EPFL

Thèse n°8303

Development of soft microscopic implants and acoustically-powered machines for biomedical applications

Présentée le 30 septembre 2021

Faculté des sciences et techniques de l'ingénieur
Laboratoire de Systèmes MicroBioRobotiques
Programme doctoral en microsystèmes et microélectronique

pour l'obtention du grade de Docteur ès Sciences

par

Murat KAYNAK

Acceptée sur proposition du jury

Prof. H. Shea, président du jury
Prof. M. S. Sakar, directeur de thèse
Prof. T. J. Huang, rapporteur
Prof. P. Fischer, rapporteur
Prof. G. Villanueva, rapporteur

École polytechnique fédérale de Lausanne

2021

The most beautiful sea:
hasn't been crossed yet.
The most beautiful child:
hasn't grown up yet.
Our most beautiful days:
we haven't seen yet.
And the most beautiful words I wanted to tell you
I haven't said yet...

— Nâzım Hikmet Ran

Acknowledgements

I would like to thank my advisor **Prof. Mahmut Selman Sakar** for feedback, advise and discussions. We started each work from scratch, which was not easy. Then, we built everything by working hard together. Additionally, he introduced me into other communities such as immunologists and neuroscientists. I have had great collaboration with them. Selman always believed that I can do proper research and publish decent articles. His support made me confident and productive throughout my PhD. He is not only an academic advisor but also a mentor for my career. He is always open to discuss any issue related to academia or my career. Thanks to him I improved my skills a lot and had a productive PhD.

I thank thesis jury members, namely **Prof. Herbert Shea, Prof. Tony Jun Huang, Prof. Peer Fischer** and **Prof. Guillermo Villanueva**, for serving in my thesis evaluation and defense. Their invaluable feedback and critics have definitely improved quality of the thesis. Their questions and suggestions for my research and career will be always in my mind.

I would like to express my gratitude to my amazing collaborators, namely **Furkan Ayhan, Pietro Dirix, Dr. Amit Dolev** and **Laura Hermans**. My thesis is based on the research we have done together. Beside our collaborative works in the articles, I have learned a lot from them. We have worked hard, did a lot of experiments and published the results together. We are a good team.

During my journey, I was lucky to collaborate with outstanding scientists. **Dr. Baptiste Guey** and **Prof. Andrea Ablasser**. Even though I had a mechanical engineering background, Baptiste was always ready to answer all my biology related questions. It was truly an honor to do research along with them. Additionally, I had an opportunity to collaborate with **Armand Kurum**, **Kewen Lei** and **Prof. Li Tang**. Armand and Kewen are not only exceptional students but also fun friends. Under Prof. Li and Prof. Sakar's guidance, we did a great job.

We have an excellent team at Center of MicroNanoTechnology (CMi) of EPFL. They are friendly and knowledgeable. Whenever I needed assistance, they came up with the best solutions to the problems. Specifically, I thank **Julien Dorsaz**, **Joffrez Pernollet**, **Cyrille Hibert** and **Patrick Madliger** for their great support during this journey.

I have valuable friends in my research group. Special thank goes to **Ece Ozelci** for her patience while listening to my experimental results and solutions to research problems. She is not only a colleague but also a close friend of mine. I would like to thank **Fazil Emre Uslu** for his great friendship both as a labmate and roommate. We have always supported each other since the very first day. I thank **Erik Mailand** for discussions and suggestions. His experiences and advice helped me a lot during my PhD. I would like to thank **Raquel Parreira** for her friendship. I thank **Matthias Rüegg** for his clear explanations on various technical topics. He is a talented educator.

I am deeply thankful to my friends in Lausanne. **Remco van Erp**, **Ozge Uysal**, **Omer Özdemir**, **Lukas Huber**, **Mustafa Kangül**, **Selen Keleş**, **Ece Yıldız**, **Paul Letainturier** for parties, picnics, drinks, dinners and camps. I thank **Eda Bayram** for our deep discussions on psychology and philosophy.

I would like to thank my lifelong mentor **Adem Özçelik** for his guidance throughout my graduate study. He has always supported me to become a successful researcher. Thanks to him, I was able to use my whole potential.

I have an amazing family. We are like a group of close friends. My parents **Ayşe Kaynak** and Şahin Kaynak are always my biggest supporters. No words can describe how I love them. My brothers; **Mustafa Kaynak**, **Şeref Kaynak** and his wife **Rukiye Kaynak** are precious to me. I love having fun, talking, sharing with them and, eventually, being a member of this family.

Last but not least, I met an amazing woman in my journey. My girlfriend, **Lebogang Moloi**, is a woman with a big heart. Her unconditional love is absolutely greatest support for me. Our brainstorming on science, gossip about anything and laughter anytime are just the biggest fun outside the campus. I feel so lucky to have such a woman in my life. I can't wait to see our future together. I am sure it will be wonderful.

Murat Kaynak
September 2021
Lausanne

Abstract

Implantable mechanical structures and electronic devices revolutionized medicine. They play a key role in the treatment of life threatening and disabling conditions such as coronary artery diseases, arrhythmia, deafness, and blindness. The capabilities of implants have been extended to open up new application areas such as targeted and chronic drug delivery, deep brain stimulation, spinal cord neuromodulation, and immunomodulation. Miniaturization of these structures and devices will certainly augment their accessibility to remote tissues and reduce their invasiveness. However, it is not trivial to manufacture sub-millimeter biomedical devices and it is even more challenging to power and operate them inside the body. Considering the potential impact of this endeavor in regenerative medicine and neuroscience, novel solutions are urgently needed.

This thesis introduces design principles and manufacturing techniques for the development of microscale soft implants and remotely actuated micromachines. Three novel microengineering solutions are introduced: (1) a suite of microfabricated structures that together provide an optical window to the ventral nervous system of fruit flies upon implantation, (2) 3D printed soft micromachines that are actuated by entrapped air bubbles, and (3) 3D printed soft micromachines that are actuated by sharp edge structures. Using the first technology, the neural activity of fruit flies can be observed and quantified throughout their lifetime. This data will be used to study the progression of neurodegenerative diseases, dissect the circuits responsible for learning motor skills, and explore the extends of neural plasticity upon amputation. The last two microengineered systems rely on traveling sound waves, a wireless actuation technique that is extensively studied throughout the thesis. We show proof-of-concept demonstrations of controlled motion, large and programmable deformation, and microfluidic operations such as pumping, sorting, and aspiration, all with untethered devices that are smaller than a millimeter. Theoretical and computational models of solid and fluid mechanics guide both the design and control procedures. The materials and methods introduced in this thesis are compatible with *in vivo* settings, opening the doors to the development of advanced microscopic injectable devices for biomedical research and clinical therapy.

Keywords: microfabrication, mechanical design, robotics, acoustics, fluid mechanics

Résumé

Les structures mécaniques implantables et les appareils électroniques ont révolutionné la médecine. Ils jouent un rôle clé dans le traitement de maladies potentiellement mortelles et invalidantes telles que les maladies coronariennes, l'arythmie, la surdité et la cécité. Les capacités des implants ont été étendues pour ouvrir de nouveaux domaines d'application tels que l'administration ciblée et chronique de médicaments, la stimulation cérébrale profonde, la neuromodulation de la moelle épinière et l'immunomodulation. La miniaturisation de ces dispositifs augmentera certainement leur accessibilité aux tissus éloignés et réduira leur caractère invasif. Cependant, il n'est pas trivial de fabriquer des dispositifs biomédicaux submillimétriques et il est encore plus difficile de les alimenter et de les faire fonctionner à l'intérieur du corps. Compte tenu de l'impact potentiel de ces initiatives en médecine régénérative et en neurosciences, de nouvelles solutions sont nécessaires de toute urgence.
Cette thèse présente les principes de conception et les techniques de fabrication pour le développement d'implants mous à petite échelle et de micromachines actionnées à distance. Trois nouvelles solutions de micro-ingénierie sont introduites : (1) une suite de structures microfabriquées qui fournissent ensemble un accès optique au système nerveux ventral des drosophiles suite à une implantation, (2) des micromachines souples imprimées en 3D qui sont actionnées par des bulles d'air emprisonnées, et (3) des micromachines souples imprimées en 3D qui sont actionnées par des structures à bords nets. Grâce à la première technologie, l'activité neuronale des drosophiles peut être observée et quantifiée tout au long de leur vie. Ces données seront utilisées pour étudier la progression des maladies neurodégénératives, étudier les circuits responsables de l'apprentissage ou de la motricité et explorer les étendues de la plasticité neuronale lors d'une amputation. Les deux derniers systèmes de micro-ingénierie reposent sur des ondes sonores, une technique d'actionnement sans fil qui est largement étudiée tout au long de la thèse. Nous montrons, comme preuve de concept, des démonstrations de mouvement contrôlé, de large déformations programmables et des opérations microfluidiques telles que le pompage, le tri et l'aspiration, le tout avec des dispositifs non attachés de moins d'un millimètre. Les modèles théoriques et informatiques de la mécanique des solides et des fluides guident à la fois les procédures de conception et de contrôle. Les matériaux et méthodes présentés dans cette thèse sont compatibles avec des paramètres in vivo, ouvrant les portes au développement de dispositifs injectables microscopiques avancés pour la recherche biomédicale et la thérapie clinique.
Mots clefs : microfabrication, conception mécanique, robotique, acoustique, mécanique des fluides

Contents

List of Figures

List of Tables

1 Introduction

1.1 Problem statement

Implantable devices are routinely used in various medical specialties, including cardiology, orthopedics, and neurology. Devices such as stents, joint replacements, pacemakers, and pumps perform an electronic or mechanical function to treat a particular injury or disease. Implants can be bioactive, such as subcutaneous drug delivery devices in the form of pills, microchips, or drug-eluting stents. Implantable devices have also become instrumental in basic research, particularly for discovering the working principles of the central and peripheral nervous system.

Untethered devices that are engineered for delivery of biological payload address a number of deficiencies of conventional means for administering pharmaceuticals. For example, it is important to maintain drug levels within the narrow concentration window required to avoid toxicity due to overdose or ineffective treatment from insufficient exposure. Furthermore, drugs must be administered with a certain chronic regimen in order to achieve a long-lasting effect, potentially resulting in patient discomfort or inconvenience, or requiring tethering to external devices. Controlled release systems provide spatial and temporal control over drug availability. More efficacious and safer therapies are introduced with the implantation procedure. The implanted device administer high drug concentrations locally at the site of disease with minimal exposure of healthy or distant tissues.

Implantable neuroprostheses are electronic devices that are designed to study and treat the injured nervous system. Cochlear implants restore hearing in deaf children, retinal prostheses restore sight to blind patients, deep brain stimulation treat Parkinson's disease, and inhibition of signaling in the spinal cord elevate chronic pain. New methods for recording and modulation of neural activity using electrical, chemical, and/or optical modalities introduce more effective combinatorial approaches for clinical solutions. Wireless neural probes with microfluidic drug delivery systems have been recently engineered as a means to perform in vivo neuromodulation inside the brains of freely behaving animals.

Miniaturization of implantable devices has several potential benefits for basic life science research and clinical applications. First and foremost, they may become injectable—they can be introduced into the body without a surgical operation. This feature would drastically reduce the risks of associated complications, therefore, facilitate the routine use of such devices. Second, miniaturization significantly expands the parts of the body that are amenable to diagnosis and treatment. For example, devices may be directly injected into deep seated tumors within internal organs. A less appreciated contribution of miniaturization is the potential impact to basic science. Majority of model animals that are used in trials such as fruit flies, mice, rats, and rabbits are quite small. Miniaturized devices enable in vivo testing of novel diagnostic and therapeutic solutions as well as exploration of physiological function.

The major bottlenecks in the miniaturization of mechanical implants is manufacturing and the process of implantation. As the size of the structures becomes smaller, proper handling and precise manipulation get more and more challenging. There are two avenues to address this issue. On one hand, fabricating structures from soft materials would reduce the risk of injury during insertion that would be otherwise caused by the application of excessive forces to the surrounding tissues. Novel manufacturing techniques are required for the fabrication of such microscopic soft implants. The second avenue is the use of robotic manipulation technology. While the existing robotic tools cannot deliver the dexterity of the human hand, they are very precise in positioning and practically tremor free. Augmenting the capabilities of human hand with robotic instruments has proven to be a successful approach in microsurgery. Novel end-effectors and manipulation strategies are required to work with tiny implants.

Miniaturization of actuated implants pose additional challenges. We cannot simply make them smaller because they contain a battery or induction antenna, and these powering units cannot be miniaturized to the microscale. Alternative solutions to power actuators in the absence of electronics have been explored during the last two decades. The sacrifice of electronic units in the pursuit of miniaturization comes with important trade-offs. First of all, neural recording and stimulation based on electrophysiology is no more an option. Secondly, on-board sensing and computation becomes extremely challenging. Thirdly, related to the previous limitation, the device must be operated blindly because there is very limited information about the state of the device and the surrounding environment. Although medical imaging may provide some information, at this size scale, small changes in the physical and chemical variables are practically inaccessible. Ideally, following the implantation, the devices are supposed to perform the intended function in an automated fashion. In this scenario, externally applied signals only provide power to the device and do not interfere with the operation.

Stimuli-responsive polymers are quite promising for actuating mechanical systems. However, they are structured for bulk deformation and, therefore, offer very limited dexterity upon miniaturization. The field of microrobotics has emerged to address some of these challenges associated with dexterous manipulation and controllable operation. A number of solutions have been proposed to realize distributed actuation of compound micromachinery using light, magnetic fields, or acoustic waves. The acquired wisdom on the engineering design principles

is essential to develop microscopic devices that can collect and/or transport fluids and solids with the desired temporal regimen. Yet, there is no solution at microscale that provides the same functionality and programmability that centimeter scale electronic devices offer.

1.2 General objectives and approach

The overall objective of this thesis is to develop a design, fabrication, implantation, and control methodology for microscale biomedical mechanical devices. The work is built upon recent advances in microengineering, particularly direct laser writing, and acoustics. Particle tracking velocimetry is routinely used throughout the project to characterize flows generated around the machines. To address the aforementioned challenges and provide a complete robotic solution, the work has been focused on the following sub-domains:

- (Fabrication) Fabrication of soft and flexible microstructures with arbitrary form
- (Power) A remote powering scheme that works inside living systems and does not rely on the localization of the device
- (Design and Control) A detailed experimental and computational study of solid and fluid mechanics along with acoustic vibrations to determine proper design and control parameters

The actuation paradigm is based on harnessing the energy carried by travelling acoustic waves. Here is a description on how I envision a purely mechanical system to recapitulate the autonomous operation of a classical robotic device. The device is engineered in a way that actuators are distributed throughout the chassis. The underlying philosophy is that large groups of connected small things can achieve almost anything—if connected in the right way, as exemplified by the brain and locomotion systems of animals.

The acoustic wave excites the actuators in a prescribed and selective way so that their timely functioning results in complex operations such as translation and rotation, mixing of fluids, mass transport, filtering and sorting of particles etc. Rationally designed flexible mechanisms push the functionality to the next level so that logic operations are permitted. The device does not always respond the same way to the same acoustic wave, it can be reprogrammed to respond differently depending on the intended performance.

Previous work has shown that acoustic waves can generate local forces in two distinct ways: either vibrating sharp edge structures or gas bubbles that are patterned or entrapped on the walls of the device, respectively. In both options, the structures resonate with the traveling acoustic wave, generating primary and secondary effects including acoustic streaming and radiation forces. In this thesis, I explore various ways to use these forces in device actuation.

Considering the multiphysics nature of the problem that includes nonlinear interactions between the acoustic wave and the actuator unit (solid or gas bubble), the device and the

surrounding fluid, the pressure generated by an actuator unit and other actuator units located nearby, theoretical and computational models are instrumental to be able to design and synthesize controllers. A number of physical models with different levels of abstraction/complexity are introduced throughout the thesis.

1.3 Thesis outline and major contributions

The following chapters are organized to highlight the major accomplishments in different aspects of microengineering (i.e., design, fabrication, control). The thesis starts with a summary of the basics that is required to understand the technical content and help the reader appreciate the impact of the original results to the advancement of the field. In this background chapter, **Chapter 2**, I summarize the state-of-the-art in the fabrication of remotely actuated microscale devices and the theory behind acoustic actuation.

Chapter 3 shows how implantation of a microfabricated flexible structure into living animals (fruit fly) open up the possibility of monitoring long-term anatomical and functional changes in premotor and motor circuits over a lifetime. Although the structure had relatively simple design and only provided structural support (i.e., no external powering), this work has multiple important contributions.

- We showed that the implant had minimal impact on animal behavior and survival. This result is quite encouraging for the future of this research as the actuated devices could also be fabricated from the same polymer.
- The instruments that were used for implantation are versatile. Any microscopic polymer device could be implanted into small animals using the same or similar tools.
- We designed and 3D nanoprinted a remounting stage that allows flies to be gently yet firmly restrained during repeated imaging of the nervous system. This prototype is first of its kind, and it opens a whole new direction for microengineered devices in the context of handling living animals.

In **Chapter 4**, we explore the following question: Can we excite solid structures to deform in 3D space using a single acoustic source? To this end, we based our actuation paradigm on air bubbles encapsulated inside cavities. Microbubbles are very efficient in transducing mechanical work from pressure waves in physiological fluids due to the large mechanical impedance mismatch between water and air. We pushed the capabilities of direct laser writing and printed ultraflexible beams to hold bubbles, precisely control the spatial and temporal dynamics of their vibrations, and the resultant operation of the compliant mechanisms. This work pushes the ultrasound actuation concept from simple machines with few degrees of freedom to match the capabilities of magnetorheological materials and liquid crystal elastomers. Here is a summary of the major contributions to the broader community:

- We provide the know-how to print ultraflexible structures and bistable mechanisms from soft materials
- A detailed characterization of bubble-fluid and bubble-bubble interactions revealed a framework to design future machines
- For the first time, we show that machines can be programmed to operate in a certain way while being powered by ultrasound
- The materials and methods are compatible with in vivo settings, opening the doors to the development of advanced microscopic injectable devices for biomedical research and clinical therapy.

In the remaining of the thesis, I propose solutions that eliminate the use of air bubbles for transducing acoustic energy. While bubbles are quite efficient, microrobotic systems actuated by entrapped bubbles work reliable only for hours. The size and mechanical response of bubbles do not stay the same under physiological conditions, thereby gradually shifting the natural frequency of the actuators and deteriorating the performance of the machine. **Chapter 5** introduces an integrated design and fabrication methodology for the spatiotemporally resolved, frequency addressable acoustic actuation of 3D hydrogel microrobots. Once excited periodically at its resonance frequency, a microstructure with sharp features submerged in fluid generates a pair of counter-rotating vortices and a localized jet as a manifestation of viscous streaming. This principle constitutes the foundation of the actuation strategy used in this part of the thesis. With a machine printed monolithically from a single polymer, I demonstrated that:

- Wireless microfluidic devices that contain several pumps can be fabricated and operated using ultrasound. Pumps are selectively activated at different frequencies.
- Mobile micromachines can be translated and rotated using thrusters that work by momentum transfer. The motion can be controlled by selectively activating several thrusters at different frequencies.
- Pumping and motion can be combined on the same machine by printing thrusters and pumps together.

In **Chapter 6**, a fabrication technique that allows polymerization of very soft materials is explored. The technique is based on projection lithography, and it allows batch polymerization of 2.5D structures inside microfluidic devices. The use of soft materials is important in four different aspects:

- The forces generated by the vibrating structure depends on the amplitude of vibrations. By using soft materials, we could fabricate very flexible sharp edge structures that provide higher performance.

- Stimuli-responsive hydrogels are very soft with a Young's modulus on the order of few kPa. By incorporating such materials into the machine body, we can instantiate shape-adaptation and on-board sensing.
- It is very appealing to create implantable machines from biomaterials such as collagen or fibrin. Those materials can be shaped using replica molding techniques. Now that we determined the design principles for soft machines, we can start building machines from natural polymers.
- In certain biomedical applications, biodegradable implants are desirable. Polymers that degrade under physiological conditions are also very soft.

Implications of these and inventions, and the work that must be done to translate these technologies are discussed in **Chapter 7**.

2 Background

This chapter provides a brief overview of techniques to fabricate and actuate machines at microscale. For the fabrication part, we focus on two photon polymerization and projection lithography. After briefly summarizing different actuation techniques, the summary is focused on machines with distributed actuation, either through the use of composites or by assembling compound machines from several actuators and mechanisms. The theory behind acoustic actuation is described in more detail as it is the principal force driving the microrobotic systems introduced in the remaining chapters of the thesis.(Figure 2.1)

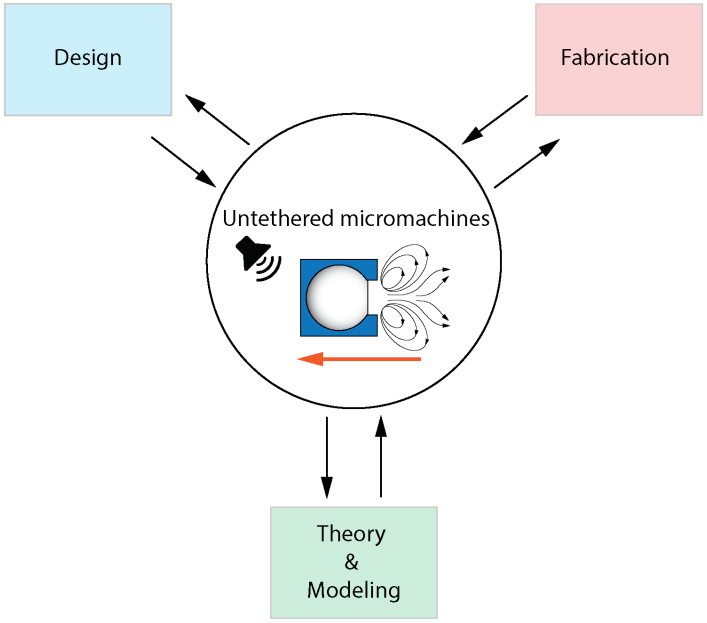

Figure 2.1 – Microscopic machine development

2.1 Untethered microscopic machines

2.1.1 Fluid mechanics at small scales

The relative importance of physical parameters in actuation may change with size. Reynolds number (Re), a dimensionless number that captures the characteristics of the fluid flow, is commonly used to evaluate the relative contribution of inertial forces with respect to viscous forces. It is defined as

$$Re = \frac{uL\rho}{\eta} \approx \frac{F_{\text{inertia}}}{F_{\text{viscous}}} \tag{2.1}$$

where u is the characteristic speed of the object, L is the characteristic length of the object, ρ is the density of the fluid, and η is the dynamic viscosity of the fluid. Here, F_{viscous} denotes the viscous forces and F_{inertia} denotes the inertial forces. The mass and volume scales as $m, V \sim L^3$ while the surface area of a machines scales as $A \sim L^2$. When Re decreases, relative contribution of inertial forces reduces while surface forces gradually become dominant. When Re$\ll$1, the Navier-Stokes equation can be simplified as:

$$\nabla P = \eta \nabla^2 U + f \tag{2.2}$$

where P is pressure, U is the fluid's velocity field, and f is the external forces. In the absence of inertial and time-dependent terms, which is commonly referred as Stokes regime, the flow around an object shows time reversible motion.

As a manifestation of Stokes regime and lack of inertial effects, bacteria must actuate their appendages to be able to keep moving. In a few milliseconds after the actuation stops, the motion ceases. The same physics is applicable to engineered micromachines. They must be actuated at all times to be able to maintain motion. Another interesting result of Stokes regime is that reciprocal motion cannot generate net movement in Newtonian fluids [1]. Therefore, the design and/or actuation of the micromachines must break the spatial and/or temporal symmetry to realize net movement or mass transport.

Analogous to macroscale, the forces generated by the actuators must be at the right magnitude and direction to realize deformation and motion inside physiological environments. The forces generated by living organisms are on the order of pico- to nano Newtons [2], [3]. These values give a course metric for the creation of synthetic actuators. For the design, there are two common techniques to break the time-reversal symmetry: using helical structures resembling the flagellum of the bacteria [4], [5] and waving structures resembling the flagellum of sperm cells [6]. Chemical and acoustic motors harness other forces such as streaming, surface tension, and electric phenomena.[7]

2.1.2 Fabrication of micromachines

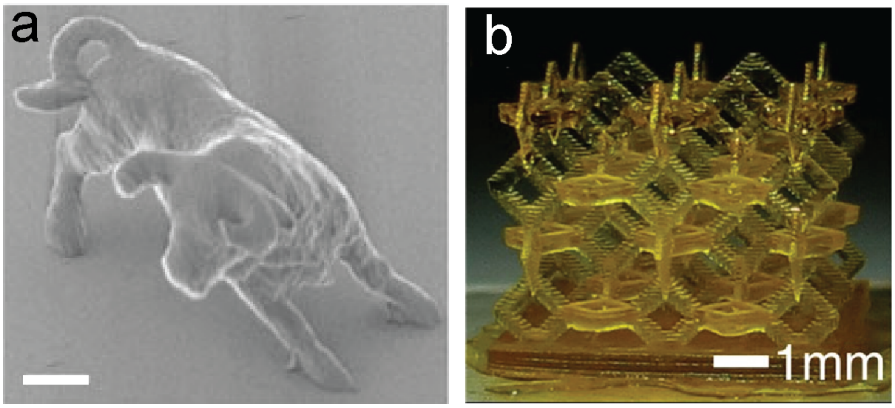

Figure 2.2 – Examples of 2PP and projection lithography. a) A bull sculpture is printed by applying 780 nm wavelength light using 2PP. Scale bar: 2 μm. Reproduced from [8] b) A 3D design fabricated using projection lithography. Patterns at each layer structured with a digital micrometer device while z axis is controlled with printer's stage. Reproduced from [9]

.

Additive manufacturing methods are the first choice for the fabrication of rationally designed complex microscopic machines [10]. More specifically, photopolymerization techniques provide nanoscale precision and a large material selection. Among others, two photon polymerization (2PP) (Figure 2.2a) and projection lithography (Figure 2.2b) are quite versatile [8], [9]. These methods are based on free radical polymerization to cure pre-polymer solution at defined regions of the workspace (Figure 2.3). Our manufacturing pipeline is primarily based on these two techniques.

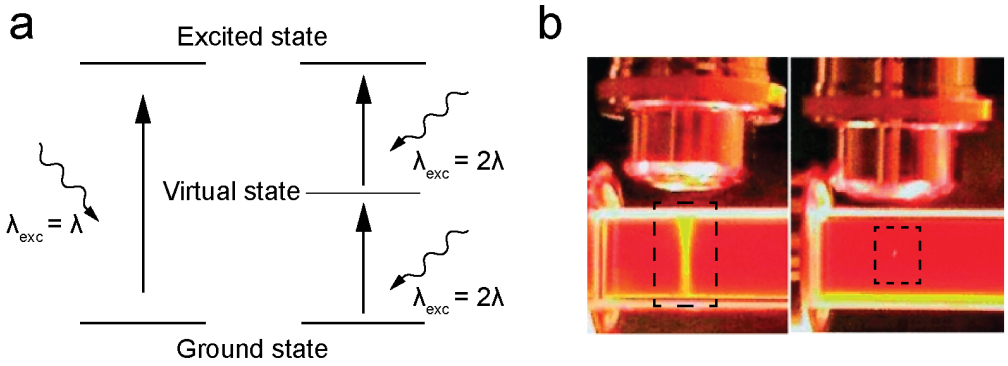

Figure 2.3 – Two photon and single photon excitation a) Jablonski energy diagram for the one-photon and two-photon excitation. b) (Left) Single photon excitation can go through the sample while (right) Two photon excitation focuses the light in a voxel. Reproduced from [11].

In 2PP, laser beam is focused on a layer creating a voxel volume, the main parameter that defines the resolution of printing. The laser scans the entire layer with the aid of a galvo-mirror while the piezo stage moves to the successive layers according to the CAD drawing. Projection lithography uses one-photon polymerization through a digital micromirror device, which

patterns light digitally into any 2D shape. By adjusting the height after polymerization of each layer, 3D structures can be manufactured layer by layer.

2.1.3 Magnetic and optical actuation methods

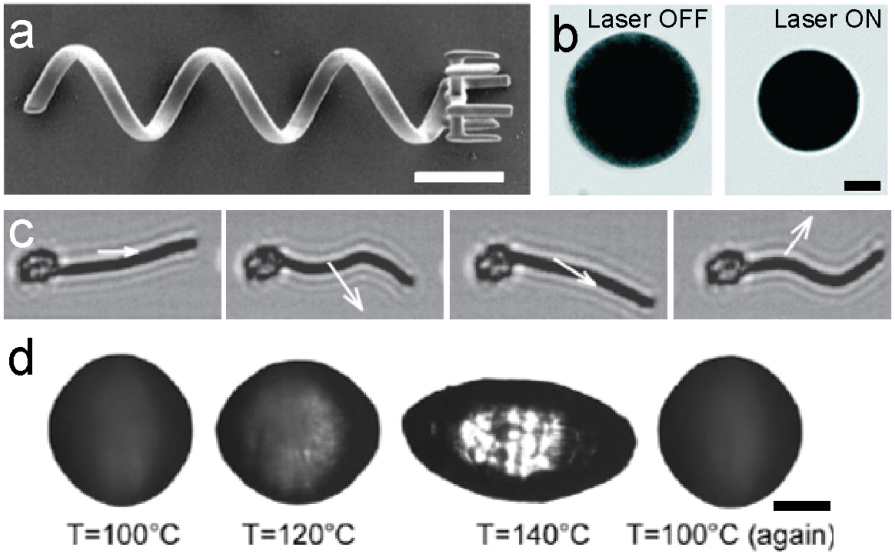

Figure 2.4 – Examples of microscopic scale actuation methods: a) A 3D printed, magnetically actuated helical microswimmer. Scale bar: 10 µm. Reproduced from [12] b) A microactuator contracted as a result of plasmonic photothermal effect of gold nanoparticles upon near infrared illumination. Scale bar: 10 µm. Reproduced from [13] c) A microscopic artificial swimmer has a tail and a red blood cell head connected each other with DNA. The tail comprised of many magnetic beads linked with DNA, too. The tail length is 24 µm. Reproduced from [6]. d) An actuator made out of liquid crystalline elastomer reversibly deforms in response to light, thus heating, which eventually triggers a phase transition. Scale bar: 100 µm. Reproduced from [14].

Respecting the flow conditions and considering manufacturing constraints, a variety of untethered micromachines have been developed [7]. In the context of this thesis, magnetic and optical actuation methods are the most relevant as they are analogous to acoustic actuation methods (Figure 2.4). Detailed theoretical and experimental work has shown that torque and not force is favorable in magnetic actuation [15]. Based on this rule of thumb, a number of different locomotion modes have been demonstrated that involves rotation, oscillation, and bending [16]–[18]. In order to make the micromachines swim in fluids, they were designed in the form of a corkscrew, resembling the prokaryotic flagellum (Figure 2.4a) [4], [12] . Alternatively, flexible propellers that beat in a planar waveform are engineered, resembling spermatozoa or cilia as shown in Figure 2.4c [6].

Optical illumination provides an alternative for powering microactuators [19], [20]. Notably, the combination of plasmonic photothermal effect of gold nanoparticles with chemomechanical potential of stimuli responsive hydrogels enables rapid and efficient conversion of energy

[21] (Figure 2.4b). This transduction mechanism has been used to actuate a variety of soft micromachines, ranging from grippers to swimmers [13], [22]. Liquid crystalline elastomers (LCEs) can also reversibly deform in response to light, realizing wireless microactuators [23]–[25]. Light can either cause a direct phase transition or induce heating, which eventually triggers a phase transition (Figure 2.4d).

2.1.4 Complex micromachines

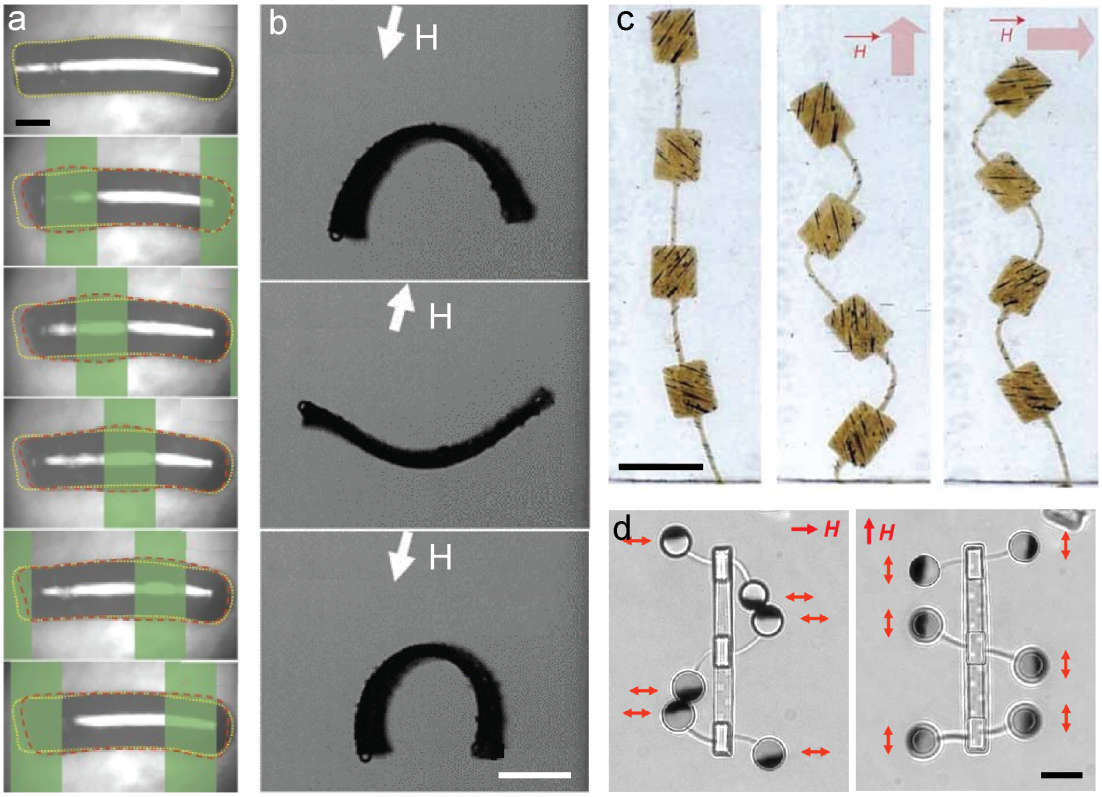

Figure 2.5 – Small scale machines which deform their bodies under external field. a) A LCE swimmer moves by deforming its body as a result of spatial distribution of light exposure. Scale bar: 200 µm. Reproduced from [26]. b) A small scale body-deforming soft robot consisting of elastomer and magnetic particles which are aligned for multi DOF deformation. Scale bar: 1 mm. Reproduced from [27]. c) Magnetic domains connected to each other with soft beams. Depending on the magnetic domain alignment, complex deformation patterns can be achieved. Scale bar: 100 µm. reproduced from [28]. d) Magnetic micromachines linked with soft beams. Already aligned magnetic beads deformed the soft beams under magnetic field. Multiple beam deformation can be achieved by simply altering the direction of magnetic field. Scale bar: 10 µm. Reproduced from [29].

As introduced in the previous chapter, one of the main challenges in the field is to engineer machines with several actuators working together for the execution of a complex and programmable task. There are two alternative strategies being pursued so far. First one relies on

the complexity of the excitation signal and the second one on the complexity of the machine design.

First strategy is based on the distribution of many small magnets or liquid crystals within a highly deformable polymer structure. By dynamically modulating the direction of the magnetic field or the spatial distribution of light exposure, deformation with many DOF can be generated. The idea here is not to worry about where the individual actuators are, which are simple particles, but to concentrate on the bulk deformation of the composite structure. This strategy has been extensively used with magnetorheological materials. Using the capabilities of LCEs, micromachines were made to crawl on surfaces [24] or swim in fluids [26] (Figure 2.5a). Different parts of the machine were activated at different times using the spatial resolution of light exposure. In another approach, magnetic particles were distributed inside an elastomer host and put into the desired form using 3D printing [30] or replica molding [27], [31]. Impressive locomotion gaits were generated using these micromachines [27], [30], [32] (Figure 2.5b). The idea is quite similar to LCE but this time instead of applying spatial light exposure, a magnetic field that affects all the embedded particles was applied.

Second strategy relies on mechanical design. The positioning of the actuators is critical, and the whole machine must be assembled according to a master plan. The musculoskeletal system of the vertebrates and almost all macroscopic robots are designed based on this paradigm. Analogous to the aforementioned magnetic elastomers, magnetic domains were connected to each other using very flexible beams or ribbons [28], [29], [33]. By prescribing the distribution of magnetic particles, very complex deformation can be programmed for a simple magnetic field (Figure 2.5c). This strategy also provides higher resolution compared to the first approach, however, with the burden of design and manufacturing complexity. Another interesting prototype is a mobile micromachine with an on-board pumping and sorting mechanism [34]. The pumping mechanism was based on the Archimedes screw and the machine was engineered to load and release cargo in a dose-dependent manner. Functional parts were printed together to form a single device without the need for further assembly using direct laser writing and selective magnetic film deposition. Dexterous micromachines can also be built from optomechanical actuators [13]. A variety of soft robotic microdevices were constructed by physically attaching microactuators to hydrogel mechanisms that are directly photopolymerized around the actuators without additional assembly procedures (Figure 2.5d). This thesis falls into the second category.

2.2 Acoustic micromachines

2.2.1 Examples of acoustic micromachines

Acoustic waves are mechanical waves that travel through a medium as a form of pressure pulses and elastic deformation. They have been used in clinics for various purposes including imaging, breaking up stony deposits, and cancer therapy[35]. Furthermore, acoustic waves are

utilized for particle and cell manipulation [36], [37]. An emerging application of microbubbles is drug delivery to the brain [38], [39].

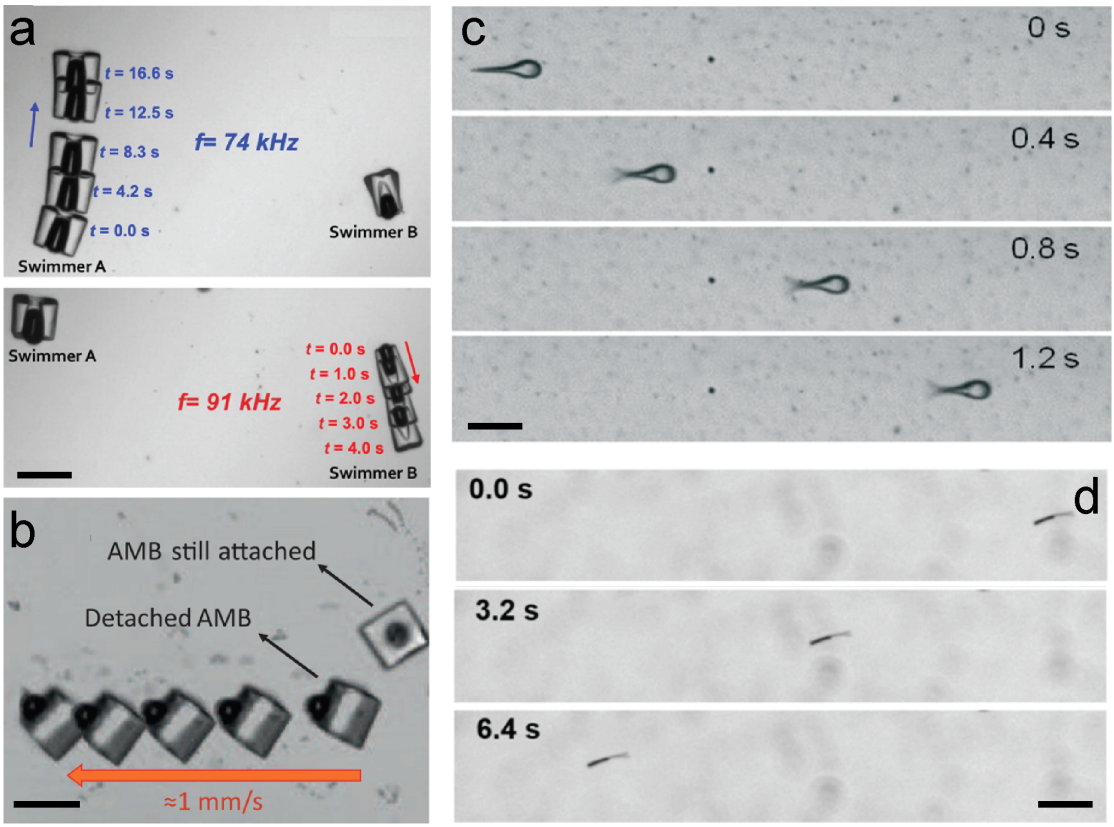

Figure 2.6 – Examples of acoustic micromachines a) Selective manipulation of a bubble based swimmer at different frequencies. Scale bar: 150 µm. Reproduced from [40]. b) A 3D printed bubble-based free swimmer moving through media. Scale bar: 50 µm. Reproduced from [41]. c) A sharp edge based microswimmer swims directionally upon acoustic excitation. Scale bar: 150 µm. Reproduced from [42]. d) A nanoswimmer oscillates its tail and moves directionally under acoustic field. Scale bar: 15 µm. Reproduced from [43].

Acoustic waves are appealing to power micro/nano machines because they generates relatively high forces, and penetrates through biological samples with minimal side effects [44]. Air bubbles and solid sharp edges that are actuated with acoustic waves generate thrust and propel micromachines Figure 2.6. Under acoustic excitation, entrapped air bubbles pulsate at the interface, which generates steady streaming (acoustic streaming) on the sides and a jet flow in the middle of the open surface. Bubble deflection reaches its maximum at the natural frequency of the bubble, which results in maximum acoustic streaming velocity. This streaming generates thrust, which we refer to as acoustic streaming force (Figure 2.6a, b). When sharp edges are actuated with an acoustic field, acoustic streaming force is generated through structural oscillations, which reaches its maximum at the tip of sharp edge (Figure 2.6c,d). Bubbles and sharp edges are also affected by the incident acoustic waves when the wavelength of the acoustic wave is comparable to the radii of the entrapped bubbles.

In this thesis, our micromachines are much smaller than the applied wavelength. Therefore, we ignore the primary radiation forces. We assume that thrust is only produced by acoustic streaming [45]. The resonance frequency of air bubbles can be altered by adjusting their volume, which results in selective manipulation of acoustic machines (Figure 2.6a). [40] Bubbles actuated by acoustic waves expand and contract due to their compressibility. As a result, air bubbles act as secondary acoustic sources and generate acoustic pressure field that affects air bubbles that are nearby [46], [47].

2.2.2 Energy analysis of acoustic actuation

We can explain the relationship between acoustic energy density, acoustic pressure, applied voltage and resultant force in a bulk acoustic wave system by considering the medium as linear, compressible viscous and Newtonian fluid.[48].

The energy density (E_{ac}) in a unit volume is considered as the sum of the kinetic (E_{k}) and potential energy (E_{p}):

$$E_{\mathrm{ac}} = E_{\mathrm{k}} + E_{\mathrm{p}} \tag{2.3}$$

where E_{ac}, E_{k}, E_{p} are the acoustic energy, kinetic energy and potential energy, respectively. By definition, the kinetic energy scales with velocity of the volume as $E_{\mathrm{k}} \propto u^2$. The unit volume velocity can be considered as zero in a closed system for simplification. Therefore, the kinetic energy can be neglected. Hence, acoustic energy is transferred via potential energy. The media is a compressible fluid which changes the unit volume when acoustic waves travels through V to $V^{'}$. To simplify, we consider the volume change in $-x$ direction only. Therefore,

$$S = \frac{\partial u}{\partial x}, \qquad p = -\rho_0 {V_0}^2 S \tag{2.4}$$

where S, u, p, ρ_0 and V_0 are dilatation, displacement, acoustic pressure, medium density and wave velocity, respectively. Thus, the volume is:

$$V^{'} = V\left(1 + \frac{\partial u}{\partial x}\right) = V\left(1 - \frac{p}{\rho_0 {V_0}^2}\right) \tag{2.5}$$

Therefore, the change in the acoustic energy is computed as

$$U_{\mathrm{P}} = -\int p dV, \qquad dV = -\frac{V dp}{\rho_0 {V_0}^2} \tag{2.6}$$

As a result, we can write

$$U_{\mathrm{P}} = \frac{V}{\rho_0 {V_0}^2} \int_0^p p\,dp = \frac{1}{2} \frac{p^2 V}{\rho_0 {V_0}^2} \tag{2.7}$$

We do not have additional energy input. Thus,

$$E_{\mathrm{ac}} \propto U_{\mathrm{P}} \propto p^2 \tag{2.8}$$

Assuming that piezoelectric transducer transmit the acoustic energy well due to coupling between its substrate, a linear relationship between applied peak-to-peak voltage and pressure can be considered as [49]

$$V_{\mathrm{PP}} \propto p \tag{2.9}$$

Thus, acoustic energy density quadratically scales with applied peak-to-peak voltage as

$$E_{\mathrm{ac}} \propto {V_{\mathrm{PP}}}^2 \tag{2.10}$$

Then, force (thrust) can be described as

$$F \propto {V_{\mathrm{PP}}}^2 \propto p^2 \tag{2.11}$$

The drag force (F_{d}) is generated through the motion of micromachines in liquid. At low Re regime, the drag force around a sphere is given by

$$F = F_{\mathrm{d}} = 6\pi a \eta V_0 \tag{2.12}$$

where a is radius of sphere, η is dynamic viscosity of fluid and V_0 is velocity of the sphere.

The overall dynamics is captured by

$$F = F_{\mathrm{d}} \propto {V_{\mathrm{PP}}}^2 \propto p^2 \propto V_0 \tag{2.13}$$

The velocity of a microsphere can be controlled through voltage applied to the acoustic transducer. This approximation has been experimentally validated using microswimmers in different setups.[41], [43]

The total force is given by

$$F = F_S + F_R \tag{2.14}$$

where F_S is acoustic streaming force and F_R is the radiation force (also called primary acoustic radiation force). In this thesis, wavelengths are much longer than the micromachine sizes; this, we ignore F_R. F_S can be defined through the momentum flux and can be defined as time average of the stress exerted on the interface of bubble (or sharp edge) and medium.

$$F_S = \iint_S \sigma \ . \ \mathbf{n_P} \ dS \tag{2.15}$$

where σ is the stress tensor on the bubble (or sharp edge) surface and $\mathbf{n_P}$ is the normal vector to the surface of bubble (sharp edge).

3 Microimplants for long-term imaging of ventral nervous system in *Drosophila*

Biological processes occur at multiple timescales ranging up to an animal's lifetime. For example, the connectivity and dynamical activity of neural circuits can continuously shift in response to new experiences and fluctuating internal states. Therefore, to gain a complete understanding of how neural activity orchestrates cognition and behavior, one needs minimally invasive methods for repeatedly measuring and perturbing circuits in behaving animals across time. Although such tools have been developed to investigate brain function, there is a lack of equivalent approaches to comprehensively and repeatedly record from motor circuits in intact, behaving animals. Here we describe a suite of microfabricated technologies that enable long-term, minimally invasive optical recordings of the adult *Drosophila melanogaster* ventral nervous system (VNS)—neural tissues that are functionally equivalent to the vertebrate spinal cord. These tools consist of (i) a dissection arm that permits the insertion of (ii) a compliant implant in the thorax to expose the imaging region of interest; (iii) a numbered, transparent polymer window that encloses and provides optical access to the thoracic interior, and (iv) a versatile tethering stage that allows one to gently and repeatedly mount an implanted animal for optical recordings. We show that the thoracic implant and window have minimal impact on animal behavior and survival, enabling neural recordings from individual animals across at least one month. Thus, our microfabricated technologies open up the possibility of monitoring long-term anatomical and functional changes in premotor and motor circuits across an animal's lifetime.

This chapter is an adapted version of the following work:

Hermans, L. [*], **Kaynak, M.** [*], Braun, J., Ríos, V. L., Günel, S., Aymanns, F., and Sakar, M. S., Ramdya, P., "*Long-term imaging of the ventral nervous system in behaving adult Drosophila*" (in preparation).

[*]Equal contribution

Author contribution

Kaynak, M. designed, fabricated and tested compliant implants, transparent windows and tethering stages according to *in vivo* data provided by other authors, contributed the methodology and wrote the paper with other authors.

3.1 Introduction

Biological tissues possess a remarkable ability to adapt to changing internal physiological conditions and external environments. This plasticity drives processes across a wide range of spatial scales—from cells to tissues—and temporal scales—from milliseconds up to an animal's lifetime. In neuroscience, many physiological studies of long timescale phenomena (e.g., memory formation and neurodegeneration) have compared data pooled across animals measured at different time points. This is not ideal due to the inter-individual variability. However, important technical challenges accompany investigating the same animal repeatedly. For example, experiments must be repeatedly tolerated by the animal, and the same neurons must be identified across measurements.

With the advent of microscopy-based neural recordings, like 2-photon calcium imaging [50], it has become possible to repeatedly measure neurons' activity in a minimally invasive manner. Furthermore, chronic recording approaches allow one to study an individual animal's brain circuits *in vivo* and across time. Chronic long-term imaging became prominent in early studies of mouse neocortex using cranial windows [51]. Since then, these technologies have advanced to improve the spatial extent [52], depth [53], and duration [54] of brain recordings. Similarly, long-term neural recordings have been an important goal in neuroscientific studies of the adult fly *Drosophila melanogaster*. *Drosophila* offers the advantages of being genetically tractable, having a numerically small nervous system, and generating complex social, navigation, and motor behaviors [55]–[58]. Thus, by building upon pioneering methods for recording brain circuits during behavior [59], [60], recent approaches permit chronic recording of the fly's brain circuits [61], [62].

However, these techniques have been restricted to the study of superficial brain regions. Only very recently, has it become possible to image downstream premotor and motor circuits in tethered, behaving mice [63], and flies [64]. The adult fly's motor circuits are principally found in the ventral nervous system (VNS). The VNS is organized similarly to the mammalian spinal cord [65], and it's control principles are also likely conserved to those of mammals—including the roles of central pattern generators (CPGs) and proprioceptive sensory feedback [66], [67]. Thus, the possibility of investigating the relatively small and genetically accessible *Drosophila* VNS is especially enticing.

The VNS rests ventrally within the fly thorax beneath layers of opaque tissue including—from ventral to dorsal—salivary glands, gut, indirect flight muscles, and cuticle. Thus, until recently, it has not been possible to record from this neural tissue in tethered, behaving animals. Our laboratory developed a technique to gain optical access for imaging the VNS during behavior by surgically (and genetically, in the case of indirect flight muscles) removing these tissues [68]. However, this operation is invasive, requiring the resection of organs and leaving an open thoracic cavity, both of which preclude long-term recordings beyond several hours. Thus, although this technique allows one to acutely study *Drosophila* premotor and motor circuits, understanding how these circuits reorganize to adapt over time has remained out of reach.

Here, we describe a suite of microfabricated tools that permit recordings of the *Drosophila* VNS for more than one month. These tools were inspired by those used to study larger animals—transparent windows [52], [54] and implants [53]—and radically modified to address the unique challenges of studying the tiny fly (≈ 2-3 mm long). These minute tools are orders of magnitude smaller and allow for extremely gentle tissue manipulation. They include (i) a manipulator tool ('arm') that allows us to move aside and hold in place thoracic organs, (ii) flexible, implantable structures that alleviate the need for surgically removing thoracic organs to access the VNS, (iii) a transparent polymer window that encloses the thoracic cavity and is numbered to allow individual flies to be distinguished from one another across consecutive imaging sessions, and (iv) a remounting stage that allows flies to be gently yet firmly restrained, allowing repeated imaging of the same animal. We provide detailed descriptions of how to fabricate and operate all of these tools, accelerating their adoption by other laboratories.

To show how our long-term imaging toolkit enables the exploration of neural circuit adaptation, we present proof-of-concept studies. First, we show that implants and windows have minimal impact on animal survival and behavior, and, then, that they permit neural recordings for at least one month.

3.2 Development of the methods

3.2.1 Fabrication of polymer molds that are used to cast implants

We developed a two-level microfabrication technique to maximize throughput, protect master molds from excessive use, and facilitate technology dissemination. Briefly, implants were cast within elastomer templates, that were fabricated from an etched wafer serving as a master mold. First, a four-inch silicon test wafer (100/P/SS/01-100, Siegert Wafer, Germany) was treated with hexamethyldisilazane (HMDS) (CAS number: 999-97-3, Sigma-Aldrich, Germany) and dehydrated at 125°C to enhance adhesion to its surface. The wafer was then spin-coated with an 8 µm thick film of positive photoresist (AZ 9260, Microchemicals GmbH, Germany) using an automatic resist processing system (EVG 150, EV Group, Germany) (Figure 3.1a-i). After baking, exposure, and development steps, the wafer was then processed using deep reactive ion etching (DRIE), specifically a Bosch process, to obtain nearly vertical walls with a high aspect ratio (Figure 3.1a-ii). The remaining positive resist was stripped in a remover (Remover 1165, Kayaku Advanced Materials, USA) at 70°C and cleaned by rinsing with water and air drying (Figure 3.1a-iii). The elastomer templates were fabricated by replica molding using polydimethylsiloxane (PDMS). The replica molding process began with vapor deposition of a silane (trichloro(1H,1H,2H,2H-perfluorooctyl) silane, Sigma-Aldrich, Germany) onto the surface of the master mold in a vacuum chamber for 6 h. This silanizion was performed only once because it forms a permanent silane layer. PDMS was prepared as a mixture (10:1, wt/wt) of the elastomer and the curing agent (GMID number: 01673921, Dow Europe GmbH, Germany) and poured onto the wafer in a petri dish. To release any bubbles trapped inside the high aspect ratio wells, the mold was degassed using a vacuum pump (EV-A01-7, Swiss Vacuum

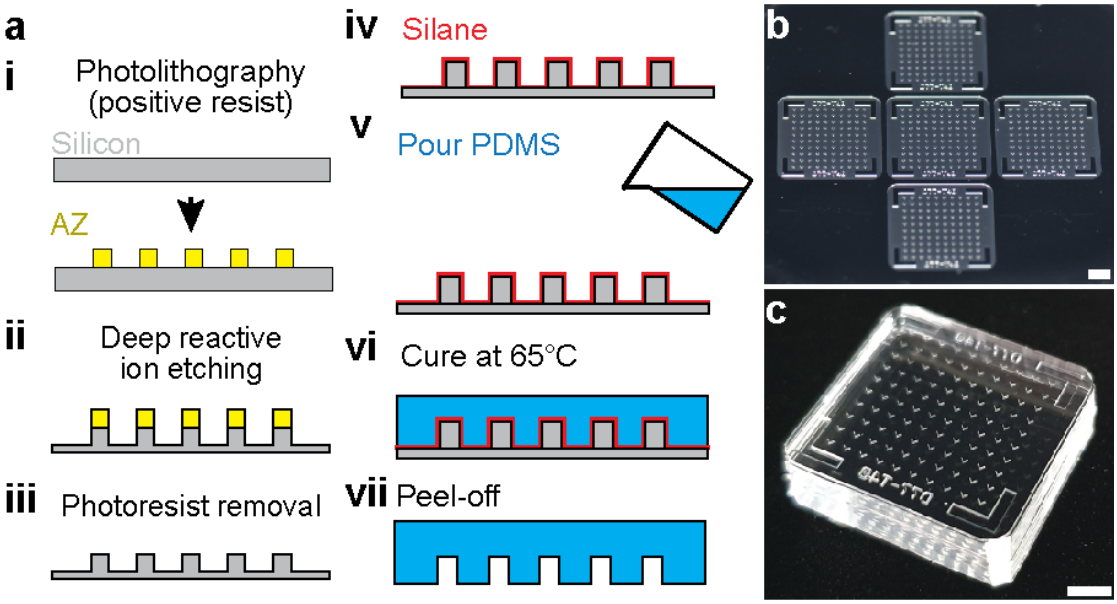

Figure 3.1 – Fabrication of molds used to cast implants.a) Implant molds are fabricated in the following steps. i) Through photolithography, a positive resist, AZ, is crosslinked onto a silicon wafer to form a temporary mask. ii) Deep reactive ion etching is used to sculpt the silicon wafer. iii) The photoresist is removed. iv) Subsequently, this silicon piece is silanized. v) PDMS is then poured, vi) cured, and vii) peeled off. b) This process yields a single large piece. Scale bar: 0.5 cm. c) This large piece is cut into multiple individual implant molds. Scale bar: 0.5 cm.

Technologies SA, Switzerland) in a vacuum desiccator (F42020-0000, SP Bel-Art Labware & Apparatus, USA). Finally, the elastomer was cured at 65°C for 5 h and the PDMS slab was peeled off (Figure 3.1b). Using alignment markers as a guide, the slab was then cut into several pieces with a razor blade to serve as templates with which one could then fabricating implants (Figure 3.1c). The silicon master mold can be used multiple times for PDMS mold fabrication.

3.2.2 Fabrication of implants

Flexible implants were fabricated from a photocurable polymer (Ostemer 324 Flex, Mercene Labs AB, Sweden). Polymerization occurs when a mixture of the base (Part B) and hardener (Part A) are exposed to UV light (Figure 3.2a-i). The PDMS template was silanized (trichloro(1H,1H,2H,2H-perfluorooctyl) silane, Sigma-Aldrich, Germany) for 1 h 45 minutes in a vacuum desiccator (Figure 3.2a-ii). Part A was warmed at 48°C overnight to make sure there were no undissolved crystals remaining in the solution. Part B and the container were also heated up to 48°C before mixing. Parts A and B were then mixed thoroughly and the mixture was degassed in a vacuum chamber for 5 min. A 200 µL drop of the mixture (1:1.86, wt\wt) was poured on the template (Figure 3.2a-iv) and the template was mechanically sandwiched between two glass slides using two clips. The glass slide which touched onto the implant

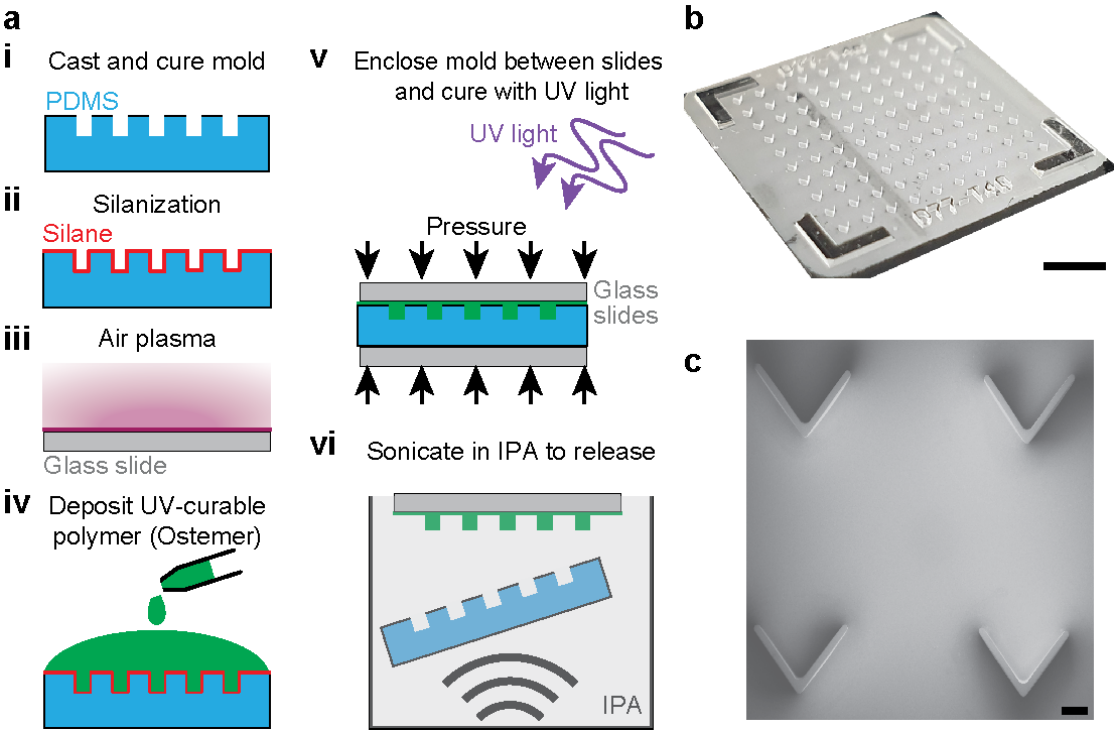

Figure 3.2 – Fabrication of implants. a) Implants are fabricated in the following steps. i) PDMS molds are cast, cured, and cut into pieces. ii) PDMS molds are silanized. iii) A glass slide is plasma treated to promote adhesion. iv) A UV curable polymer is deposited onto the PDMS mold. v) Subsequently, this composite is sandwiched between glass slides and exposed to UV light. vi) The mold is sonicated to release in IPA. b) This high throughput process yields 100 implants in a single mold. Scale bar: 0.5 cm. c) A scanning electron microscopy image confirms the precision of implant fabrication. Scale bar: 200 µm.

polymer was plasma treated (PDC-32G, Harrick Plasma,USA) at 29 W for 1 min to ease the releasing of implants by improving the adhesion between glass and implants. The solution was exposed to UV light (365 nm, UV9W-21, Lightning Enterprises, USA) for 10 min for polymerization (Figure 3.2a-v). The samples were rotated several times during UV exposure to ensure a homogeneous reaction throughout the template. The implants were released by mechanically agitating the templates in isopropyl alcohol (IPA) using a sonicator (DT 100 H, Bandelin Sonorex Digitec, Germany) (Figure 3.2a-vi). This whole process yielded a wafer with 100 implants (Figure 3.2b,c) that were subsequently cut with a needle for experimental application.

3.2.3 Fabrication of thoracic windows with engraved markers

Thoracic windows (transparent polymer disks) were fabricated using photolithography. All exposure steps were performed on a mask aligner (MJB4 , Süss Microtec, Germany) using i-line illumination. Chrome masks were fabricated using a direct laser writer(VPG-200, Heidelberg

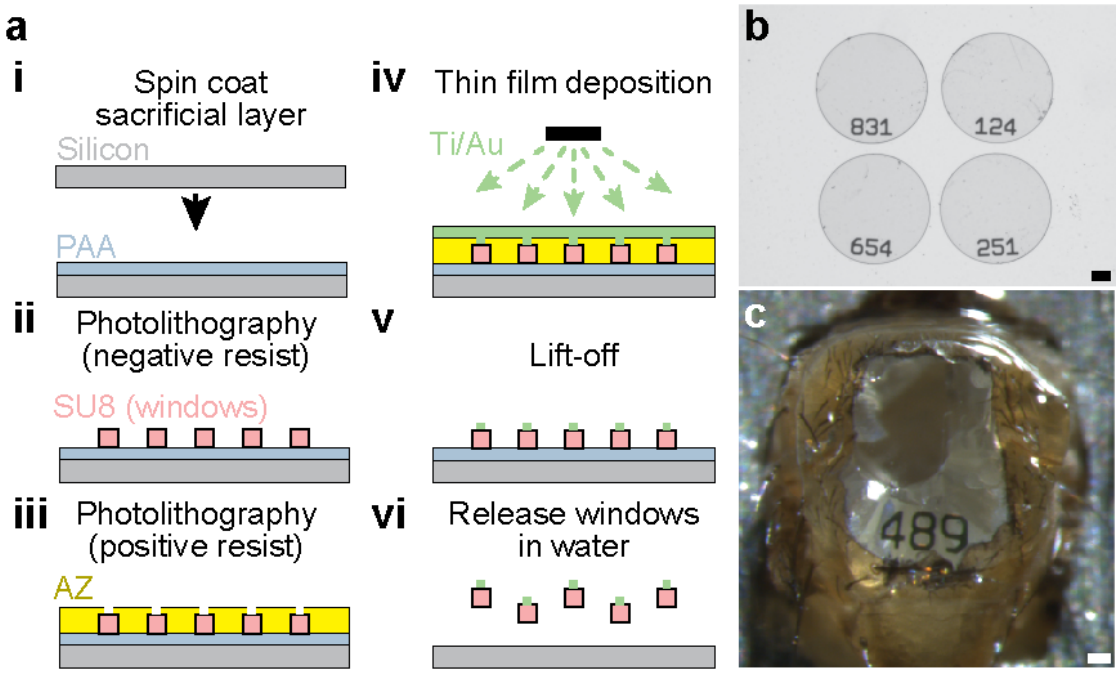

Figure 3.3 – Fabrication of number-coded and optically transparent thoracic windows.a) Thoracic windows are fabricated in the following steps. i) A sacrificial layer of PAA is spin-coated onto a silicon wafer, using photolithography. ii) SU8 windows are structured onto the sacrificial layer. iii) A positive resist, AZ, is crosslinked to mark number openings. iv) Ti/Au is vapor deposited. v) The AZ layer is lifted off. vi) Finally, the numbered windows are released in water. b) This process yields transparent SU8 windows with thin Ti/Au numbers. Scale bar: 100 µm. c) View of a window on an implanted animal, permitting a view of thoracic organs and the tracking of this animal's identity. Scale bar: 50 µm.

Instruments, Germany) and an automatic mask processor (HMR900, HamaTech, Germany). The dimensions of microfabricated structures were measured using an optical microscope (DM8000 M, Leica Microsystems, Switzerland) or a mechanical surface profiler (Dektak XT, Bruker Corporation, USA). The protocol began with treatment of the surface of a 4-inch silicon wafer with a plasma stripper (PVA TePla 300, PVA AG, Germany) at 500 W for 5 min to reduce its wettability. An aqueous solutions of 25% (wt/vol) Poly(acrylic acid) (Polysciences, MW 50000) was spun at 2000 rpm (WS-650-23, Laurell Technologies Corporation, USA) to form a 1 µm thick sacrificial layer for the gentle release of windows at the end of the fabrication process (Figure 3.3a-i). A negative photoresist (SU-8 3025, Kayaku Advanced Materials, USA) was directly spin-coated on the sacrificial layer and soft-baked (Figure 3.3a-ii). After exposure, the windows were post-baked and uncured resist was removed with a developer (Propylene glycol methyl ether acetate (PGMEA, 1-methoxy-2-propanol acetate), Sigma-Aldrich, Germany) (Figure 3.3a-iii). Next, the wafer with SU-8 windows was coated with a 15 µm thick layer of positive photoresist (AZ 40XT) using an automated processing system (Süss, ACS200 Gen3). This extra layer of polymer serves as a physical mask during the metal deposition process. A second chrome mask was fabricated to pattern unique identifiers onto the windows

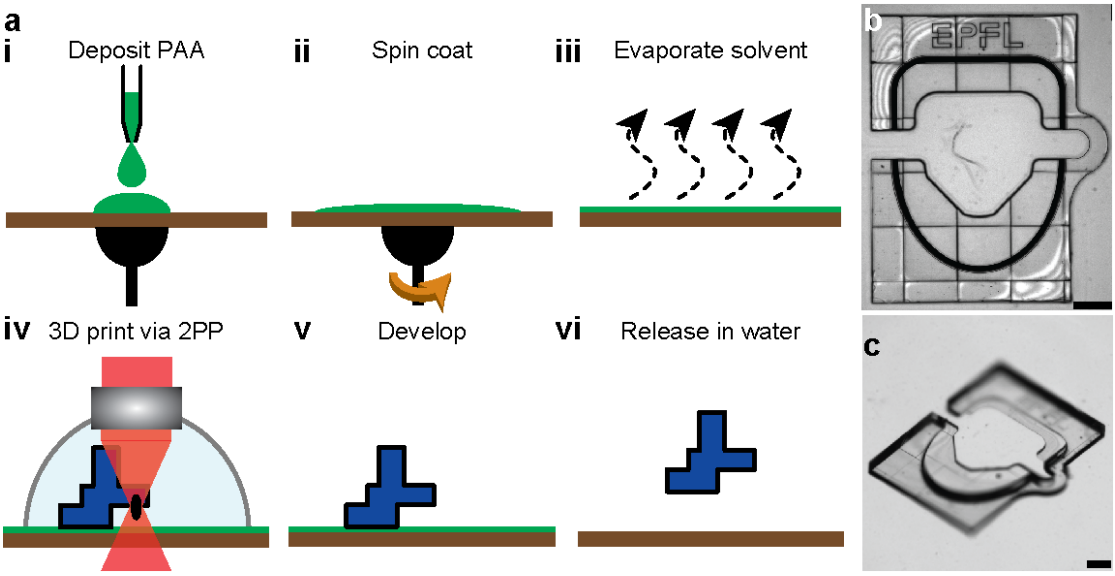

Figure 3.4 – Fabrication of remounting stage. a) A water soluble sacrificial solution is i) deposited and ii) spin-coated to ensure a thin layer. iii) The water in the solution is evaporated, leaving a dry water soluble layer. iv) The 3D remounting stage is printing using 2-photon polymerization. v) This is followed by development in a solvent. vi) Finally, the piece is released in water. b) A microscope image of the remounting stage before releasing it in water. Scale bar: 0.25 mm. c) An alternate perspective visualization of the remounting stage that illustrates its ergonomic design for fly tethering. Scale bar: 0.25 mm.

through photolithography. Next, the wafer was coated with Ti and Au films using physical vapor deposition (Alliance-Concept EVA 760) at a thickness of 2 nm and 10 nm, respectively (Figure 3.3a-iv). The development of the negative photoresist (Remover 1165) removed all the layers on top of the windows except for the numbers that serve as markers. Finally, the labelled windows were released by dissolving the sacrificial layer in deionized (DI) water (Figure 3.3a-vi). The windows were filtered, dried at room temperature, and sterilized prior to implantation in animals. The resulting windows were optically transparent (Figure 3.3b) and of the appropriate size to seal thoracic openings (Figure 3.3c).

3.2.4 Manufacturing the remounting stage

We used direct laser writing to fabricate a custom compliant mechanism that holds flies in place during 2-photon microscopy. The mechanism was designed using a 3D CAD software (SolidWorks 2021, Dassault Systèmes, France). A 25 mm x 25 mm diced silicon wafer was used as the substrate upon which structures were printed. The surface of the substrate was plasma treated at 500 W for 5 min and coated with an aqueous solution of 10% (wt/vol) Poly(acrylic acid) (MW 50000, Polysciences, USA) at 2000 rpm for 15 s using a spin-coater (WS-650-23, Laurell Technologies Corporation, USA) (Figure 3.4a-i-iii). The mechanism was fabricated using a direct laser writer (Photonic Professional GT+, Nanoscribe GmbH, Germany) that

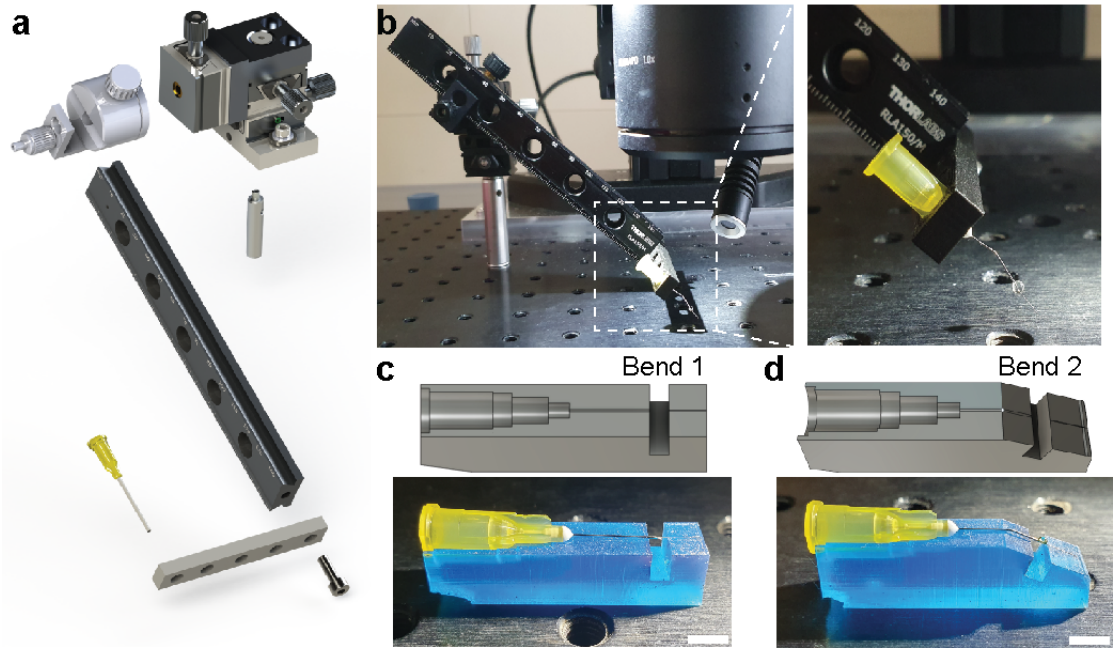

Figure 3.5 – Fabrication of the manipulator arm to displace thoracic organs. a) Exploded view of the manipulator arm and its component parts. b) (Left) View of the manipulator arm mounted near the dissection microscope. (Right) Zoomed in view of the inset (dashed white lines) highlighting the bent needle tip. c) 3D printed piece used to guide gluing of the pin to the syringe needle. Scale bar is 0.5 cm.d) 3D printed piece used to guide the bending of the manipulator arm tip.

operates two-photon polymerization (Figure 3.4a-iv). A polymer (IP-S,Nanoscribe GmbH, Germany) was chosen as the print material due to its Young's modulus of 4.6 GPa [69] and the resolution at which structures could be printed. The overall design was segmented into multiple frames because the maximum laser scan area provided by a 25X objective (NA 0.8, Zeiss) is 400 µm. This approach results in fine printing over a relatively large layout. The objective was dipped into liquid photoresist during printing. At the end of the printing process, the uncured polymer was removed using a developer PGMEA,Sigma-Aldrich, Germany) for 20 min (Figure 3.4a-v). Finally, PGMEA was rinsed with IPA. The mechanism was released from the substrate by dissolving the sacrificial layer in DI water (Figure 3.4a-vi). This yielded a microfabricated structure large enough to contain the thorax of the fly (Figure 3.4b,c). The remounting stage was completed by attaching the mechanism onto a laser-cut aluminum frame using a UV-curable glue (Bondic, Aurora, ON Canada).

3.2.5 Fabrication of a manipulator arm to perform thoracic organ displacement

We designed and constructed a manipulator arm to temporarily displace thoracic organs during implantation (Figure 3.5a,b). To construct the arm, we first 3D printed a mold that allows us to glue a dissection pin (26002-10, Fine Science Tools, Germany) to a syringe needle

(15391557, Fisher Scientific, USA) at a specific length in a reproducible manner (Figure 3.5c). The pin is inserted into the needle until its tip touches the end of the mold. We glued the pin to the needle using a UV-curable adhesive (Bondic, Aurora, ON Canada). The arm was then bent three times using forceps. Then, a second 3D printed mold (Figure 3.5d) was used to guide the locations and angles of each bend. The pin was first bent coarsely and then adjusted more finely using the 3D printed mold. Another 3D printed piece was then used to connect the syringe needle to a 3-axis micromanipulator (DT12XYZ, ThorLabs, USA) and to an extension stage (Figure 3.5a). The whole structure was then attached to a breadboard (MB1224, ThorLabs, USA) (Figure 3.5b).

3.2.6 Implantation procedure

Here we describe the steps required to prepare flies for long-term VNS imaging.

Tethering flies onto the dissection stage

Flies were first cold anesthetized for 5 min. They were then positioned onto the underside of a dissection stage and their wings were ripped off near the base using forceps. The thorax was then pressed through a hole (Etchit, Buffalo, MN) in the stage's steel shim (0.001" Stainless Steel, type 316 soft annealed (McMaster-Carr, part # 2317K11). Afterwards, the stage was turned upside down and a tiny drop of UV-curable glue (Bondic, Aurora, ON Canada) was placed onto the scutellum, to fix the fly.

Opening the thoracic cuticle

The stage was filled with saline solution (Table 3.1). A needle was then used to cut a small rectangular hole (to fit within the 600 μm diameter window) into the dorsal thoracic cuticle. The hole was made by inserting the needle onto the posterior thorax closest to the scutellum. Then three holes were cut into the lateral and anterior thorax. A final line was cut to complete the rectangular opening. The rectangular piece of cuticle was then removed using forceps.

Clearing out thoracic tissues

Residual degraded IFMs were removed using forceps. Then, a pulled (P-1000, Sutter instrument, USA) glass needle (30-0018, Harvard Apparatus, USA) was used to detach small tracheal links between a large left trachea and the gut. The left salivary gland was then removed using forceps.

Chemical	mM
NaCl	103
KCl	3
NaHCO3	26
NaH2PO4	1
CaCl2 (1M)	4
MgCl2 (1M)	4
Trehalose	10
TES	5
Glucose	10
Sucrose	2

Table 3.1 – Saline Solution

Displacing thoracic organs using the manipulator arm

The manipulator arm was positioned on top of the stage with its tip visible. The dissection stage was positioned with the fly's head pointing to the operator. The arm tip was then inserted into the thorax using a 3-axis manipulator (DT12XYZ, ThorLabs, USA). The tip of the arm was then inserted to the (operator's) right side of the gut near the middle of the proventriculus. The tip was inserted deep enough to be below the crop and salivary glands. Once the tip of the arm was on the right side of the salivary gland, crop, and gut, it was pulled to the left side of the thoracic cavity to make space for the closed implant.

Positioning the implant

Once the flies' organs were held onto the left side of the thoracic cavity by the manipulation arm, the implant was closed in the air using forceps and then transferred into the saline solution immersing the dissection stage's shim. The closed implant was then positioned in front of the fly on the stage. A thinner pair of forceps was then used to insert the implant into the animal's thorax. Finally, a glass needle was used to adjust the location of the implant and to keep it at the appropriate height, allowing it to open passively. Once open, the glass needle was used to gently press the left side of the implant towards the bottom of the thorax while the arm was removed.

Sealing the thoracic opening with a transparent, labelled window

Once the implant was well positioned, a syringe needle (15391557, Fisher Scientific, USA) was used to remove saline solution from the stage. A window was then positioned onto the top of the cuticular hole and centered with the identification numbers posterior, near the scutellum. A wire was then used to position tiny drops of UV curable glue between the window and the surrounding dorsal thoracic cuticle, beginning from the right side of the scutellum

and finishing on the left side. Saline solution was then added back to the stage. The cured UV glue, previously tethering the fly to the stage, was finally removed using a needle. The saline solution was then removed and the window was sealed onto the fly's cuticle near the scutellum.

Dismounting flies from the dissection stage

Once the thoracic hole was fully sealed by a transparent window, the fly was dismounted from the dissection stage by gently pushing the front of the thorax through the hole in the steel shim. The fly was then returned to a vial of food to recover.

3.3 Long-term recording technologies and experimental workflow

We developed a microfabricated toolkit and surgical micromanipulation protocol that together enable optical access to the fly's VNS for more than one month. We observed that implanted flies show no obvious deficiencies in their ability to feed, walk, lay eggs, and interact socially with others. (Figure 3.6a). The toolkit consists of two major components: a compliant and transparent V-shaped implant (Figure 3.6b) and a transparent thoracic window (Figure 3.6c). The implants are fabricated *en masse* using soft lithography, a technique that is based on rapid prototyping and replica molding. The window is fabricated from a biocompatible photoresist, SU8, using conventional photolithography. To use these tools, we first tether animals to a dissection stage allowing us to perform a series of surgical operations (Figure 3.6d) [68]. Then, we open a hole into the dorsal cuticle using a syringe needle (Figure 3.6e-i). In the next step, the indirect flight muscles (IFMs) are removed to create space for the implant. To minimize the impact of this surgery, we worked with flies that express the apoptosis-inducing protein, Reaper, in IFMs, resulting in rapid and specific degradation of these muscles (*Act88F:Rpr*) [68]. This genetic manipulation does not degrade all of the IFMs, therefore, we removed the remaining and dead muscle using the syringe needle. Having exposed the thoracic tissues, we then used a fine glass needle and forceps to unilaterally detach the tracheal fibers that connected the gut and the left salivary gland. With the aid of a custom manipulation arm (Figure 3.5), we then pushed the internal organs (e.g., gut, crop, salivary gland and trachea) to the right side of the thoracic cavity (Figure 3.6e-ii, blue) and inserted the implant, preflattened, into the thoracic cavity (Figure 3.6e-iii),(Figure 3.2). Upon releasing the implant, it gradually unfolded until its arms could hold the organs in place against the thoracic wall—after removing the manipulation arm's tip (Figure 3.6e-iv). We then sealed the exposed thoracic cavity by gluing a transparent polymer window to the cuticle (Figure 3.6e-v),(Figure 3.3). Because they have unique numbers engraved on their surfaces, these thoracic windows can be used to identify and distinguish between implanted animals. By removing the UV-curable glue holding the animal to the stage, we can then gently detach flies from the dissection stage.

To facilitate repeated neural imaging of animals who carry the implants, we engineered a remounting stage (Figure 3.6f), (Figure 3.4). The stage is designed to have microscale 3D

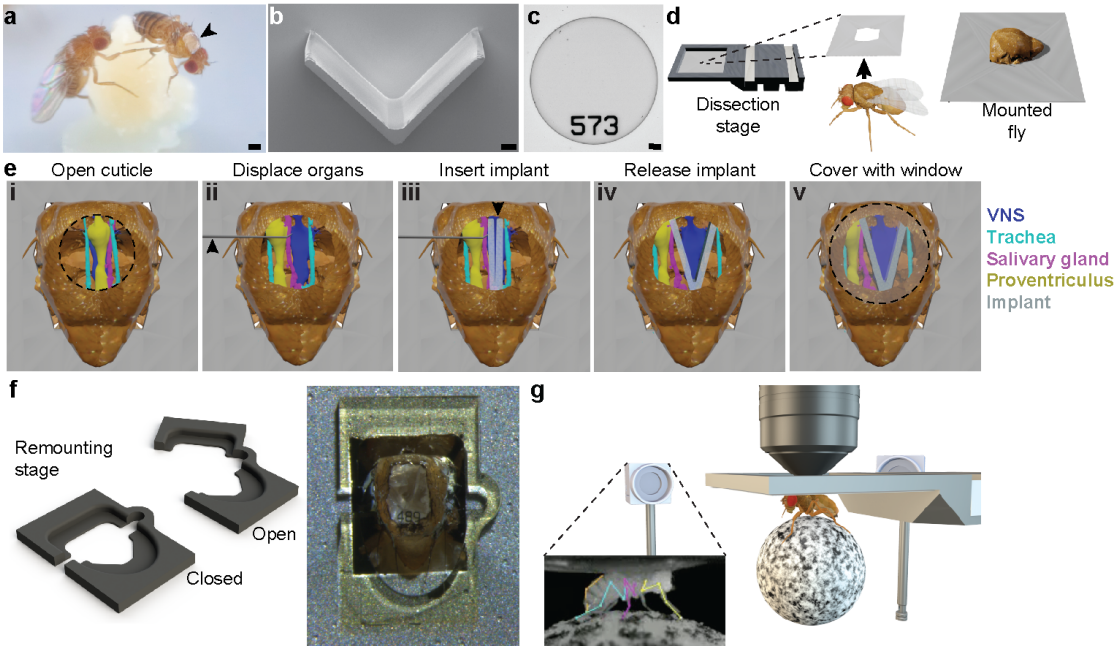

Figure 3.6 – Long-term recording technologies, workflow, and experimental validation. a) Implanted adult flies can be raised in complex environments between neural recordings. Here an implanted animal—see dorsal thoracic opening (black arrow)—interacts with a non-implanted animal. Scale bar: 0.5 mm. b) A mechanically compliant and transparent V-shaped implant microfabricated from PDMS. Scale bar: 50 µm. c) A number-coded, transparent thoracic window microfabricated from SU-8. Scale bar: 50 µm. d) For implantation, an animal is first mounted, thorax first, into a hole in a steel shim within a dissection stage. e) A multi-step dissection permits long-term optical access to the VNS. (i) First, a hole is cut into the dorsal thoracic cuticle, revealing the proventriculus (yellow), trachea (cyan), and salivary gland (magenta) overlying the ventral nervous system (VNS, dark blue). The indirect flight muscles (IFMs) were degraded by tissue-specific expression of Reaper (*Act88F:Rpr*) [68]. (ii) Then, using a custom-designed surgical arm, thoracic organs are displaced, revealing the VNS. (iii) Next, the implant is placed within this thoracic hole in a narrow, mechanically closed configuration. (iv) The arm is removed and the implant is released, causing it to spontaneously open and mechanically push aside organs covering the VNS. (iv) Finally, a transparent SU-8 window is sealed to enclose the thoracic hole. f) A remounting stage permits gentle mounting and dismounting of animals for repeated 2-photon imaging. (left) A flexible microfabricated hinge allows the stage to open and close. (right) Sample image of an animal tethered to the remounting stage as seen isometrically. g) Implanted animals tethered to the remounting stage are placed in a 2-photon microscope system surrounded by a camera array. This configuration permits simultaneous recording of neural activity and animal behavior. Inset shows one camera image superimposed by deep learning-based 2D poses estimated using DeepFly3D [70]. h) (top row) The dorsal thorax of an implanted animal, as visualized from the dissection microscope, and (bottom row) its VNS, as visualized using the 2-photon microscope. The animal expresses GFP throughout the nervous system and is recorded at (left) 3 dpi, (middle) 14 dpi, and (right) 28 dpi. Z-stacks are depth color-coded. Scale bar: 25 µm.

features to reliably hold the flies. We used two-photon polymerization technique, which has the processing accuracy required to print those features. Experiments were performed within a multipurpose system consisting of multiple cameras and software that measured and tracked animal movements and a 2-photon microscope that simultaneously recorded neural activity in the VNS (Figure 3.6g).

3.3.1 Impact of long-term imaging technologies on lifespan and behavior

Having established a suite of long-term imaging technologies, we next assessed their impact on the lifespan of implanted animals. Specifically, we measured the longevity of three groups of animals (n = 40 per group): (i) flies that were not manipulated ('intact'), (ii) flies that endured cold anesthesia, mounting onto the dissection stage, and wing removal ('sham dissected'), and (iii) flies that underwent the full implantation procedure (Figure 3.6e) ('implanted'). We found that implanted flies could survive up to 88 days, an only slight reduction compared with intact animals (Figure 3.6a). Notably, sham implanted flies had a similar lifespan, suggesting that animal handling, and not the implantation procedure, was largely the cause of increased mortality.

Next, we asked whether implantation would have a negative impact on legged locomotion, possibly due to the perturbation of leg-related musculature, or the weight of the implants. Analysis of locomotion can be complicated owing to the variety of gaits depending on walking speed and path tortuosity. Therefore, to enable rigorous quantitative analysis, we triggered a reliable backward walking response in transgenic flies by harnessing the spatiotemporally resolved stimulation capabilities of optogenetics. We could consistently elicit backward walking upon orange-light illumination [71] in flies expressing the light-gated cation channel, CsChrimson [72], in Moonwalker Descending Neurons (MDNs) [73]. We analyzed the locomotor kinematics of intact, sham implanted, or implanted flies behaving in a custom-built arena (Figure 3.7B). The protocol involved first recording spontaneous behaviors for 30 s, and then delivering three consecutive flashes of orange light for 3 s each (Figure 3.7c, pink) interleaved by 10 s without orange light. Upon optogenetic stimulation, animals exhibited a large initial backward velocity that gradually reduced. Translational velocities rapidly returned to baseline levels after the light was turned off. We did not detect any difference in the velocity profiles across experimental conditions when comparing the initial backward acceleration (Figure 3.7d), the total amount of backward walking (Figure 3.7e), (Figure 3.7c, pink), the maximum backward walking velocity (Figure 3.7f), and the duration of backward walking bouts (Figure 3.7g). Taken together, these data imply that fly locomotion does not change due to the implantation procedure, or the presence of an additional thoracic payload.

3.3.2 Imaging Green Fluorescent Protein throughout the VNS over long term

To observe the extent of the optical access of the flies' nervous system, we drove expression of GFP (Green Fluorescent Protein) throughout their nervous system (GMR57C10-Gal4 >

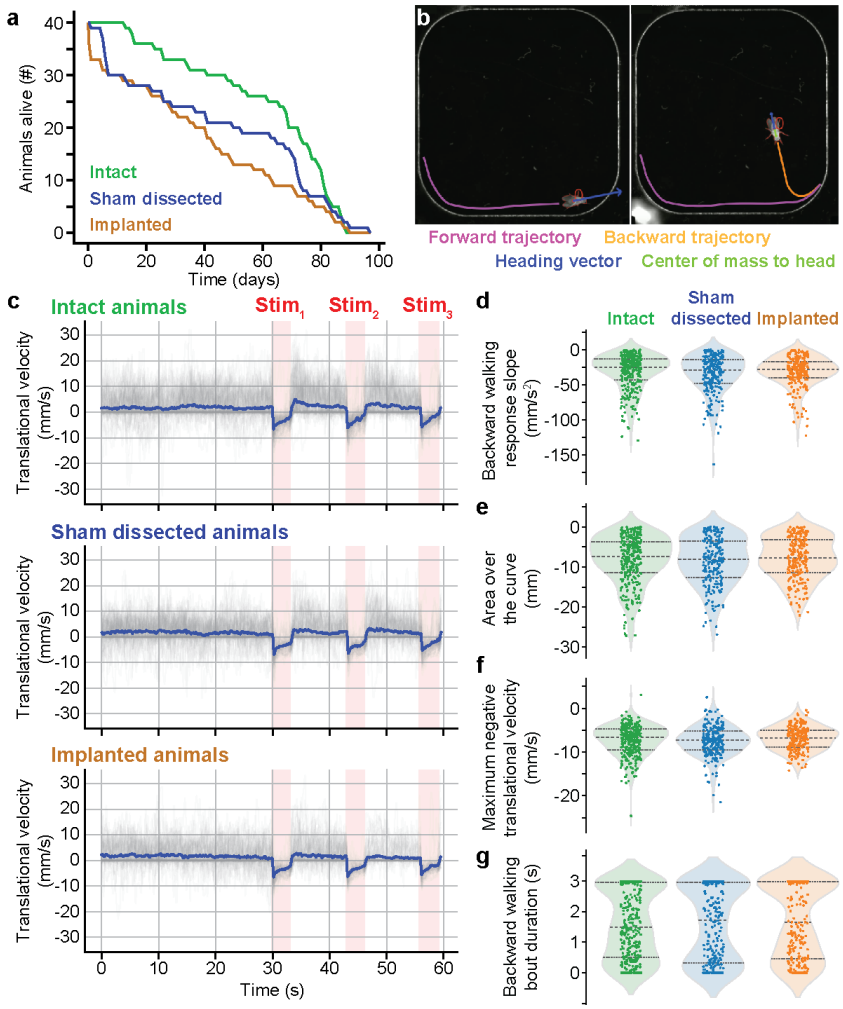

Figure 3.7 – Impact of long-term imaging technologies on lifespan and behavior. a) Survival curves for genetically-identical sibling animals that (i) were not experimentally manipulated (green, 'intact'), (ii) were tethered, and had their wings removed (blue, 'sham dissected'), or (iii) were prepared for long-term imaging by implantation and the addition of a thoracic window (orange, 'implanted'). b) Behaviors were compared by analyzing the dynamics of optogenetically activated backward walking within a rounded square-shaped arena. Locomotion was computationally analyzed and plotted, showing the animal's initial forward trajectory (purple), subsequent optically evoked backward walking trajectory (orange), as well as the associated heading direction vector (blue), and the distance between the head and the center of mass (green). c) Translational velocities of intact (top), sham dissected (middle), and implanted (bottom) animals during 30 s of spontaneous behavior, followed by three optogenetic stimulation periods of 3 s each (pink, 'Stim'). Shown are the raw (grey) and mean (blue) traces. From these time-series, we calculated summary statistics including d) the initial negative slope in translational velocity—backward walking—upon optogenetic stimulation, e) the integrated translational velocity over the entire optogenetic stimulation period, f) the peak negative translational velocity over the entire optogenetic stimulation period, and g) the duration of backward walking bouts during optogenetic stimulation. Shown are the raw data (circles), summary violin plots, and median, upper, and lower, quartiles (dashed lines).

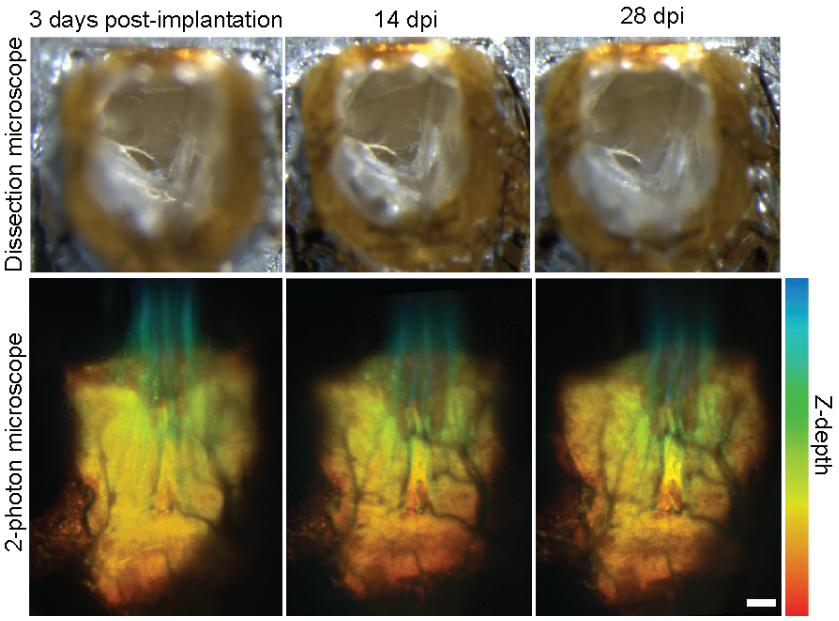

Figure 3.8 – Imaging Green Fluorescent Protein throughout the VNS over long term. Top image: The dorsal thorax of one implanted fly can be observed with its VNS after 3, 14 and 28 days post implantation. (Bottom images) The Green Fluorescent Proteins were imaged with a 2-photon microscope after 3, 14 and 28 days post implantation. Color-coded by depth over 100 µm. Scale bar: 25 µm

Act88FRpr; GFP; +) while also driving reaper – a protein that leads to apoptosis - in the flies' indirect flight muscles. Flies were implanted following the procedure described previously. Flies were kept in individual food vials and mounted on stages 3 times over one month (1-3 days post-implantation (dpi), 14-16 dpi and 28-30 dpi) and their ventral nervous system (VNS) were imaged with a 2-photon microscope. The dorsal thorax of one implanted fly can be observed (top row of Figure 3.8) with its VNS imaged with a 2-photon microscope (bottom row of Figure 3.8). The fly's ventral nervous system remained optically accessible over one month. Our long-term imaging technology allows to record the fly's nervous activity for more than one month and opens up the opportunity to perform a wide range of new experiments such as studying the neural dynamics following a leg injury, studying the neural changes in the VNS of flies at different internal states (for example hungry vs fed flies), studying the loss of neurons in neurodegenerative diseases, studying aging related changes in neural activity, studying plasticity in the neural activity following a learning experiment.

3.4 Discussion

Here we have described a suite of microfabricated technologies that enable long-term imaging of the adult *Drosophila* VNS. These include (i) a micromanipulating dissection arm to displace thoracic organs, (ii) an PDMS-based implant, (iii) a numbered, transparent SU-8 window to seal the thoracic opening, and (iv) a printed hinged microtethering stage that permits repeated

mounting and dismounting of animals for 2-photon imaging. When combined, these tools open the temporal window for recording neural activity in a single animal from a few hours [68] to more than one month. These tools do not markedly impact the lifespan of implanted animals, or perturb their locomotor behaviors. The fact that sham implanted animals had similar lifespans to truly implanted flies suggests that increased mortality was a consequence of not recovering well from the surgical procedure rather than the implantation itself.

Using our microfabricated technologies, we first demonstrated how the morphology of limb mechanosensory neurons could be recorded across a week. Although similar studies have been performed for studies of brain circuit rewiring following injury or stroke, our long-term imaging approach enables the study the reorganization of premotor and motor circuits in the VNS. Additionally, because the previous state-of-the-art approach required the resection of gut and other thoracic organs to visualize the VNS [68], one could not resolve how long term changes in internal state, particularly the effect of hunger state, impact global neural dynamics. However, our method can overcome this gap by visualizing how feeding increases the global activity level of neurons descending from and ascending to the brain.

In summary, our suite long-term imaging technologies permit a wide range of investigations across time in individual animals including an exploration of how aging, injury, learning, internal states, disease progression, social experiences, and drug ingestion impact neural circuit organization and activity dynamics.

4 Mechanical programming of soft micromachines powered by ultrasound

In the previous chapter, the feasibility of implanting microscopic soft structures into living animals has been demonstrated. Those structures were only actuated upon implantation due to stored elastic energy and stayed idle inside the animal. In this chapter, we explore wireless actuation of microscopic implants using pressure waves and air bubbles.

Untethered miniaturized devices administrated via injection, ingestion, or implantation hold great promise for minimally invasive medical operations. Automation is instrumental for operating such devices inside a living organism with accuracy and precision, considering the challenges associated with device localization, physical perturbations, and lack of surveillance. Here, we show that programmed commands can be contained on 3D printed soft micromachines with the introduction of selectively addressable acoustic actuators and monolithic mechanisms constructed from flexible beams. A repertoire of micromachines is designed using experimentally validated computational models that consider dynamic interactions among primary and secondary pressure fields, entrapped air bubbles, and the surrounding fluid. By freely programming the deformation of each beam element, we demonstrate that the micromachines can undergo prescribed motion, which could be reprogrammed on demand with the incorporation of bistable mechanisms. The materials and methods introduced in this study are compatible with in vivo settings, opening the doors to the development of advanced microscopic, injectable, and intelligent devices for biomedical research and clinical therapy.

This chapter is an adapted version of the following work:

Kaynak, M., Dolev, A., and Sakar, M. S., "*Mechanical programming of soft micromachines powered by ultrasound*" (under review).

Author contribution

Kaynak, M., Dolev, A., and Sakar, M. S. designed the experiments,**Kaynak, M.** performed the experiments and analyzed the data, Dolev, A. formulated and implemented the analytical and computational models, **Kaynak, M.**, Dolev, A., and Sakar, M. S. wrote the manuscript, Sakar, M. S. supervised the research.

4.1 Introduction

Injectable microscopic machines and robotic microimplants that can be programmed to operate autonomously inside living organisms can potentially revolutionize minimally invasive medicine[74]–[77]. Considering the challenges associated with remote powering of electrical sensors and actuators at microscale, research has been primarily focused on mechanochemical solutions with a few notable exceptions[78]–[80]. Polymers are particularly suited for the manufacturing of this class of biomedical devices because the final prototype can be entirely soft, biologically inert, and biochemically functional. Active polymer systems that are responsive to external stimuli such as temperature, pH, enzymes, and various physical fields have been extensively explored for controlled delivery of cells and drugs[81]. However, existing macroscale platforms are structured for bulk deformation and, therefore, offer very limited dexterity upon miniaturization. To address this limitation, polymer composites with distributed magnetic or optomechanical actuation have been developed[13], [25], [28], [33], [82]–[84]. Small scale structures with simple shapes display remarkable degrees of freedom and multimodal locomotion, as a result of either the spatial complexity of the magnetization profile or the use of structured illumination[26], [27], [30], [31]. Although very promising for teleoperation, magnetic control techniques face a fundamental challenge in the pursuit of autonomy. The same signal that powers the machine also controls its action, a major limitation for computation and information processing[85]. On the other hand, optical techniques heavily rely on spatiotemporally controlled illumination of actuator units. Considering the capabilities of medical imaging in real-time localization of microscopic devices, an alternative actuation strategy that would enable programmable and adaptive functionalities could become instrumental.

Rationally designed flexible structures can be programmed to execute commands in the absence of electronics, analogous to automata based on gears, cams and bar linkages[86]–[89]. This route for physical intelligence has already been pursued by microorganisms[90], [91], and extensively studied for the development autonomous soft robots[68], [92], [93]. Conveniently, 3D nanoprinters based on two photon polymerization enabled fabrication of micromachines with unprecedented complexity[29], [34], [94]. 4D manufacturing techniques that involve origami self-folding of thin films has expanded the design space[95]–[97]. What has been missing for the realization of a complete microrobotic solution is untethered actuators that can be seamlessly integrated with highly deformable structures and configured to produce a wide range of motions without being constrained by the power signal. Previous work has shown that air bubbles are powerful and efficient wireless microactuators that can generate forces (i.e. thrust and radiation forces) through primary and secondary interactions with the external pressure field, the surrounding fluid, and with each other[98]–[100]. Notably, bubble-carrying microstructures have been energized to move in fluids without constraining their heading, allowing simultaneous control of multiple agents[40], [101]. In other words, it is possible to generate travelling sound waves that do not directly apply force or torque to the machine body but excite the entrapped bubbles in a frequency and amplitude dependent

fashion. So far, in microrobotic applications, this actuation strategy has only been used to propel rigid structures with very limited degrees of freedom[41], [46], [47].

Here, we introduce an integrated design and fabrication strategy for the development of microscopic untethered automata powered by ultrasound. The key innovation is spatial patterning polymer capsules that stably contain gas bubbles along ultraflexible beams using direct laser writing. We, experimentally and computationally, study the physical principles of the actuation scheme by considering complex acoustofluidic interactions and the geometric nonlinearity of compliant mechanisms. We propose a simplified analytical model for the bulk deformation to facilitate the design of complex machinery along with a digital twin of the air-filled polymer capsules to study the dynamics of fluid-structure interactions. We show quantitative agreement between empirical data and simulation results with respect to the effects of the geometry and distribution of bubbles on force generation and deformation. Based on the acquired fundamental understanding, we engineer dexterous soft micromachines that can be set up to follow a predetermined sequence of operations or respond to external instructions provided via ultrasound. While the former form of programmability is achieved by leveraging the sensitivity of acoustic excitation to the characteristics of the input signal, the latter is realized with the use of actuated bistable mechanisms. The materials and methods introduced in this study are compatible with in vivo settings, opening the doors to the development of advanced microscopic injectable devices for biomedical research and clinical therapy.

4.2 Results

4.2.1 Design and fabrication of actuator modules

The actuator module consists of a 3D printed cylindrical capsule with a single circular aperture (Figure 4.1a). We printed all the structures as a monolithic piece from a single biocompatible soft polymer, trimethylolpropane ethoxylate triacrylate (TPETA), using two-photon polymerization Figure 4.1b. Within this capsule, the bubble was physically isolated from the surrounding fluid except at the side of the opening. A drying process nucleated the bubble inside the cavity where the angle at the air-liquid interface was determined by the surface tension Figure 4.1c, which depends on the composition of the fluid and solid boundary conditions at the aperture[102], [103].

Acoustic excitation of a single bubble submerged in liquid generates microstreaming. By entrapping the bubbles inside cylindrical cavities, the oscillations were constrained to a single interface at the opening Figure 4.1d. In this configuration, acoustic streaming generated a pair of counter-rotating vortices and a localized jet, which was captured using high-speed recordings of tracer particles around the actuator module Figure 4.1e. Once an actuator module is connected to a clamped cantilever beam, it is expected to generate thrust along the long axis of the capsule, thereby deforming the structure. By carefully tuning the frequency

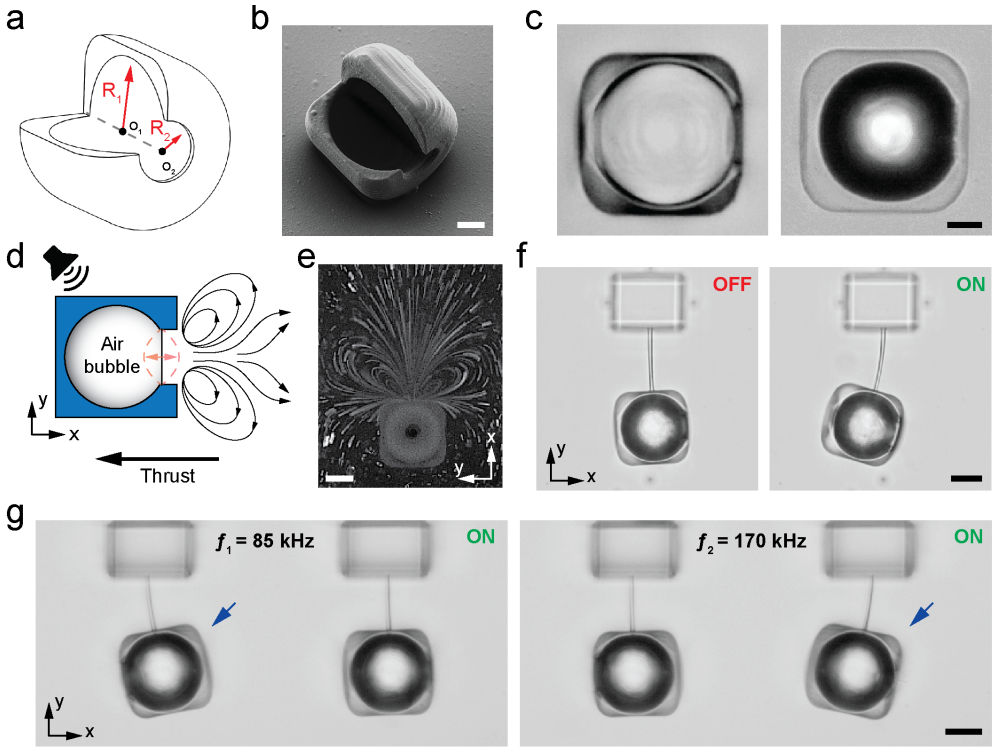

Figure 4.1 – Design, fabrication and operation of acoustic actuators. a) Multiple actuators with differing resonance frequencies are designed by altering inner and opening radii (R_1 and R_2). b) Scanning electron microscopy image shows a partially printed actuator module. Scale bar: 10 µm. c) Representative bright field images before and after air bubble is formed. Scale bar: 10 µm. d) Representative schematics of the actuator module when an air bubble inside the actuator module is excited under acoustic field. e) Flow profile around an actuator module was visualized experimentally. Counter rotating microstreaming on the sides and localized jet in the middle were formed. Scale bar: 20 µm. f) Bright-field images of an actuator module which was linked to an anchor with a beam. The beam was deflected due to thrust generated by the module under acoustic excitation. Scale bar: 20 µm. g) Bright-field images of selectively-actuated modules. Resonance frequencies of the modules was modified by altering opening radii of the actuator. Scale bar: 20 µm.

of the input signal, different vibration modes of the interface can be excited on the same actuator module. Nevertheless, we focused our attention to the first mode because, assuming a uniform pressure over the bubble, the projection of the impinging pressure is maximal at this mode[104]. We modified the diameter of the capsule and the size of the aperture to set the natural frequencies of oscillation of the entrapped bubbles.

4.2.2 Characterization of forces generated by a single bubble

Large deformation and complex motion can be generated with various slender structural elements including beams, plates, and shells[105]–[107]. We based our design methodology

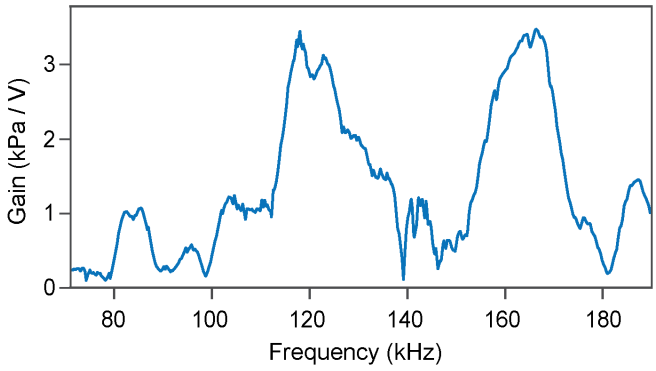

Figure 4.2 – Measured transfer function (TF) produced pressure as a result of input voltage. The gain of the TF, which is the pressure produced by the transducer vs. input voltage is plotted as a function of the frequency. The TF captures the dynamics of the transducer, glass slide, and peripheral electronics. Large TF values indicate optimal excitation frequencies.

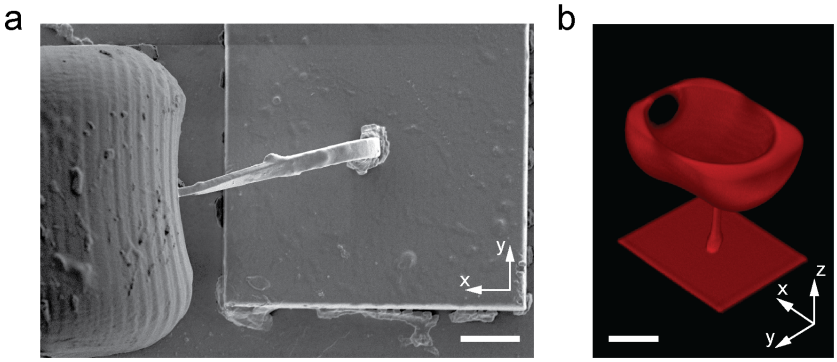

Figure 4.3 – Scanning electron and confocal microscopy images of vertically printed actuator module. a) The size of the beam was confirmed with SEM. Scale bar: 10 µm. b) The vertically printed actuator module was visualized in water using confocal imaging. The top part of the module was excluded to show details. Scale bar: 20 µm.

on flexible beams because they are easier to manufacture, experimentally characterize, and computationally model. The thrust generated by acoustic streaming was strong enough to bend a beam with a cross sectional a of 1.5 µm x 3 µm Figure 4.1f. The first natural frequency of the bubble increases with decreasing aperture size, and this dependency can be harnessed to selectively generate thrust on different actuator modules to deform beams in a programmable way. We first studied the transfer function (TF) produced pressure vs. input voltage spectrum of the ultrasound transducer using a hydrophone to determine the frequency bands at which the microactuators could be effectively powered. Figure 4.2 We have recently developed an analytical model that calculates the natural frequencies and corresponding vibration modes of bubbles entrapped inside arbitrarily shaped cavities and opening geometries. Assuming a fixed inner radius of 30 µm, we estimated the size of the apertures that would force the entrapped bubbles to exhibit their first natural frequencies within these bands. Using this

information, we printed two actuator modules with aperture radii of 7.75 µm and 13 µm. Entrapped bubbles were actuated selectively at their estimated natural frequencies of either 85 kHz or 170 kHz, which led to sequential deformation of the beams Figure 4.1g. The torque applied to the activated beam was adjusted by modulating the amplitude of the applied voltage.

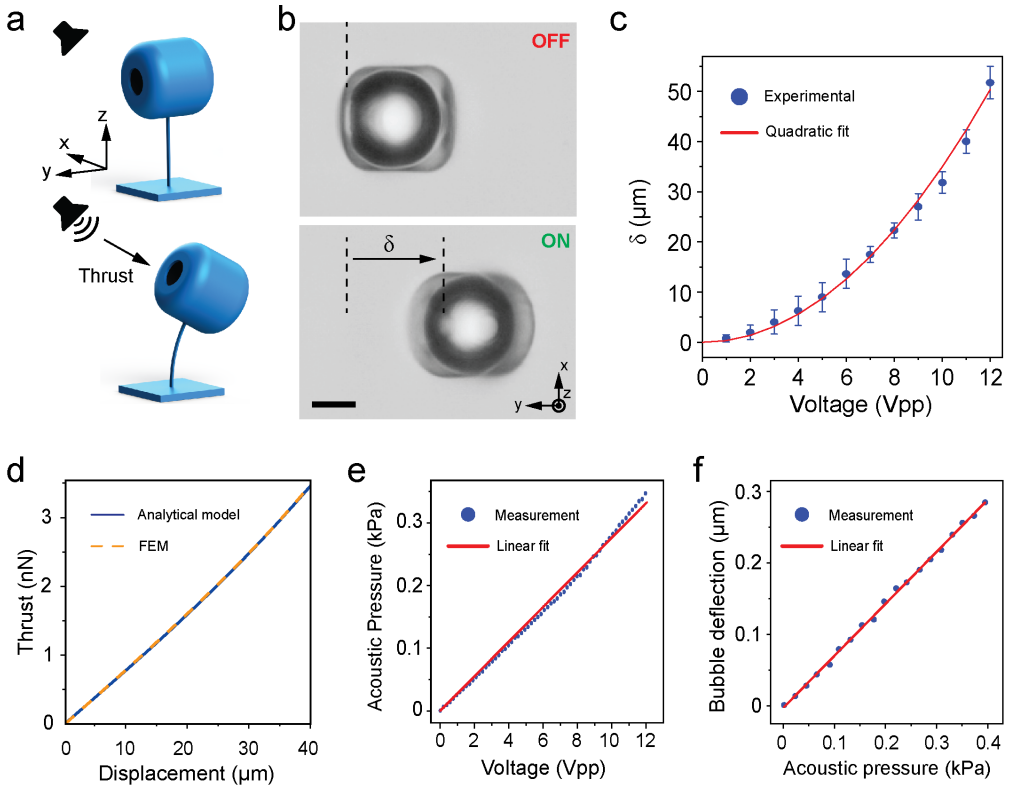

Figure 4.4 – Characterization of a single actuator module under acoustic field. a) Schematics of an actuator module which are designed vertically to minimize the surface bubble interaction. b) Bright-field images show vertically-printed actuators without and with acoustic excitation. The module had net displacement (δ) under acoustic field and immediately returned to its original position when acoustic field was turned off. Scale bar: 20 µm. c) The net displacement exhibits quadratic growth with the applied voltage of the acoustic transducer. d) The thrust was estimated according to an analytical model and a finite element method. Both models, in a good agreement, show that thrust linearly depends on displacement. e) Acoustic pressure linearly depends on applied voltage of the transducer. The acoustic pressure was measured using a hydrophone. f) The amount of deflection at the center of the opening linearly increases with the acoustic pressure. The deflection was measured using a vibrometer.

Printing mechanisms parallel to the substrate is not ideal for the quantification of forces because the bubbles may interact with substrate's surface [46], [47]. In order to minimize such perturbations, we constructed the beams in vertical direction, raising the actuator modules 50 µm above the substrate Figure 4.4a. Laser scanning confocal microscope images of fluorescently labeled samples verified that the structures were printed according to the

CAD design Figure 4.3b. In this configuration, bending of the cantilever beam could be followed from the planar displacement of the actuator module Figure 4.4b, which increased quadratically with the input voltage Figure 4.4c.

4.2.3 Estimating the natural frequencies and vibration modes of an entrapped bubble with a single circular opening

We develop a model of an entrapped gas bubble in an arbitrary shaped confinement, with a circular opening that includes fluid structure interaction (FSI) between the bubble's interface and surrounding fluid. The model builds upon previous models and extends them by combining an optimization stage, to further refine the results by taking into consideration geometrical features in the proximity of the opening, namely the baffling radius. The optimization stage includes the use of the boundary elements method (BEM) to simulate the acoustic field generated by the bubble, and compare it to the analytically computed field.

We focus on natural frequencies and not resonance frequencies for three reasons. First of all, radiation forces and streaming are acoustic phenomena that are driven by the gas-fluid interface velocity while the maximum velocities are obtained at the natural frequencies [108]. Second, the natural frequencies and normal modes are independent of the damping in the systems and, thus, can be treated as inherent characteristics of the linear system. Lastly, as demonstrated by Gelderblom *et al.*[109], resonance frequencies of a gas pocket can be reliably predicted by the potential flow model (i.e., lossless). Regarding the last point, when using modal analysis, the relation between the resonance frequency and natural frequency is $\omega_r = \omega_n \sqrt{1-\zeta^2}$, where ω_r is the resonance frequency, ω_n is the natural frequency, and ζ is the modal damping. Therefore, $\omega_r \approx \omega_n$ when the damping is low (i.e. almost lossless).

Governing equations of motion

The governing equations for the lossless case of a fluid-immersed, entrapped gas bubble with a single opening are derived by following the work of Gelderblom *et al.*[109]. The gas is assumed to be ideal, and the fluid domain is modeled assuming potential flow. We derive the equations for a cavity with a single interface as shown in the Figure 4.5.

Here is a complete list of modeling assumptions:

1. The cavity has circular openings.
2. The interface is pinned to the circular edge of the cavity, only valid for small vibrations.
3. The surrounding fluid is incompressible and inviscid.
4. The interface deflection is much smaller than the opening radius, thus the interface is flat at the equilibrium.

5. Lossless problem.
6. The airflow is negligible.
7. Linear harmonic analysis.
8. Polytropic process in the gas.

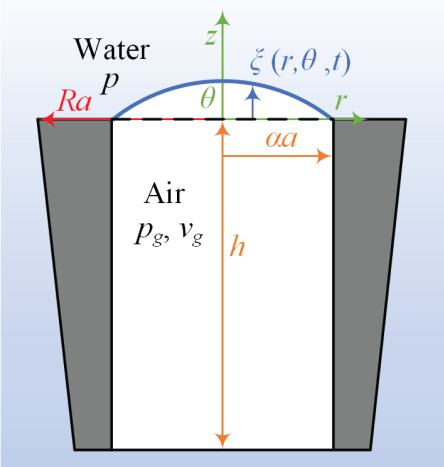

Figure 4.5 – The geometry and parameters used in the the analytical model. An air-filled cavity with a single interface immersed in water. The solid walls entrapping the bubble are denoted with black contour, the solid is colored gray, and the air-water interface is highlighted with s blue line. The local coordinate systems are sketched in green, and the dimensions are given in orange and red.

The local deflection of the interface is described by $\xi(r,\theta,t)$, with a cylindrical coordinate system located on the axis of the cavity's opening. Employing lossless harmonic analysis, the interfaces can be described as:

$$\xi(r,\theta,t) = \xi(r,\theta)e^{j\omega t}, \qquad j = \sqrt{-1} \tag{4.1}$$

The interface motion is coupled to the velocity field in the liquid through a kinematic condition that yields:

$$u_z = j\omega\xi, \qquad \mathbf{u} = u_r\hat{\mathbf{r}} + u_z\hat{\mathbf{z}} \tag{4.2}$$

The boundary conditions for the fluid domain are as follows. On the interface, due to the 4th assumption, and the kinematic condition:

$$u_z\big|_{z=0} = j\omega\xi, \qquad 0 \le r/a \le \alpha \tag{4.3}$$

On the solid surface (z = 0), no penetration and no-slip conditions are denoted as:

$$u_z\big|_{z=0} = 0, \qquad u_r\big|_{r=0} = 0, \qquad \alpha \le r/a \le R \tag{4.4}$$

We ignore the boundary conditions on the cavity walls. The coupling between the pressures in the liquid and the gas occurs via the dynamic boundary conditions at z = 0.

$$p_g = p + \sigma C - 2\mu \frac{\partial u_z}{\partial z}\bigg|_{z=0} \tag{4.5}$$

Here, p_g is the pressure in the gas bubble, p is the pressure in the liquid adjacent to the interface, σ is the surface tension coefficient, C is the curvature of the free surfaces ξ, and μ is the fluid dynamic viscosity. As a result of the 3rd assumption, μ is neglected. Considering small deflections, the curvature for the free surfaces is approximated by

$$C \approx -\left(\frac{1}{r}\frac{\partial \xi}{\partial r} + \frac{\partial^2 \xi}{\partial r^2} + \frac{1}{r^2}\frac{\partial^2 \xi}{\partial \theta^2}\right) \tag{4.6}$$

We assume a general polytropic relation between the instantaneous gas volume V and the gas pressure p_g. Expanding the relation for small volume variations yields

$$p_g = p_0\left(\frac{V_0}{V}\right)^{\kappa} \approx p_0\left[1 - \kappa\left(\frac{V}{V_0} - 1\right)\right] \tag{4.7}$$

where V_0 is the cavity's volume when the interfaces are flat, κ is the gas polytropic index, and $\kappa = 1$ is applicable for isothermal conditions. The instantaneous gas volume can be found from the shape of the interfaces by the following integration:

$$\begin{aligned} V &= V_0\left(1 + \frac{a^3}{V_0}\frac{\int_0^{2\pi}\int_0^{a\alpha} \xi(r,\theta,t)\, r\, dr\, d\theta}{a^3}\right) = V_0\left(1 + \lambda\frac{H}{a^3}\right), \\ H &= \int_0^{2\pi}\int_0^{a\alpha} \xi(r,\theta,t)\, r\, dr\, d\theta, \qquad \lambda = \frac{a^3}{V_0} \end{aligned} \tag{4.8}$$

Substituting Equation 4.7 and Equation 4.8 to Equation 4.5, the dynamic boundary condition becomes

$$p_0 = \left(1 - \kappa\lambda\frac{H}{a^3}\right) = p - \sigma\left(\frac{\partial \xi}{\partial r} + \frac{\partial^2 \xi}{\partial r^2} + \frac{1}{r^2}\frac{\partial^2 \xi}{\partial \theta^2}\right) \tag{4.9}$$

From Equation 4.9 and the first two assumptions, it is intuitive to select the vibration modes of a circular membrane as basis functions for spanning the vibration modes. According to the 3rd assumption, the flow is irrotational, and the velocity field can be written in terms of a velocity potential, $\mathbf{u} = \nabla\phi$.

The following dimensionless quantities are used from here forth without the hat symbol $\hat{\bullet}$.

$$\hat{r} = \frac{r}{a}, \quad \hat{z} = \frac{z}{a}, \quad \hat{\xi} = \frac{\xi}{a}, \quad \hat{u} = \sqrt{\frac{a\rho}{\sigma}}u, \quad \hat{\phi} = \sqrt{\frac{\rho}{a\sigma}}\phi, \quad \hat{t} = \sqrt{\frac{\sigma}{a^3\rho}}t, \quad \hat{p} = \frac{a}{\sigma}p, \quad \hat{H} = \frac{H}{a^3} \tag{4.10}$$

Potential and kinetic energies

The system is considered lossless and Euler-Lagrange equations can be employed to derive the governing equations.

$$d(x) = \frac{d}{dx}\left(\frac{\partial L}{\partial q_1}\right) - \frac{\partial L}{\partial q_1} = 0, \quad l = 1, 2, ..., \quad L = E_\mathrm{k} - E_\mathrm{p} \tag{4.11}$$

where the over dot $\bullet$ indicates a derivative with respect to time t, $\mathbf{q}$ is a set of generalized degrees of freedom (DOF), $\mathscr{L}$, ε_k and ε_p are the Lagrangian, kinetic energy, and potential energy of the system, respectively. The contribution of the irrotational flow near the interface to the kinetic energy is expressed as[110]:

$$E_\mathrm{k} = \frac{1}{2}\int_A \phi\frac{\partial\phi}{\partial\hat{\mathbf{n}}}dA \tag{4.12}$$

where $\hat{\mathbf{n}}$ is a unit vector pointing out of the fluid. Far from the interfaces, the velocity reduces to zero. The impermeability conditions imply that the total kinetic energy can be reduced to

$$E_\mathrm{k} = -\frac{1}{2}\int_0^{2\pi}\int_0^{\alpha}\phi\Big|_{z=0}\frac{\partial\xi}{\partial t}r\,dr\,d\theta \tag{4.13}$$

The potential energy of the system is related to the surface tension and the volume of the microbubble. The potential energy increases as the area of the interface grows and the bubble volume decreases.

$$E_\mathrm{p} = \int_{A_0}^{A} dA - \int_{V_0}^{V}(p_\mathrm{g} - p_0)dV \tag{4.14}$$

Substituting Equation 4.7 and assuming small amplitude variations, the potential energy is

approximated as

$$E_{\mathrm{p}} \approx \int_0^{2\pi} \int_0^{\alpha} \frac{1}{r}\left(\frac{\partial \xi}{\partial \theta}\right)^2 + r\left(\frac{\partial \xi}{\partial r}\right)^2 dr d\theta + \frac{1}{2}\lambda \kappa p_0 H \tag{4.15}$$

To solve the general problem for which R is finite, we first solve for two extreme cases, free ($R = 0$) and baffled ($R = \infty$) bubbles. Notice that the free bubble case is not physical.

The free bubble

To solve the interface displacement fields, we span them using a set of basis functions, which are the vibration modes of a circular membrane [111].

$$\xi(r,\theta,t) = \sum_{m=0}^{\infty}\sum_{n=1}^{\infty} J_{\mathrm{m}}\left(j_{\mathrm{mn}}\frac{r}{\alpha}\right)\left[q_{\mathrm{mnA}}\cos(m\theta) + q_{\mathrm{mnB}}\sin(m\theta)\right],\ m = 0,1,...,\ n = 1,2,... \tag{4.16}$$

Here, J_{m} is a Bessel function of the first kind of order m, j_{mn} is the nth zero of J_{m}, and q_{mnA} and q_{mnB} are time-dependent unknown functions. Because the potential energy depends only on the gas bubble, substituting Equation 4.16 into Equation 4.15 yields Equation 4.17.

$$\begin{aligned}
E_{\mathrm{p}} = \sum_i \Bigg\{ & \frac{\pi}{2}\sum_{m=1}^{\infty}\sum_{n=1}^{\infty}\sum_{q=1}^{\infty} q_{\mathrm{mnA}} q_{\mathrm{mqA}} m^2 F_{\mathrm{mnq}} + \frac{\pi}{4\alpha^2}\sum_{q=1}^{\infty}\sum_{n=1}^{\infty} q_{0\mathrm{nA}} q_{0\mathrm{qA}} j_{0\mathrm{q}} j_{0\mathrm{n}} G_{0\mathrm{nq}} + \\
& \frac{\pi}{8\alpha^2}\sum_{m=1}^{\infty}\sum_{n=1}^{\infty}\sum_{q=1}^{\infty}\left(q_{\mathrm{mnA}} q_{\mathrm{mqA}} + q_{\mathrm{mnB}} q_{\mathrm{mqB}}\right) j_{\mathrm{mn}} j_{\mathrm{mq}} G_{\mathrm{mnq}} \Bigg\} + \\
& \kappa\lambda p_0 2\pi^2\alpha^2 \sum_{n=1}^{\infty}\sum_{q=1}^{\infty} q_{0\mathrm{nA}} q_{0\mathrm{qA}} \frac{J_1(j_{0\mathrm{n}}) J_1(j_{0\mathrm{q}})}{j_{0\mathrm{n}} j_{0\mathrm{q}}}, \\
F_{\mathrm{mnq}} = & \int_0^{\alpha} J_{\mathrm{m}}\left(j_{\mathrm{mq}}\frac{r}{\alpha}\right) J_{\mathrm{m}}\left(j_{\mathrm{mn}}\frac{r}{\alpha}\right)\frac{1}{r} dr, \\
G_{\mathrm{mnq}} = & \int_0^{\alpha} \left[J_{\mathrm{m\text{-}1}}\left(j_{\mathrm{mn}}\frac{r}{\alpha}\right) - J_{\mathrm{m+1}}\left(j_{\mathrm{mn}}\frac{r}{\alpha}\right)\right]\left[J_{\mathrm{m\text{-}1}}\left(j_{\mathrm{mq}}\frac{r}{\alpha}\right) - J_{\mathrm{m+1}}\left(j_{\mathrm{mq}}\frac{r}{\alpha}\right)\right] r dr.
\end{aligned} \tag{4.17}$$

In the free bubble case, the only boundary condition to be satisfied is given by Equation 4.3, and the following potential fields are assumed [112].

$$\phi^{(F)}(r,\theta,z,t) = -\sum_{m=0}^{\infty}\sum_{n=1}^{\infty} \frac{1}{j_{\mathrm{mn}}} J_{\mathrm{m}}\left(j_{\mathrm{mn}}\frac{r}{\alpha}\right)\left[a_{\mathrm{mn}}\cos(m\theta_{\mathrm{i}}) + b_{\mathrm{mn}}\sin(m\theta)\right] e^{-j_{\mathrm{mn}} z}. \tag{4.18}$$

where a_{mn} and b_{mn} are time-dependent unknown functions. To compute them, the derivative of Equation 4.18 with respect to z is computed. By using the boundary condition and the orthogonality properties of the trigonometric and Bessel functions, they are found to be

$$a_{\mathrm{in}} = q_{\mathrm{imnA}}, \qquad b_{\mathrm{mn}} = q_{\mathrm{mnB}}. \tag{4.19}$$

Substituting Equation 4.19 into Equation 4.18, and the kinetic energy for a free bubble becomes

$$E_{\mathrm{k}}{}^{(F)} = \frac{\pi}{2}\sum_{n=1}^{\infty}\frac{\alpha^2 J_1{}^2(j_{0\mathrm{n}})}{j_{0\mathrm{n}}} q_{0\mathrm{nA}}{}^2 + \frac{\pi}{4}\sum_{m=1}^{\infty}\sum_{n=1}^{\infty}\frac{\alpha^2 J_{\mathrm{m+1}}{}^2(j_{\mathrm{mn}})}{j_{\mathrm{mn}}}\left[q_{\mathrm{inA}}{}^2 + q_{\mathrm{mnB}}{}^2\right]. \tag{4.20}$$

The baffled bubble

We assume that the interface displacement field can be spanned by the same basis functions as for the free bubble, and the boundary conditions to be satisfied are given by Equation 4.3 and the impermeability condition of Equation 4.4. To satisfy them, the following potential fields are assumed [109].

$$\phi^{(F)}(r,\theta,z,t) = -\int_0^{\infty}\sum_{m=0}^{\infty}\Phi_{\mathrm{m}}(k)J_{\mathrm{m}}\left(k\frac{r}{\alpha}\right)\left[a_{\mathrm{mn}}\cos(m\theta) + b_{\mathrm{mn}}\sin(m\theta)\right]e^{-kz}dk. \tag{4.21}$$

To compute a_{mn} and b_{mn} the derivative of Equation 4.21 with respect to z is computed, then by using the boundary conditions and the orthogonality properties of the trigonometric and Bessel functions, they are found to be

$$a_{\mathrm{mn}}\phi(h) = \sum_{n=1}^{\infty}\frac{J_{\mathrm{m\text{-}1}}(j_{\mathrm{mn}})J_{\mathrm{m}}(h)j_{\mathrm{mn}}}{h^2 - j_{\mathrm{mn}}{}^2}q_{\mathrm{mnA}}, \qquad b_{\mathrm{mn}}\phi(h) = \sum_{n=1}^{\infty}\frac{J_{\mathrm{m\text{-}1}}(j_{\mathrm{mn}})J_{\mathrm{m}}(h)j_{\mathrm{mn}}}{h^2 - j_{\mathrm{mn}}{}^2}q_{\mathrm{mnB}}. \tag{4.22}$$

Then, the kinetic energy for a baffled bubble is obtained,

$$\begin{aligned}
&E_{\mathrm{kp}}{}^{(B)} = \pi\alpha^2\sum_{n=1}^{\infty}\sum_{q=1}^{\infty}\partial q_{0\mathrm{nA}}\partial q_{0\mathrm{qA}}J_{\text{-}1}(j_{0\mathrm{q}})J_{\text{-}1}(j_{0\mathrm{n}})j_{0\mathrm{n}}j_{0\mathrm{q}}f_{0\mathrm{nq}} + \\
&\frac{\pi\alpha^2}{2}\sum_{m=1}^{\infty}\sum_{n=1}^{\infty}\sum_{q=1}^{\infty}\left(q_{\mathrm{mnA}}q_{\mathrm{imqA}} + q_{\mathrm{mnB}}q_{\mathrm{mqB}}\right)J_{\mathrm{m\text{-}1}}(j_{\mathrm{mn}})J_{\mathrm{m\text{-}1}}(j_{\mathrm{mq}})j_{\mathrm{mn}}j_{\mathrm{mq}}f_{\mathrm{mnq}}, \\
&f_{\mathrm{mnq}} = \int_0^{\infty}\frac{J_{\mathrm{m}}{}^2(k)}{(k^2 - j_{\mathrm{mn}}{}^2)(k^2 - j_{\mathrm{mq}}{}^2)}dk.
\end{aligned} \tag{4.23}$$

The intermediate case

The intermediate case, where $R < \infty$, is a realistic situation that is more relevant to physical scenarios than the free and baffled cases. The potentials should comply with the boundary conditions. However, no analytical potential satisfying all conditions was found. Therefore, we assume that the solution of the intermediate case lies in between the two extreme ones and introduce the following potential:

$$\phi^{(I)} = e^{-\beta(R-\alpha)}\phi^{(F)} + \left(1 - e^{-\beta(R-\alpha)}\right)\phi^{(B)}, \tag{4.24}$$

where β is an unknown coefficient, which is found by solving an optimization problem as described below.

Discretized linear equations of motion

The problem is studied in the framework of linear harmonic analysis. It follows that every arbitrary time dependent function can be described as $F(t) = Fe^{j\omega t}$. Notice that the frequency ω is normalized according to Equation 4.10. Now, to discretize the continuous equations, the coefficient q_{mnA} and q_{mnB} are used as discrete DOF, indicating the participation factor of each basis function. Because the energies hold terms up to the second-order, utilizing the Euler-Lagrange equations yields the discrete linear equations of motion. Similarly, we can directly derive the mass, **M**, and stiffness, **K**, matrices, and write the equations of motion as follows:

$$\mathbf{Mq} + \mathbf{Kq} = \mathbf{0} \tag{4.25}$$

The DOF in **q** can be organized differently, here, we use a finite set of cosine DOF (i.e., q_{mnA}), and order them as follows:

$$\begin{aligned} &\mathbf{q} = \left\{q_{01\text{A}} \;\; q_{02\text{A}} \quad q_{0\text{NA}} \;\; q_{11\text{A}} \;\; q_{02\text{A}} \quad q_{1\text{NA}} \quad q_{\text{M1A}} \;\; q_{\text{M2A}} \quad q_{\text{MNA}}\right\}^T, \\ &m = 0, 1, 2, ..., M, \quad n = 1, 2, ..., N \end{aligned} \tag{4.26}$$

We chose to use only the cosine DOF due to the problem's axisymmetric nature which yields doublet modes[113], [114] (i.e., for each natural frequency where $m > 0$ there is a cosine mode and similar mode shifted in space by $\pi/2$, the sine mode). With this information, the stiffness

and mass matrices can be computed as follows

$$\begin{aligned}
&\mathbf{K} = \begin{pmatrix} \mathbf{K_0} & \mathbf{0} \\ \mathbf{0} & \mathbf{K_m} \end{pmatrix}, \\
&(\mathbf{K_0})_{\mathrm{qn}} = \frac{\pi}{2\alpha^2} j_{0\mathrm{q}} j_{0\mathrm{n}} G_{0\mathrm{nq}} + \kappa\lambda p_0 4\pi^2\alpha^4 \frac{J_1(j_{0\mathrm{q}})J_1(j_{0\mathrm{n}})}{j_{0\mathrm{q}} j_{0\mathrm{n}}}, \\
&(\mathbf{K_m})_{\mathrm{qn}} = \pi m^2 F_{\mathrm{mnq}} + \frac{\pi}{4\alpha^2} j_{\mathrm{mn}} j_{\mathrm{mq}} G_{\mathrm{mnq}}.
\end{aligned} \tag{4.27}$$

$$\begin{aligned}
&\mathbf{M}^{(F)} = \begin{pmatrix} \mathbf{M}_0^{(F)} & \mathbf{0} \\ \mathbf{0} & \mathbf{M}_m^{(F)} \end{pmatrix}, \\
&(\mathbf{M}_0^{(F)})_{\mathrm{nn}} = \frac{\pi\alpha^2 J_1^2(j_{0\mathrm{n}})}{j_{0\mathrm{n}}}, \quad (\mathbf{M}_m^{(F)})_{\mathrm{nn}} = \frac{\pi\alpha^2 J_{m+1}^2(j_{\mathrm{mn}})}{2 j_{\mathrm{mn}}} \\
&\mathbf{M}^{(B)} = \begin{pmatrix} \mathbf{M}_0^{(B)} & \mathbf{0} \\ \mathbf{0} & \mathbf{M}_m^{(B)} \end{pmatrix}, \\
&(\mathbf{M}_0^{(B)})_{\mathrm{nq}} = 2\pi\alpha^2 J_{-1}(j_{0q}) J_{-1}(j_{0n}) j_{0n} j_{0q} f_{0nq}, \\
&(\mathbf{M}_m^{(B)})_{\mathrm{nq}} = \pi\alpha^2 J_{m-1}(j_{mn}) J_{m-1}(j_{mq}) j_{mn} j_{mq} f_{mnq}
\end{aligned} \tag{4.28}$$

The potential given in Equation 4.24 influences only the mass matrix. Once β is calculated, as described in the following section, the mass matrix of intermediate case can be computed. The generalized eigenproblem is then solved to compute the natural frequencies and the normal modes[108].

Intermediate case solution via an optimization problem

For the general case where the bubble lies on a finite plane, an additional parameter, β, is required. To estimate the parameter, we devised an optimization problem that minimizes the error between the analytically and numerically obtained solutions as a function of β. From the analytical solution, we can obtain the natural frequencies, normal vibration modes, and potential fields. Moreover, because potential flow is assumed, the analytical pressure field can be computed as $p^{An} = -j\omega\phi$. We assume a lossless harmonic problem; therefore, the pressure field can be computed numerically using a BEM simulation. The input to the simulation is the interface velocity, which is dictated by the analytically computed vibration modes and natural frequencies, and the output is the pressure field p^{BEM}. The intermediate case can be resolved by minimizing the error between the two fields:

$$\Delta = \sqrt{\frac{\sum \left(p^{An}(\mathbf{x}) - p^{BEM}(\mathbf{x})\right)^2}{\sum \left(p^{BEM}(\mathbf{x})\right)^2}}. \tag{4.29}$$

Computing the natural frequencies and normal modes

We compute the natural frequencies and matching normal modes for the free, baffled, and intermediate cases for several geometries. We begin by analyzing a bubble with a single opening and demonstrate the impact of the geometry and optimization procedure on the simulation results. The values for the model parameters are chosen as follows:

$$\begin{aligned} \sigma = 0.072\ N/m, \quad \kappa = 1.4, \quad \rho_{\text{water}} = 998.24\ kg/m^3, \quad c_{\text{water}} = 1481.4\ m/s, \\ p_0 = 101325\ Pa, \quad h = 150\ \mu m, \quad a = 20\ \mu m, \quad R = 1.1. \end{aligned} \tag{4.30}$$

We reduced the computation time while maintaining a sufficient level of accuracy by truncating the basis function series and selecting $M = 4$ and $N = 3$. The truncated series provided accurate predictions of all the modes up to the third axisymmetric mode. The mode shapes of the baffled case are shown in Figure 4.6, which are almost identical to the mode shapes of the free case.

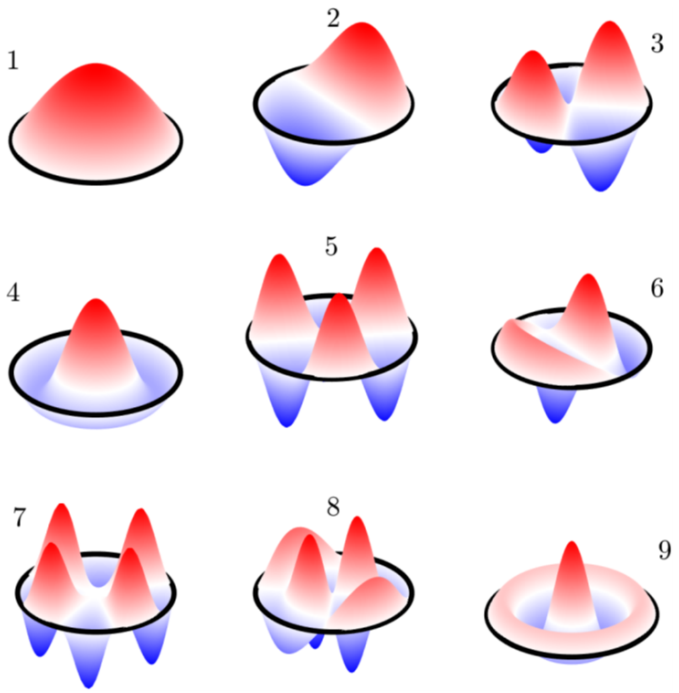

Figure 4.6 – First nine analytically computed normal vibration modes of the baffled bubble. Modes 1, 4 and 9 are axisymmetric, while the rest are not. For each non-axisymmetric there should be a similar mode shifted in space by $\pi/2$ having the same natural frequency.

We are interested in finding the solution for the intermediate case when R is finite. To this end, the optimization problem is solved using MATLAB's built-in functions from the Optimization and Global Optimization Toolboxes. The acoustic field is simulated using OpenBEM [115] according to the selected mode(s), where the input to each simulation is the interface

velocity obtained from the modal analysis. By minimizing the error, the optimal value for β is calculated. In general, the obtained results show that the optimization scheme leads to an accurate estimation of the pressure fields by the analytical model. The natural frequencies for the three different cases are given in Table 4.1. The natural frequencies were computed using two optimization schemes. In the first, each mode was estimated separately (i.e., each mode yielded a different value for β). In the second scheme, all the considered modes were computed together (i.e., yielding a single value for β). The results highlight the importance of considering the geometry near the opening of the microbubble. Although, the mode shapes are practically identical, the relative error between the computed natural frequencies can be higher than 33% for the first mode. The relative error reduces below 10% for higher modes, nevertheless the difference remains more than 10 kHz. Notably, the intermediate solution lies in between the two extreme cases, and as R increases, the solution gets closer to the baffled solution. The latter can be rationalized as follows; larger R increases the flow resistance, thus increasing the inertia, which results in lower natural frequencies. We can conclude that the optimization scheme (single mode versus all modes) has a negligible effect on the results, as the maximum obtained relative error is lower than 1.4%. In practice, the uncertainty in the values of the parameters is expected to lead to larger errors.

Mode		1	3	4	8	9
Baffled (kHz)		53.65	162.86	175.26	349.95	360.36
Free (kHz)		71.51	175.87	198.31	369.04	385.44
R=1.1	Single mode (kHz)	57.33	163.85	178.57	351.65	363.48
	All modes (kHz)	57.01	166.01	178.54	354.06	363.51
	R.E. (%)	0.56	1.32	0.02	0.69	0.01
R=2	Single mode (kHz)	55.56	162.86	176.67	350.02	361.58
	All modes (kHz)	55.10	164.27	176.64	351.76	361.68
	R.E. (%)	0.83	0.87	0.02	0.50	0.03
R=3	Single mode (kHz)	54.90	162.86	176.14	349.95	361.11
	All modes (kHz)	54.58	163.78	176.14	351.12	361.20
	R.E. (%)	0.58	0.56	0.00	0.33	0.02

Table 4.1 – Computed natural frequencies.

When realizing this method, it is important to acknowledge the errors that may occur due to the discrepancies between the free and baffled bubble solutions, and related truncation errors. Commonly the first natural frequency is selected as the operational frequency. To compute it, the method assumes that in both extreme cases the mode shape is the same. However, this is not true for all geometries as can be seen in Figure 4.7, which shows, the two first natural frequencies of the extreme cases as a function of the bubble's radius. Beyond $a \approx 48.5$ µm for the baffled bubble and $a \approx 56$ µm for the free bubble, the mode shapes are different. Truncation of the basis function series may lead to similar results; therefore, it is important to perform a proper convergence analysis. Similar errors may occur for higher natural frequencies. This observation was previously reported and justified by Gelderblom et al. [109].

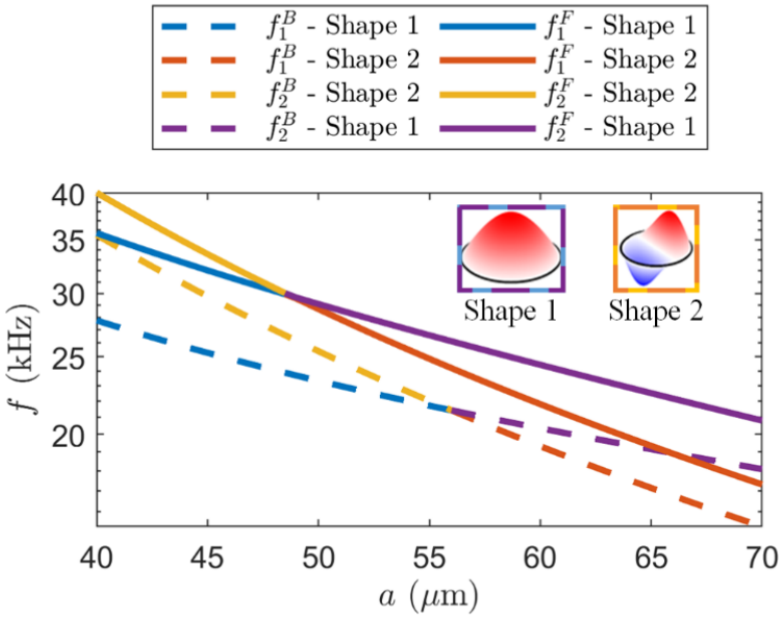

Figure 4.7 – First two natural frequencies and matching vibrations modes shapes as a function of the bubble radius for the baffled (dashed lines) and free (continuous lines) cases.The, two possible vibration mode shapes for both cases exchange their order for different values of the bubble radius.

4.2.4 Computing the beam's stiffness using a linear model

A linear model can be used to compute the beams stiffness by using the experimental parameters.We calculated the bending modulus calculated from the Young's modulus of the material, $E = 13$ MPa[116], and the dimensions of the beam that were measured using electron microscopy Figure 4.3a. Then, we calculated the generated force from the bending modulus of the beam and the measured tip displacement using linear beam theory. We derived the linear stiffness of the beam shown in Figure 4.8 figure below assuming linear material and linear geometry.

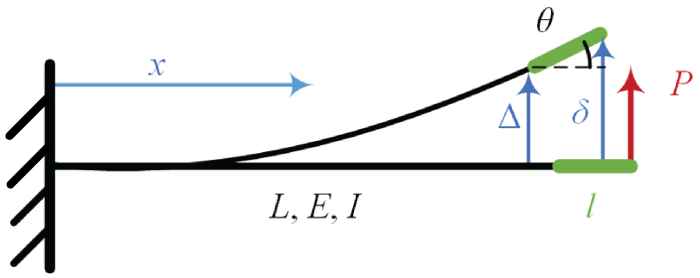

Figure 4.8 – Schematics of the free body diagram to derive linear stiffness of the beam.

The black compartment of the beam is flexible while the green part is rigid. The beam is subjected to a force acting at the end of the beam, P. To solve only the flexible compartment,

we can apply at its end the force P and a moment equal to lP. Therefore, we solve the following linear beam deflection curve:

$$u(x) = a_3x^3 + a_2x^2 + a_1x + a_0 \tag{4.31}$$

The boundary conditions are as follows, at x = 0, the beam is clamped:

$$u(0) = u_{\mathrm{x}}(0) = 0 \tag{4.32}$$

and at its end where x = L, a force and a moment are applied:

$$u_{\mathrm{xx}}(L) = \frac{Pl}{EI}, \qquad u_{\mathrm{xx}} = -\frac{Pl}{EI} \tag{4.33}$$

The solution yields the following deflection curve

$$u_{\mathrm{x}} = \frac{Pl}{6EI}\left[3(l+L) - x\right]x^2, 0 \leq x \geq L \tag{4.34}$$

Therefore, the linear stiffness and slope at the end of the beam are:

$$k = \frac{6EI}{L^2(3l+2L)}, \qquad u_{\mathrm{x}}(L) = \tan(\theta) = \frac{L(2l+L)P}{2EI} \tag{4.35}$$

The total deflection at the end of the rigid beam is

$$\delta = \triangle + l\sin\left[\arctan\frac{L(2l+L)P}{2EI}\right] = \triangle + \frac{lL(2l+L)P}{EI\sqrt{4+\frac{L^2(2l+L)^2P^2}{EI^2}}} \tag{4.36}$$

Since $\triangle = P/k$

$$\delta = P\left[\frac{1}{k} + \frac{lL(2l+L)}{EI\sqrt{4+\frac{L^2(2l+L)^2P^2}{(EI)^2}}} = \frac{LP}{6EI}\left[L(3l+2L) + \frac{6l(2l+L)}{\sqrt{4+\frac{L^2(2l+L)^2P^2}{E^2I^2}}}\right]\right. \tag{4.37}$$

where L is the length of the beam, l is the length of half the actuator module, E is Young's modulus, I is the second moment of inertia of the cross-section and P is the applied force. Although the analytical model is linear, the displacement is a nonlinear function of the applied force because we considered the part of the beam corresponding to the location of the actuator module as rigid.

FEM simulations of a nonlinear model of the mechanism were in perfect agreement with the solution of the analytical model, confirming that the linearity assumption was acceptable for the given range of deflections Figure 4.4d. The linear model was used throughout this work to calculate the total force acting on a deforming beam from the recorded deflection.

We observed a linear relationship between the voltage applied to the transducer and the resultant acoustic pressure measured by a hydrophone Figure 4.4e, as predicted by the theory[49]. The acoustic energy density in the workspace quadratically increases with increasing pressure[117], and so does the streaming velocity around the bubble[41], [47]. As a manifestation of Stokes regime, the actuation completely began and halted within milliseconds after turning on and off the input voltage source, respectively. Furthermore, the beam immediately returned to its original position, confirming that the actuation was in the elastic range. We characterized the amplitude of oscillations at the first natural frequency of the bubble using a custom-built experimental platform. The data showed that the deflection amplitude increases linearly for the range of pressure we applied in the course of this study Figure 4.4f.

4.2.5 Characterization of interaction forces between actuator modules

Acoustically excited bubbles interact with each other through the surrounding fluid when they reside in close proximity. The total force acting on a bubble is the result of the exciting primary pressure field, and higher order fields emanating from neighboring bubbles that also act as acoustic sources[118], [119]. Because the distance between the two bubbles was significantly smaller than the acoustic wavelength, we assumed that the acoustic radiation forces caused by the primary field did not affect the relative displacement of the beams. The secondary forces that act on the coupled beams are thrust, drag induced by acoustic streaming, and acoustic radiation force. Identical bubbles are expected to generate the same acoustic streaming; thus, the generated thrust would push the bubbles away from each other. On the other hand, the amplitude of the acoustic radiation force, which primarily acts to pull the bubbles toward each other, depends on the distance between the bubbles[118], [119]. The total force, F_{B}, acting on a bubble is

$$F_{\mathrm{B}} = F_{\mathrm{R}} + F_{\mathrm{AS}} + F_{\mathrm{d}} \tag{4.38}$$

where F_{R} denotes the acoustic radiation force, F_{AS} denotes thrust generated by streaming, and F_{d} is the drag force acting on a bubble due to the streaming generated by the adjacent bubble.

	Theoretical Freq., f_T,(kHz)	**Experimental Freq., f_E,(kHz)**	**Bubble Radius, R_1,(μm)**	**Opening Radius, R_2,(μm)**
Design 1	122	125	25	10
Design 2	84.9	85	30	13
Design 3	171.8	170	30	7.75

Table 4.2 – Actuator module design parameters

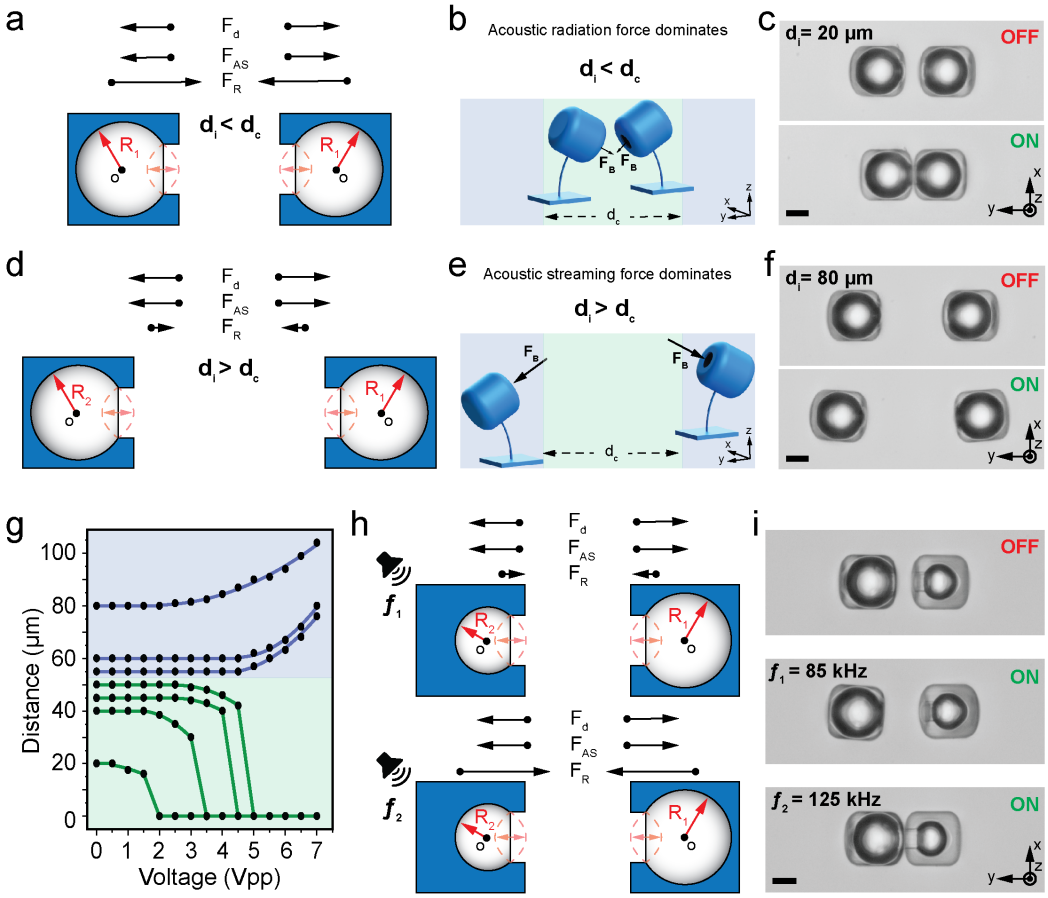

Figure 4.9 – Characterization of acoustic radiation forces between actuator modules. a) Schematics of forces (drag force, F_{d}; acoustic streaming force, F_{AS}; radiation force, F_{R}) which contribute to movement of actuator when initial distance (d_{i}) is shorter than critical distance (d_{c}). Magnitude of forces is not to the scale. b) 3D schematics represents attraction of modules and deflection of beams due to total force (F_{B}) when actuator modules are placed in the critical distance. c) Representative bright field images show actuator modules attracting each other when placed closely. d) Schematics of forces (drag force, F_{d}; acoustic streaming force, F_{AS}; radiation force, F_{R}) which contribute to movement of actuator when initial distance (d_{i}) is longer than critical distance (d_{c}). Magnitude of forces is not to the scale. e) 3D schematics represents repulsion of modules, which in turn deflects beams due to total force (F_{B}) when actuator modules are placed outside the critical distance. f) Representative bright field images show actuator modules repel each other when placed closely. g) The actuator modules either attract or repel each other when the d_{i} is under or above dc, respectively. The shorter d_{i} results in the less voltage until the modules snap in d_{c} area (marked green). Higher d_{i} results in that the actuator modules get far away from each other at lower voltages as they initially placed above d_{c}. All actuator models were excited at 125 kHz. h) Schematics represents that actuator modules with differing volume attract each other when they oscillate in phase or repel otherwise. i) Representative bright field images show identical actuator modules either attract or repel each other at different frequencies even though they are placed closely. Scale bars: 20 μm.

In order to quantify the total force generated by interacting bubbles, we printed two adjacent cantilever beams with identical actuator modules that were faced toward each other (see Table 4.2). The initial distance between the actuator modules, d_i, was systematically varied to study the effect of spacing in force generation. At equilibrium, F_B in Equation 4.32 represent the elastic force applied by the cantilever beam, denoted by P in Equation 4.31. We observed two distinct regimes in the dynamics of the coupled cantilevers. When $d_i < d_c = 50$ µm, the radiation forces dominated the thrust generated by acoustic streaming. (Figure 4.9a) As a result, the beams bent towards each other until the bubbles made contact Figure 4.9b, c. As the initial distance between the actuator modules was increased, the magnitude of the acoustic radiation force was reduced, emphasizing the contribution of streaming forces (Figure 4.9d). As d_i exceeded $d_c = 50$ µm, the sign of the total force switched, where the beams started to move away from each other (Figure 4.9e, f).

Figure 4.9g summarizes the nonlinear responses of coupled cantilevers with respect to the initial distance and the input voltage. The further away the actuator modules were from each other at rest, the more the deflection of the beam pair resembled that of the isolated single beam shown in Figure 4.4c. Based on this empirical observation, we hypothesized that the dynamics could be captured by an analytical model where all forces are proportional to the square of the input voltage[120]. We assumed that F_d did not depend on the distance between the actuator modules, therefore $F_{AS} = F_d$ at all times. This assumption is reasonable as the distance between the bubbles was always in the same order of magnitude of the radii of the bubbles, which was significantly shorter than the acoustic wavelength. We also assumed that the nonlinear change in F_R with distance could be described with an exponent a.[118], [119] The force balance Equation 4.32, is then re-written as:

$$F_B = \alpha V^2 d^a + 2\gamma V^2 \tag{4.39}$$

where α and γ are functions of the excitation frequency, and d is the distance between the vibrating surfaces of the bubbles. We fitted $\alpha = 24.022$, $\gamma = 0.027$ and $a = -1.293$ to the empirical data shown in Figure 4.9g. The model could capture the dynamics represented in the experimental data quite well. This analytical model has been used to design the prototypes presented in the rest of the article.

So far, our data has shown that radiation forces between identical actuator modules does not change sign for a given spacing. For actuator modules with different opening sizes, the interactions became more complex. We discovered that depending on the excitation frequency, modules with the same initial distance attracted or repelled each other (Figure 4.9h). An analogous phenomenon was observed between acoustically excited free-floating spherical bubbles with different radii[118], [119]. Bubbles with distinct natural frequencies oscillate with a relative phase that dictates the direction of the radiation force. When the bubbles oscillate in phase, the force is attractive, and when they oscillate out of phase, the force is repulsive. Therefore, identical bubbles tend to attract each other, and non-identical bubbles can either

attract or repeal each other, depending on the excitation frequency. In our experiments, actuator modules with cavity radii of 25 µm and 17.5 µm attracted or repelled one another at 85 kHz and 125 kHz, respectively (Figure 4.9i).

4.2.6 Programming deformation by patterning actuator modules and modulating input signal

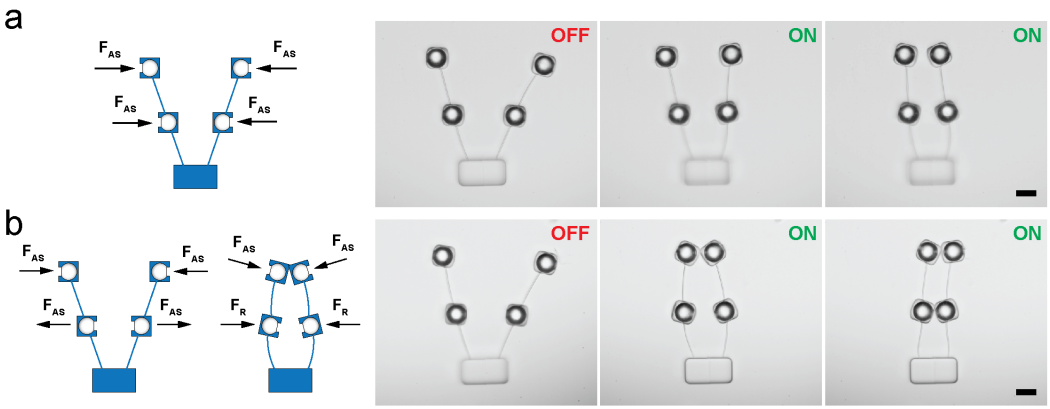

Figure 4.10 – Programming deformation by patterning actuator modules. a) Openings of actuator modules look outside the V-shaped design, which results in sequential closing with increasing input pressure. Scale bar: 50 µm. b) Openings of the actuator modules in the middle look inside. Under the acoustic field, the upper actuator modules close the device while middle actuators repel each other. Middle actuator modules snapped as they get closer. Scale bar: 50 µm.

The dynamics of the presented mechanical systems is very sensitive to the distribution of the bubbles and the properties of the acoustic wave. We postulated that these features could be harnessed for designing micromachines with programmable deformation. As a first proof of concept, we fabricated an arm mechanism with two actuated beams connected to a single base through living hinges, where the beams were free to bend in both directions (Figure 4.10a). In the version where we placed the actuator modules on the outer walls of the beams, the direction of the applied forces did not change with respect to the body frame with increasing pressure (Figure 4.10b). As a result, the arm progressively moved inwards, eventually closing the mechanism. A simple adjustment of moving the two bottom actuators to the interior of the mechanism significantly changed the shape evolution. In this configuration, the bottom actuator pair first generated forces that would move the beams away from each other. The torque applied by the upper actuators was higher, therefore, the arms moved towards each other, forming an oval shape. With decreasing distance between actuators, the acoustic radiation forces generated by the bottom actuator pair increased, switching the direction of the total force acting on the beams. As a result, the beams started to flatten, leading to the full closure of the mechanism.

In the first demonstration, the evolution of morphology was controlled by the amplitude

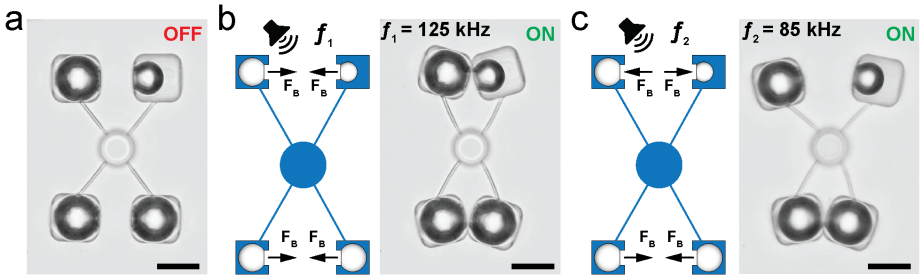

Figure 4.11 – Programming deformation by modulating input signal. a) A bright-field image of two pairs of actuator modules which are connected with beams to an anchor in the middle. Bottom actuator modules are identical while the top actuators had different inner radii; 25 µm and 17.5 µm. b) The actuators were attracted, which in turn deformed the beams at 125 kHz. c) The top actuator modules repelled each other due to out of phase oscillation while the bottom actuator modules kept attraction at 85 kHz. Scale bars: 50 µm.

of the input signal, which modified the distance between the actuator modules. The second characteristic of the pressure wave that could potentially program the forces generated by the bubbles is the excitation frequency (see Figure 4.1g and Figure 4.9i). We designed a flextensional mechanism that leverages this frequency-dependent behavior to manifest multiple distinct deformation patterns on the same system (Figure 4.11a). The two arms of the mechanism simultaneously closed at one frequency (Figure 4.11b), and one arm opened while the other was closing at another frequency (Figure 4.11c). The frequencies at which the mechanism would open or close was determined by the size of the entrapped bubbles. Both modes were independent of the amplitude of the input signal, therefore, the angle between the arms could be tuned with the applied voltage.

4.2.7 Programming deformation through machine design

So far, we focused on a single control paradigm where actuator modules patterned on separate beams were allowed to interact with each other. In this arrangement, rapid increase in radiation forces with decreasing distance limits the range of strain that the actuators can generate. We asked whether we could extend the force interval at which the structure bends in a graded fashion by constraining the motion of the bubbles. To this end, we connected two actuator modules with a truss so that the bubbles were not allowed to come very close to each other (Figure 4.12a). As expected, the arms progressively bent out of plane for a large range of input voltage (Figure 4.12b). To follow the deformation of the arms, we recorded the displacement of the actuator modules along the longitudinal axis (x axis in the diagram) (Figure 4.12b). Although the arms were bending under the dominant effect of the radiation forces, the displacement curve did not follow the highly nonlinear trend presented in Figure 4.9g. We built an FEM model of the mechanism based on the CAD design and the experimentally measured Young's modulus of the material. The magnitude and direction of the radiation force is expected to change as the arms bend due to the change in the interbubble distance.

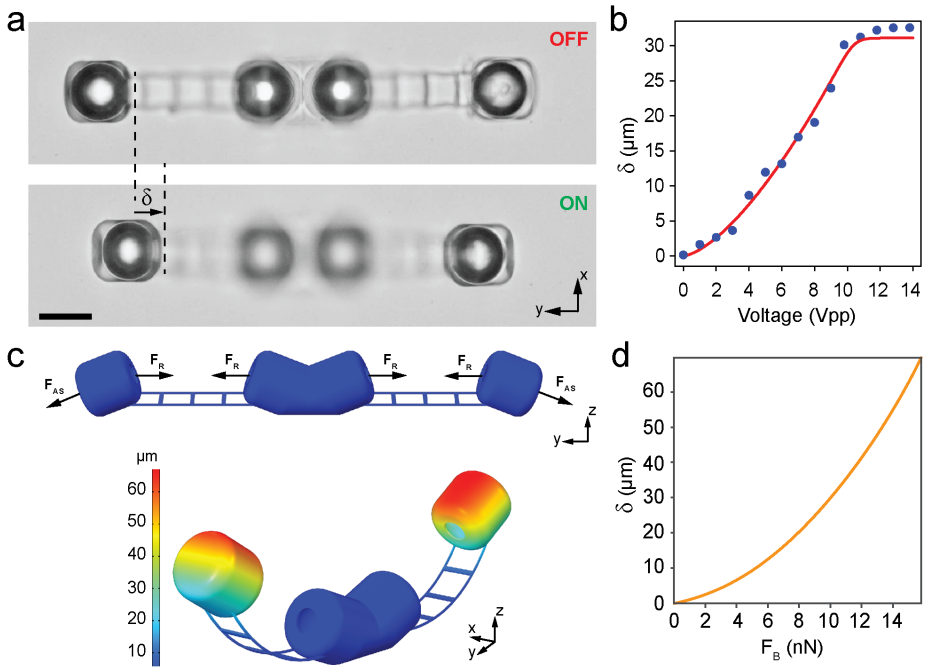

Figure 4.12 – Programming out-of-axis deformation through machine design. a) Two pairs of identical actuator modules were connected with two beams on both sides. The middle two actuator modules were fixed on the ground. They started out-of-axis deformation during ultrasound excitation. Scale bar: 50 μm. b) The displacement exhibited quadratic increase and reached its limit. No snap was observed due to the balance between non-linear beam deformation and acoustic forces. c) FEM results shows the displacement when F_{AS} and F_R is considered. F_d is ignored due to the relatively high distance. d) δ and F_B exhibit the quadratic increase; however, it does not reach the plateau, which can be attribute to F_d as the distance decreases.

We simplified the dynamics by assuming that the radiation force always acted to pull the actuators towards each other and its magnitude was non-linearly dependant to the δ, which is denoted as (Figure 4.12d)

$$F_R = \beta F_{AS} \tag{4.40}$$

We took the thrust calculated for a single actuator module (see Figure 4.4d) as an input and estimated the value of β as 2.25 by fitting the simulated displacements to the empirical data. The simulated radiation forces remained within the range of values recorded for the same voltage. While the arms reach an equilibrium configuration at which increasing voltage further did not lead to more deformation in the experiments (Figure 4.12b), the displacement continued to increase in the simulations (Figure 4.12d). The magnitude of the total force acting on one side of the truss in the FEM model is given by

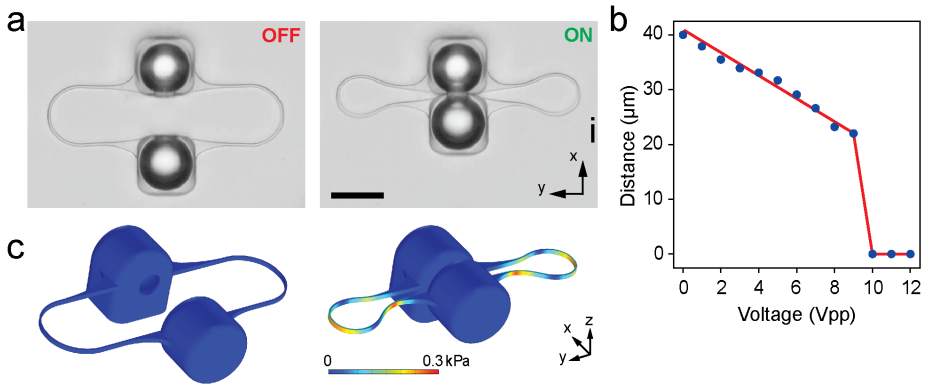

Figure 4.13 – Programming linear deformation through machine design. a) Wireless linear microactuator connected with ultraflexible spring mechanism. The top actuator module was fixed on the ground while bottom one was left free to move in x axis. Scale bar: 50 µm. b) The initial distance between actuator modules decreases linearly with voltage until the snap at 10 V_{PP}. c) Linearly increasing force was applied in FEM model to reach the experimental deformation. The spring coefficient (k) was estimated as 0.763 nN / µm.

$$F_B = | F_B + F_{AS} | \tag{4.41}$$

The plateau observed in the experiments may be a result of the drag force applied to the moving actuator modules by the anchored ones. This force was ignored in the FEM simulations.

Linear actuators generate motion in a straight line. By simply connecting a microbubble pair with an ultraflexible spring mechanism, we developed a wireless linear microactuator (Figure 4.13a). Acoustic forces were primarily uniaxial and, as expected, and we did not observe out of axis deflection during operation. Attractive radiation forces between the two microbubbles caused the gap to narrow and finally snapped the mechanism (Figure 4.13b). The deflection of the spring remained linear with respect to applied voltage until the bubbles were 20 µm apart from each other, at which point the radiation forces snapped the mechanism. When the excitation signal was turned off, the acoustic forces vanished and the stored mechanical energy pushed the suspended body back to its initial position. We built an FEM model of the system from the CAD design and applied the same magnitude of forces that we calculated from the interacting beams as an input (Figure 4.13c). We calculated the stiffness of the spring as 0.7563 nN/µm by computing the derivative of the displacement with respect to the total force.

4.2.8 Programming deformation by harnessing elastic instabilities

Constrained elastic beams can exhibit complex mechanical responses depending on the geometry, degree of confinement, and boundary conditions. Of particular interest for building programmable machines are mechanical instabilities that involve bistability and snap-through.

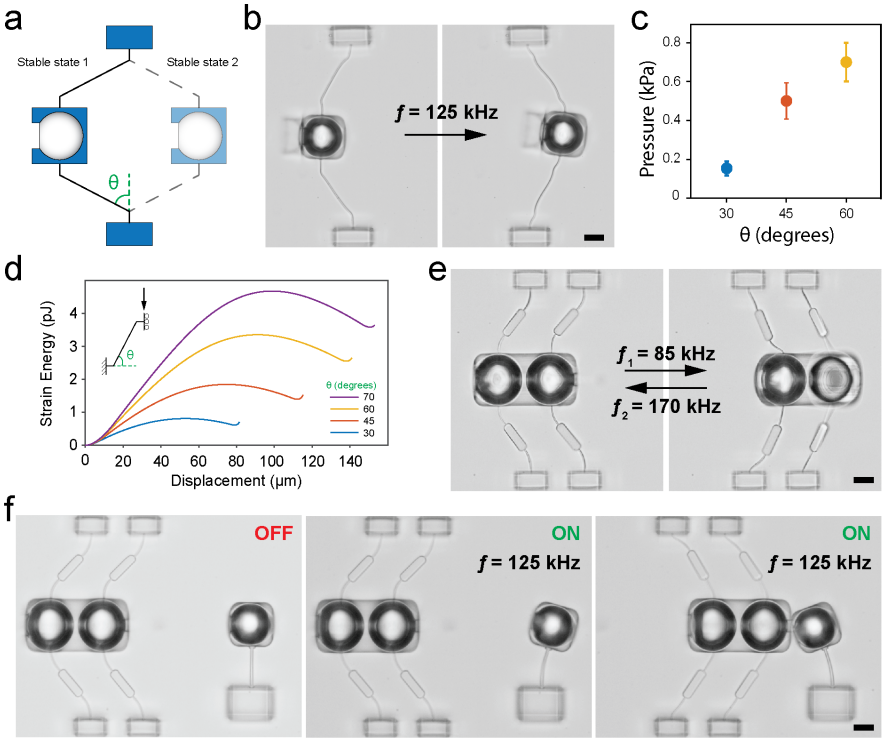

Figure 4.14 – Programming deformation by harnessing elastic instabilities. a) A bistable mechanism was designed using a free actuator module in the middle, anchors on sides and beams to connect thereof. b) The bistable mechanism moved from stable state 1 to stable state 2 as it generated enough thrust at 125 kHz. The mechanism infinitely stayed in both stable states when the actuator was non-excited. c) Necessary acoustic pressure to pass the energy barrier increased with the angle, θ. d) This increase was simulated an in energy landscape diagram, confirming the experimental observation. e) Reversible actuation of a bistable mechanism. The actuators' inner radii are the same (30 μm) while their opening radii are different (13 μm and 7.75 μm). This, in turn, resulted in frequency selective actuation (85 kHz and 125 kHz) and travel between stable states. f) The bistable mechanism was used as a control unit. A single actuator deformed the cantilever beam clockwise due to the thrust (F_T) generated by the actuator when the control module was at stable state 1. The actuator deformed the beam counter-clockwise due to radiation force (F_R) between two actuators. Scale bars: 25 μm.

Bistable structures such as hair clips have two possible equilibrium states where there is no need for actuation to maintain the system in either stable state. Previous work has shown that such mechanisms instantiate embodied logic and programmable functionality in soft machines[68], [121]–[123]. Inspired by these demonstrations, we hypothesized that acoustically actuated beams shaped as constrained curves could serve as wirelessly programmable mechanical control modules. We designed the beam to present a snap-through instability so that application of a relatively small thrust would be sufficient to cross a turning point, and trigger rapid and large deformation towards a second stable configuration.

Key geometric parameters for the design of the curved beams are the inclination angle of the beam, θ, and its slenderness ratio, ω/L, where ω and L denote the width and length of the beam, respectively (Figure 4.14a). The mechanism was driven by a single actuator module that operated in acoustic streaming mode (Figure 4.14b). The beam stayed indefinitely in both stable states, and the thrust generated by the actuator module was high enough to pass the energy barrier. For a fixed ω/L, as θ increases, the input voltage required to switch the state of the mechanism is expected to increase while the deformed position becomes more stable[63]. We fabricated three different prototypes with the same slenderness ratio and varying inclination angle ($\theta = 30°, 45°$, and $60°$) to validate the theoretical predictions. We observed a monotonic increase in the pressure at which the beam managed to switch states (Figure 4.14c). We used a 2D FEM model to obtain the double well potential energy landscape for the same design parameters (Figure 4.14d). The simulation results showed that the strain energy quadrupoles when θ is increased from 30°to 70°, and the displacement of the actuator module is doubled. We calculated the force required to switch the mechanism at different θ from the empirical data using Equation 4.33, where we only considered the thrust generated by a single actuator module (i.e., $F_B = 0.027V^2$). The comparison of these values with the simulated force showed that the switching occurred at lower levels than predicted (Table 4.3). The rationale behind this discrepancy is that the actuator module did not move along a straight line as simulated by the 2D model, and instead moved in 3D by following a more favorable energy landscape.

	Experimental (nN)	**Simulation (nN)**
30 °	1.09	32.53
45 °	8.95	40.5
60 °	16.92	47.76

Table 4.3 – The force required to switch the mechanism at different θ.

We harnessed frequency selective thrust generation to realize reversible actuation for the bistable mechanism (Figure 4.14e). We set the bubble size constant and tuned the aperture diameter of the two actuator modules to be able to activate them at distinct frequencies, 85 kHz and 170 kHz (see Figure 4.1g). Connecting two actuator modules with a single beam to the anchor point proved to be undesirable. To stabilize the structure and ensure reliable operation, we extended the mechanism with additional beams and added support structures in the middle of the beams. The resulting mechanism could be switched repeatedly at the same amplitude and frequency of excitation.

As a final demonstration, we programmed the motion of a continuously bending cantilever beam using an actuated bistable mechanism, which we refer to as the control module (Figure 4.14f, left). Here, triggering the control module completely changes the deformation of the cantilever beam by introducing radiation forces to a system otherwise driven solely by acoustic streaming. To be able to deliver the trigger for the controller and the actuation signal at different frequencies, we engineered actuator modules with varying dimensions. At 125

kHz, the cantilever beam bent in clockwise direction while the control module stayed idle (Figure 4.14f, middle). Exciting the system at 85 kHz activated the bubble on the left of the control module, moving the bubble on the right closer to the actuator module of the cantilever beam. The control module stayed in this stable state upon the removal of the acoustic signal, as expected. At this state, exciting the system again at 125 kHz deformed the cantilever beam in counterclockwise direction due to the attractive forces generated between the two neighboring bubbles (Figure 4.14f, right). In this prototype, the control module must be reset manually because the radiation forces are stronger than the thrust applied by the bubble on the right of the control module. However, a reprogrammable machine could be invented by implementing an actuation strategy like the one introduced in Figure 4.11a. By tuning the aperture and bubble sizes, we may introduce a third frequency at which the interacting bubbles of the control module and the deforming beam would push each other.

4.2.9 Conclusion and Discussion

We developed a suite of micromachines with relatively basic mechanical design. This simplicity facilitated detailed analysis of forces and fluid-structure interactions. The printing technique and the actuation scheme are both compatible with more complex designs that would require scaling down the size of the actuator modules while increasing their number. Furthermore, beams with graded mechanical properties can be printed by either modulating the laser exposure at different sites[124] or using multiple materials[125]. The machines can be built from other flexible structural elements such as plates and shells as these structures also display large deformation and reversible mechanical instabilities. There is an alternative way to augment the functionality of the devices, focusing on the acoustic excitation. We have recently shown that having multiple openings around the entrapped bubble enables generation of multi-DOF actuation using only a single module. The second future direction is considering the interactions between bubbles and solid structures. Sharp edge structures are particularly interesting because they also generate acoustic streaming and radiation forces when excited with ultrasound[126], [127]. We have recently shown that these structures can be printed from biocompatible polymers[128], therefore, they can be readily incorporated into our design framework. Finally, compound machines may be assembled *in situ* from simpler building blocks using radiation forces. Recent work has shown that bubbles can be agglomerated inside blood vessels using ultrasound[38]. This concept may be used to reversibly bring parts together at the target location to perform programmed tasks, analogous to devices assembled using magnetic dipole-dipole interactions [129], [130].

Considering the geometric nonlinearities and the multiphysics of acoustic excitation, finding the optimal design and actuation parameters is not trivial. We developed a simplified analytical model that allows calculation of forces acting on acoustically actuated beam elements. We have also implemented several FEM models to simulate large deformations of more complex structures. These models assumed linear material, and nonlinear geometrical deformations. Under these assumptions, we applied forces which were estimated empirically.

To be able to explore the full capabilities of the presented platform, we developed a realistic FEM model, digital twin, of the actuator modules. The digital twin successfully recapitulated the experimental observations on forces generated by acoustic streaming and bubble-bubble interactions. More on the model and extension.

We focused our attention on geometric arrangements of actuator modules, as a means to program the deformation of the machines. Harnessing frequency selective actuation of bubbles, we could operate the machines in different modes at different frequencies. We have also incorporated acoustically actuated bistable mechanisms as on-board control units to realize machines that can operate in different modes under the same input signal. This last functionality represents a first step towards development of reprogrammable machines, operating analogous to mechatronic systems. To this end, reversible switching of several bistable structures will be instrumental. Frequency selective actuation of bubbles facilitate the implementation of such control systems. The programmable deformation of the machines can be leveraged to build machines with programmable stiffness and strength[65]. Furthermore, although we only studied the equilibrium state of the machines in response to static inputs, the powering scheme is compatible with the application of dynamic pressure. For example, driving the linear microactuator shown in Figure 4.13 at resonance may lead to larger amplitude deflections while keeping the strength of the applied field minimal. To this end, the actuator must be designed in a way that the lowest vibration mode is in the desired actuation direction. Releasing the machines from the tethers will lead to motion, and with the repertoire of compliant mechanisms presented in this study, multimode locomotion can be realized for mobile microrobots.

4.2.10 Methods

Experimental Platform

A piezo transducer (SMMOD15F120, Steminc INC.) was glued in the middle of the cover glass (0.5 centimeter away from the 3D structures) using an epoxy glue (G14250, Devcon). To reduce friction between glass and polymer at the moving parts, a surfactant (3% Pluoronic F-127 in DI water) was applied for 10 minutes. The 3D structures were rinsed with water and dried at ambient temperature. To increase the surface tension for longer bubble lifetime[41], [131], a phosphate buffered saline (25X PBS, ScyTek Laboratories Inc.) solution was dropped onto the devices. A function generator (AFG-2225, GW Instek) and an amplifier (HVA200 THORLABS) were used to control and power the transducer. The microdevices were also excited using water immersion transducers (GPS100-D19 the ultran group) in a custom-made water tank.

3D printing of soft micromachine

Soft microactuators were fabricated with a 3D laser lithography system (Nanoscribe Photonic Professional GT+) equipped with a 63x oil immersion objective (63x/1.4 Oil DIC M27, Zeiss).

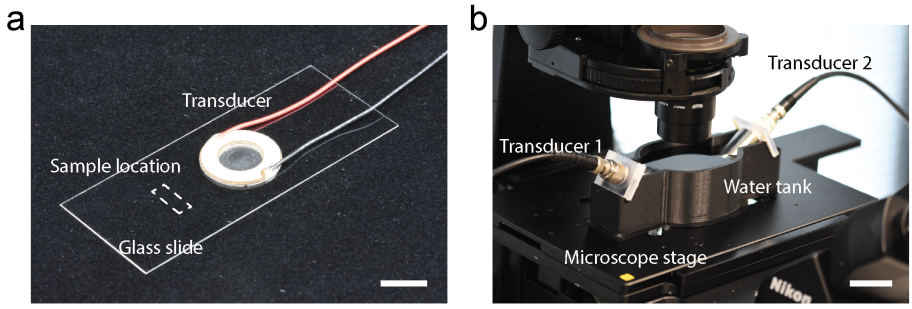

Figure 4.15 – Photographs of the acoustic devices used in this work. a) A pzt transducer is bonded in the middle of the glass slide. The actuator modules are fabricated in the dashed area (1 cm to the transducer). Scale bar: 1 cm. b) Water immersion ultrasound transducers are positioned above the actuator modules in a custom-made water tank. Scale bar: 5 cm.

The polymer was prepared based on a previous publication (Wegener, Sci Adv. 2020). Briefly, a polymer (trimethylolpropane ethoxylate triacrylate (TPETA), Sigma) and a photoinitiator (Irgacure 819, Sigma) were mixed at a ratio of 98:2 (w/w), respectively, and sonicated for 3 hours. For confocal imaging, a fluorescence die (Rhodamine B, Sigma) was added to the solution at a final concentration of 0.5% (w/w). A computer-aided design (CAD) software (Solidworks 2020, Dessault Systèmes) was used to sketch 3D designs. A software (Describe, Nanoscribe GmbH) was utilized to process the design. 3D models were sliced 0.3 µm vertically and 0.2 horizontally. Laser power and scan speed were set to 40 mW and 2 mm/s, respectively. The structures were printed in oil immersion mode on a cover glass (No.1, Cat. No. 470819, Brand). To promote the surface adhesion, the cover glasses were silanized with a solution (3-(trimethoxylsil) propyl methacrylate (Sigma-Aldrich), acetic acid (Sigma-Aldrich), isopropyl alcohol at a ratio of 3:30:1000, respectively) for 1 hour after 5-minute plasma treatment with a plasma cleaner (PDC-32G, Harrick Plasma). The remaining solution was spin-coated at 1000 rpm for 15 seconds using a manual coater (WS-650-23, Laurell Technologies Corporation) and dried on a hotplate (PZ 28-2 ET, Harry Gestigkeit GmbH) at 100 °C for 5 minutes. After printing, the entire devices was developed in a solution (Methyl isobutyl ketone (MIBK) and isopropyl alcohol (IPA) at a ratio of 1:1 (v/v)) for 1 hour. The structures were gently rinsed with IPA and dried.

Pressure and vibration measurements

The pressure in the fluid was measured using a needle hydrophone (RP. ACOUSTIC, PVDF hydrophone type l). The output signal was amplified (RP. ACOUSTIC, HVA-10m-60-F) before it was sampled (pico Technology, PicoScope 5243D). The vibrations measurement were performed using a laser Doppler vibrometer (Polytec CLV-2534). The laser beam was steered using two 45 degrees angled mirrors and coupled to an inverted microscope (Nikon, Ti-2), using a custom built adapters. A high magnification water immersion objective (Nikon, CFI Apo NIR 40X W) was used to reduce the refractive indices discrepancies thus increasing the reflected

light required for the proper operation of the laser vibrometer. To successfully measure the bubble deflection, first the focal plane was adjusted with the microscope stage and verified optically. In the following stage the position of the laser beam was adjusted using the two angled mirrors, and it was focused using the built in focal ring in the sensor's head. The laser adjustment were performed visually using a CMOS camera (BASLER, acA2440-35um) which was connected to the microscope.

Finite element modelling

The commercial FEM software COMSOL Multiphysics 5.6 was used throughout the work to simulate several systems in the time domain, and at steady state. Nonlinear mechanical deformations of solid bodies were simulated using the structural mechanics module, where various constraints and loads were applied. For the digital twin, fluid-gas simulations were performed using the fluid flow module and moving mesh to accurately capture the interface deformation. Both fluid and gas were modeled as compressible and their densities were a function of the pressure [webpage]. The exciting pressure field was applied at the domain boundaries. The twin is realized as a FEM simulation in the commercial software COMSOL Multiphysics 5.6. Due to the multiphysics nature of the simulation it is solved in the time domain, and to reduce the run time, the problem is defined as axisymmetric.

Microscopy and imaging

A high speed camera (VEO640L, Phantom) connected to an inverted microscope (Ti2, Nikon) with a 20x objective (Nikon) was utilized for image and video acquisition. Videos and imaged were postprocessed with Fiji (National Institute of Health). Data were plotted using a commercially available graphing and data analysis software (Origin 2021, OriginLab Corporation). Flow profile of the streaming was visualized using a 1 µm fluorescent beads (Cat # 17154-10, Polysciences). A scanning electron microscope (Merlin, Zeiss) was utilized to capture high resolution images. Confocal imaging was done with an inverted microscope (Zeiss LSM 700) equipped with 20x objective.

Statistical analysis

Results are presented as mean ± standard deviation. Statistical analysis was performed using Origin 2021 (OriginLab Corporation). Data were processed coming from at least three different trials per device and the number of devices tested (n) is at least 4 ($n > 3$) for each condition.

5 Addressable acoustic actuation of 3D printed soft robotic microsystems

As shown in the previous chapter, acoustically excited air bubbles generate relatively high and controllable thrust at microscale. However, there are certain issue related to the use of entrapped bubbles such as stability and manufacturing challenges. In this chapter, we introduce an alternative strategy for wireless actuation that is based on the vibrations of sharp edge structures. Relying on solid structures enables monolithic printing of the whole machine from a single material. The machine performance remains the same over months.

A design, manufacturing, and control methodology is presented for the transduction of ultrasound into frequency-selective actuation of multibody hydrogel mechanical systems. The modular design of compliant mechanisms is compatible with direct laser writing and the multiple degrees of freedom actuation scheme does not require incorporation of any specific material such as air bubbles. These features pave the way for the development of active scaffolds and soft robotic microsystems from biomaterials with tailored performance and functionality. Finite element analysis and computational fluid dynamics are used to quantitatively predict the performance of acoustically powered hydrogels immersed in fluid and guide the design process. The outcome is the remotely controlled operation of a repertoire of untethered biomanipulation tools including monolithic compound micromachinery with multiple pumps connected to various functional devices. The potential of the presented technology for minimally invasive diagnosis and targeted therapy is demonstrated by a soft microrobot that can on-demand collect, encapsulate, and process microscopic samples.

This chapter is an adapted version of the following publication[128]:

Kaynak, M., Dirix, P., and Sakar, M. S. (2020). "*Addressable acoustic actuation of 3D printed soft robotic microsystems*", Advanced Science, 7(20), 2001120.

Author contribution

Kaynak, M., and Sakar, M. S. designed the experiments,**Kaynak, M.** performed the experiments and analyzed the data, Dirix, P. implemented the computational models, **Kaynak, M.**, and Sakar, M. S. wrote the manuscript, Sakar, M. S. supervised the research.

5.1 Introduction

Microfabricated devices have led to revolutionary changes in our ability to manipulate small volumes of fluid and microscopic samples contained therein.[132] As a result, majority of state-of-the-art in vitro biomedical platforms contain microfluidic components. Operating these devices requires the use of bulky pumps, compressors, or tethered electrical powering units, which significantly increase the overall size and limit the portability. A key technological challenge has been the development of untethered microfluidic systems that are capable of providing such functionality with wireless control for in vivo applications. Ideally, such systems are expected to determine the timing, duration, and dosage of the intervention and allow remote, noninvasive, repeatable, and reliable control of diagnostic or therapeutic procedures.[133]–[138] Remote control has been recently achieved with flexible piezoelectric actuators powered by tiny batteries or magnetic induction.[139]–[142] However, the sizes of these electromechanical devices are still in the centimeter range. One potential strategy to address the miniaturization challenge is building automata that operate only with mechanical components. While direct miniaturization of the clockwork mechanisms that power macroscale automata is not a viable option, flexible structures fabricated from natural or synthetic hydrogels possess physical intelligence in the absence of electronic components.[84], [95], [143]–[145] There exists an engine at the heart of every modern machine that is connected to various mechanisms for the controlled application of forces and creation of motion. Development of remotely powered microscopic engines from hydrogels will resolve the aforementioned bottleneck and establish the sensing and actuation capabilities of lab-on-a-chip technology on board an implantable compartmentalized soft microrobot. Two-photon polymerization emerged as a feasible solution for printing polymers in complex forms with nanometer scale resolution.[8], [146], [147] While 3D printed, magnetically driven microscopic screws and gears provide an effective method for mass transport at low Reynolds number,[12], [34], [148] selective magnetization and operation of moving parts require complex manufacturing steps. Furthermore, magnetization scales with volume, thus, microscale structures fabricated from magnetic nanocomposites or polymers coated with magnetic thin films generate very limited thrust and fluid flow. As an alternative strategy, laser power has been harnessed to actuate 3D printed microstructures.[124], [149]–[151] However, focusing the laser beam continuously and precisely at a small region through tissues and organs without causing excessive heating impedes further development.

Bubbles and sharp-edged solid structures excited by acoustic waves generate steady streaming in liquids,[152]–[155] providing a minimally invasive and scalable solution for powering untethered micromachines in vivo.[40], [42], [43], [46], [47] While bubbles are quite efficient in transducing acoustic energy,[41] microrobotic systems actuated by entrapped bubbles work reliable only for hours.[46], [47] The size and mechanical response of bubbles do not stay the same under physiological conditions, thereby gradually shifting the resonance frequency of the actuators and deteriorating the performance of the machine. Furthermore, stable entrapment and precise actuation of multiple bubbles inside a compartmentalized

microrobot is quite challenging due to surface effects. On the other hand, actuation based on specially designed structures provides a durable and versatile solution that delivers the same performance over time and under varying environmental conditions. Previous work demonstrated the feasibility of shaping hydrogels into solid triangular beams using projection lithography inside microfluidic channels and actuating them to drive untethered swimmers and rotors using acoustic waves.[42], [156] However, this fabrication technique does not allow development of morphologically complex dexterous microrobots, restricting its use to on-chip planar manipulation.

Here, we introduce an integrated design and fabrication methodology for the spatiotemporally resolved, frequency addressable acoustic actuation of 3D hydrogel microrobots. Once excited periodically at its resonance frequency, a microstructure with sharp features submerged in fluid generates a pair of counter-rotating vortices and a localized jet as a manifestation of viscous streaming.[157] This principle constitutes the foundation of our actuation methodology. Inspired by the form and ease of operation of macroscale pump-jets, we developed a microjet (μjet) engine that transports fluid through local body deformation without moving parts.

5.2 Results

5.2.1 Fabrication and operation of acoustically excited μjet engines

The μjet engine consists of a cylindrical casing surrounding a conical flexible wedge that was obtained by the 360° rotation of an inclined sharp-edged beam (Figure 5.1a). This axisymmetric configuration ensured zero average torque on the main body during operation while concentrating the synthetic jet along the longitudinal axis. Furthermore, this design scheme allowed all the machine components to be printed as a single piece from a biocompatible hydrogel, poly(ethylene glycol)diacrylate (PEGDA), using two-photon polymerization (Figure 5.1b).

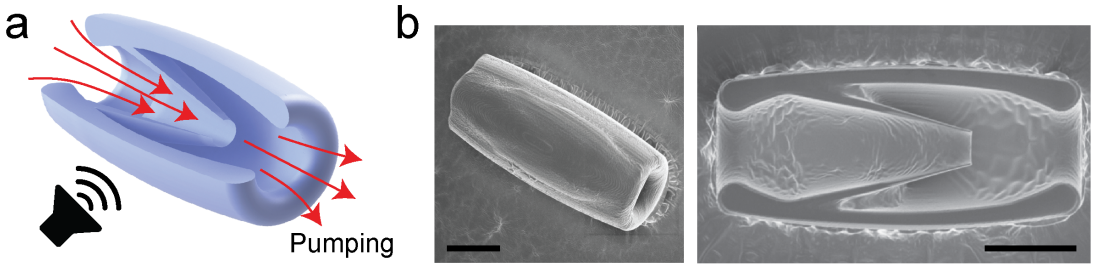

Figure 5.1 – The operation and fabrication of acoustically excited μjet engines. a) Schematic representation of the working principle of the μjet engine. The red arrows show the direction of pumping generated by acoustic streaming inside the device. b) Electron microscopy images showing fully (left) and partially (right) printed μjet engines. Scale bars: 75 μm

Quantitative analysis of the flow generated around the engine is instrumental for the optimization of the pumping performance. This procedure requires robust immobilization of the µjet engine inside a closed test chamber. We fabricated a microfluidic chamber with elastomer pillars that served as ports for the docking of µjet engine (Figure 5.2a). Cross-shaped cavities engraved inside the pillars and T-shaped hydrogel holders printed on both sides of the engine lock the system in place. This configuration resembles the facilities used for testing macroscale jet engines where the engine is mounted on a thrust frame to prevent forward motion. The length of the holder arms was kept long enough to have negligible hydrodynamic interactions between the pillars and the µjet engine. The holders had a nonuniform profile with a thickness starting from 8 µm outside the docking site until reaching the pillars to minimally distort the shape of the engine. We left a minimum clearance of 50 µm between the top of the chassis and the ceiling of the microchannel to avoid formation of underpolymerized sections due to the oxide layer. Parameter sweeps for the laser power and scanning speed were undertaken for successful printing of fine features. At low laser power and high scan speed, the prepolymer solution was not uniformly polymerized everywhere, resulting in differential swelling of the hydrogel. This inhomogeneity-induced residual stress and bending of structures, specifically at the sharp tip. On the other hand, high laser power and low scan speed resulted in overpolymerization, which occasionally led to clogging of the pump. Figure 5.2b shows a representative bright-field image of an engine immobilized inside the microfluidic testing platform.

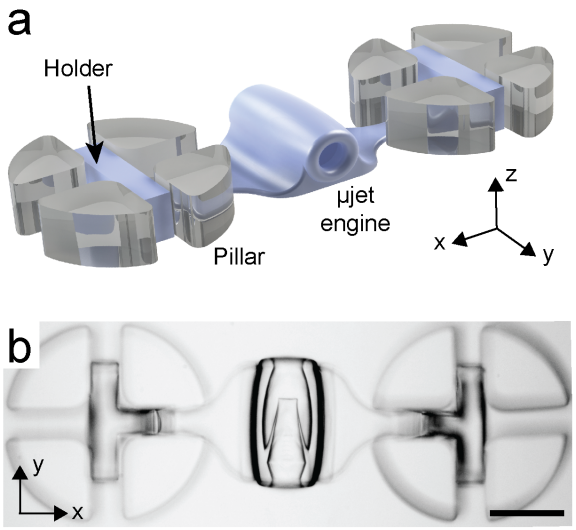

Figure 5.2 – *In situ* fabricated µjet engine in microfluidic test platforms. a) The µjet engine is stabilized using holders inside microfluidic channels. b) Representative bright-field image of a 3D-printed µjet engine that is anchored to pillars. scale bar: 150 µm

We injected 1 µm polystyrene particles into the channel and recorded flow upon acoustic excitation at high frame rates. Streamlines were visualized by rendering temporal projection of images from time-lapse movies (Figure 5.3).

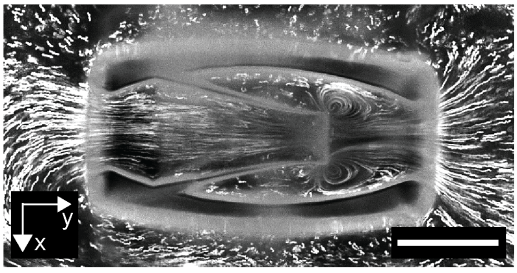

Figure 5.3 – Flow profile inside and around µjet engine a) Streamlines inside and around the µjet engine are visualized experimentally using fluorescent microparticles. Scale bar: 75 µm

Instantaneous flow velocity was extracted from the particle movement in the middle plane of the engine ≈ 30–50 µm behind the sharp tip, a region we denote as the observation site (Figure 5.4a). The flow velocity was tuned by adjusting the intensity of the applied acoustic field, i.e., the voltage applied to the piezoelectric transducer. The flow along the longitudinal axis of the pump reached velocities as high as 476 ± 71 µm s^{-1} at 116 kHz at a peak-to-peak input voltage (V_{PP}) of 55 V in the observation site. As a manifestation of low Reynolds number, the pumping completely began and halted within milliseconds after turning on and off the input source, respectively. The amplitude of the structural oscillations was not large enough to generate pumping below $V_{PP} = 2.5$ V. Above $V_{PP} = 2.5$ V, the pumping velocity at the observation site displayed a quadratic relationship with the input voltage (Figure 5.4b).

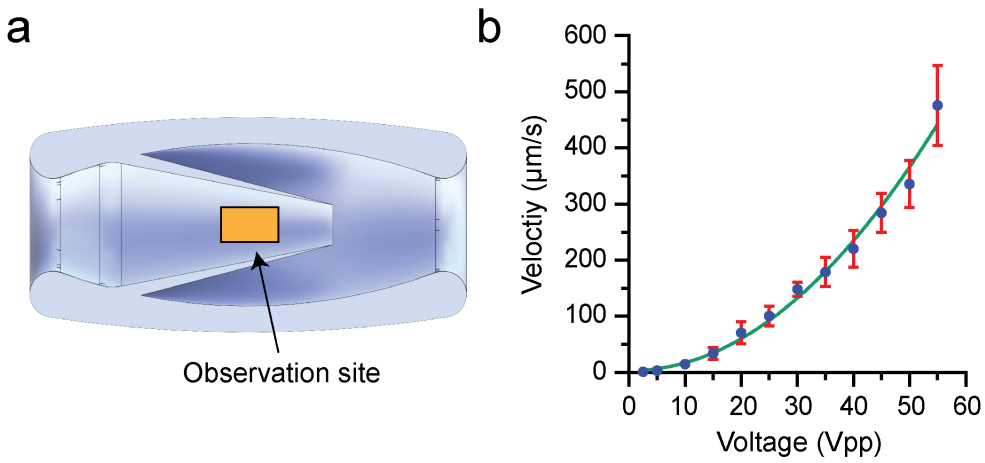

Figure 5.4 – The fluid flows from inlet to outlet along the pump. a) The observation site, where the data is collected, is located between ≈ 30 to 50 µm behind the wedge tip. b) Flow velocity along the longitudinal axis shows a quadratic relationship with the input voltage. Error bars represents the SD of the mean.

A linear relationship exists between V_{PP} applied to the transducer and the generated acoustic pressure. The acoustic energy density in the workspace quadratically increases with increasing pressure [49], [158] while the streaming velocity generated by an oscillating sharp-edged

structure changes linearly with the acoustic power.[155] To explore acoustic streaming around the flexible wedge, we recorded movies of particles at different focal planes. Streamlines showed steady streaming all around the vibrating tip of the wedge, essentially forming a vortex ring (Figure 5.5).

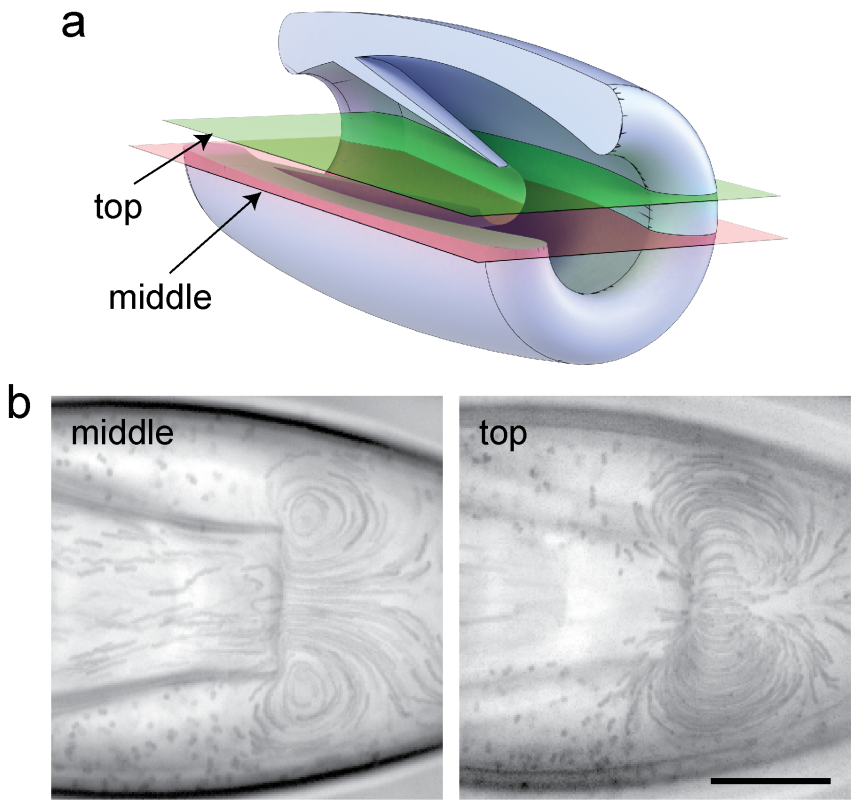

Figure 5.5 – The streaming forms a vertex ring around the tip of the wedge. a) Representative schematic of the layers in the middle and at the top of the wedge. b) The jet in the middle layer results in pumping while couter-rotating vortices on the both sides are in steady state. c) The streaming at the top layer of wedge tip leads to continuous vortices. Scale bar: 25 µm in b).

Numerical modal analysis of µjet engines

We next performed a numerical modal analysis of the µjet engine and associated fluid flows using finite element analysis (FEA) and computational fluid dynamics (CFD), respectively. The analysis was performed on the 3D machines where the influence of the fluid was incorporated to the model through added mass. At certain natural frequencies, the corresponding vibration modes showed large displacement at the tip of the wedge while reporting negligible deformation on the rest of the structure (Figure 5.6).

This particular deformation profile is expected to be optimal for thrust generation, and, thus, we operated the engines around the corresponding frequencies. Solving the Navier–Stokes

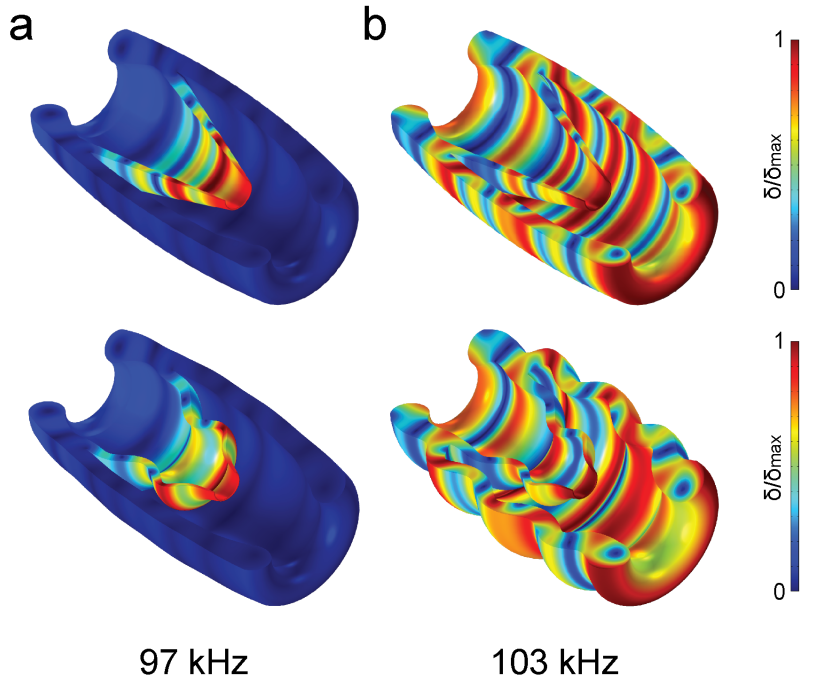

Figure 5.6 – Representative eigenmodes of the pump.a) Displacement localized at wedge leads to fluid flow pumping. b) Dispersed displacement throughout the pump results in unwanted streaming inside and outside of the pump with limited flow pumping. Top panel shows color coding only while bottom panel shows color coding with exaggerated deformation.

equations in 3D requires significant computational power, particularly when considering deformable mesh and moving boundaries. Only axisymmetric modes were considered so that the simulations could be performed on 2D meshes and, as a result, the computational cost of the CFD simulations would be reduced significantly. The simulation framework consisted of a one-way fluid-structure interaction model where the stresses on the structure from the fluid were not considered. For a given eigenfrequency, the eigenmode was extracted from the FEA and applied as a time-dependent displacement condition on the structure boundary (i.e., moving boundary) in the CFD. We tuned the amplitude of deformation and simulated the flow patterns around the oscillating structures. Simulation results captured counter-rotating vortices around the flexible wedge (Figure 5.7) and the flow profile was consistent with experimental data shown in Figure 5.3.

We tuned the displacement of the tip in the computational model to match the empirical fluid flow recorded at 116 kHz, which gave an order of magnitude estimate for the amplitude of structural vibrations. At V_{PP} = 55 V, the empirical value of the flow velocity was 500 µm s^{-1} which corresponds to 0.15 µm tip displacement in the computation model (Figure 5.8).

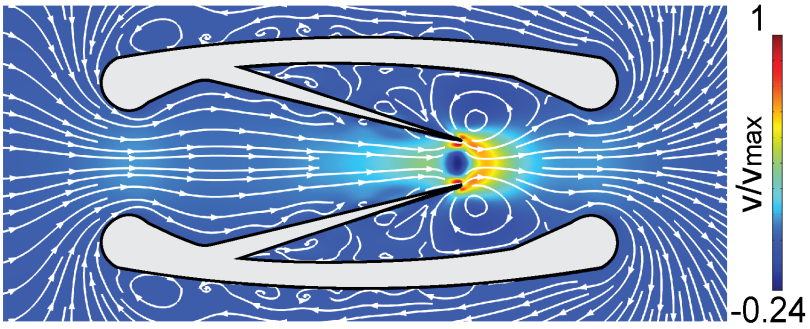

Figure 5.7 – Streamlines inside and around the µjet engine are visualized numerically using CFD simulations.

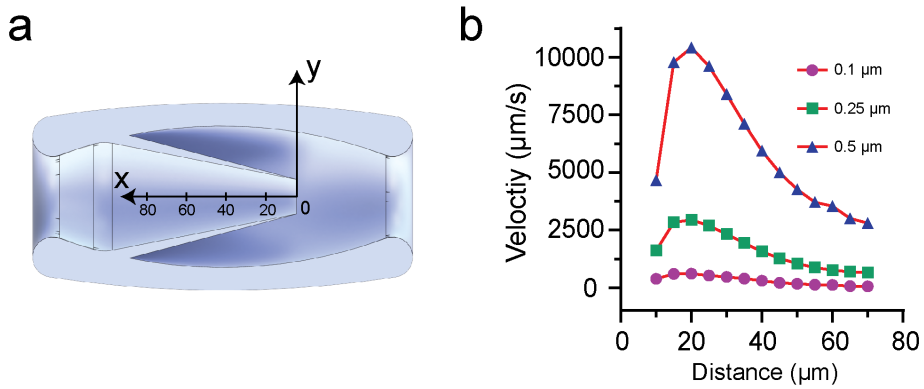

Figure 5.8 – Computational approximation of the tip displacement. a) A schematics showing the axis where the data collected in the middle. b) The flow velocity increases with tip displacement. Additionally, the flow velocity in the x-direction rises up until 20 µm away from the wedge tip. Then, the flow is under the effect of streaming resulting in changes in the flow direction.

Frequency selective actuation of µjet engines

The ability to regulate mechanical power by tuning the amplitude and frequency of the traveling acoustic waves enables the operation of microfluidic systems with multiple engines. We designed two engines with different operation frequencies (i.e., pumping generating eigenfrequencies) by changing the length of the wedge while keeping the opening constant (Figure 5.9a). Both engines were printed together on the same casing with a common outlet. This configuration allowed formation of a cross junction where the profile of the output flow depended on the frequency of the acoustic wave.

Although engines were physically attached to each other, the modal analysis showed that it was feasible to selectively operate engines at different frequencies (Figure 5.9b). Streamlines

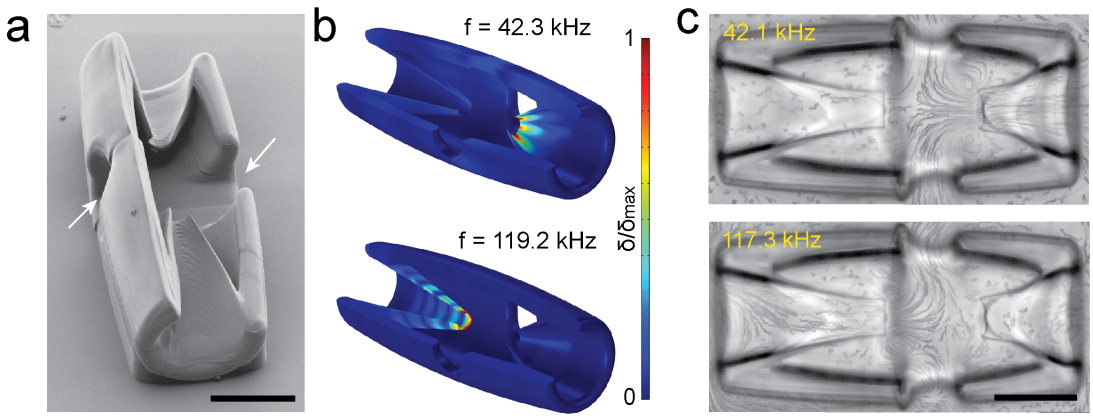

Figure 5.9 – Frequency selective actuation of µjet engines. a)Electron microscopy image of the bidirectional µjet engine. The arrows show the outlets of the pump. b) Numerical simulations show addressable acoustic excitation of the µjet engine within the same device at different frequencies. c) Streamlines showing the flow generated at the resonance frequency of each µjet engine. Scale bars: 75 µm.

recorded at resonance frequencies corresponding to aforementioned vibration modes are shown in Figure 5.9c. Flow velocities recorded at the exhaust of the pumps were $v_1 = 7.64 \pm 1$ µm s^{-1} and $v_2 = 58.6 \pm 3.3$ µm s^{-1} at 42.1 kHz while $v_1 = 37.75 \pm 3.37$ µm s^{-1} and $v_2 = 0$ µm s^{-1} at 117.3 kHz. This frequency dependent transition in flow direction led to an almost digital switch between the two inlet ports.

5.2.2 Fabrication and operation of µthrusters

Microfluidic manipulation systems require not only pumps but also passive and active control elements such as valves and mixers that are seamlessly integrated on the same platform. Expelling mass could provide effective means for the actuation of hydraulic control elements. Macroscale thrusters are propulsive devices used by watercraft for very rapid and accurate control of vessels. They also provide impressive maneuverability with compact and lightweight gear. Inspired by these machines, we engineered amicroscopic thruster (µthruster) in the form of an empty hydrogel container with a single opening (Figure 5.10a). At certain frequencies, the graded structure concentrates the deformation at the opening of the machine much like the flexible wedge of the µjet engine (Figure 5.10b). The jet emanating produces thrust in accordance with the law of conservation of momentum. The streamlines visualized the collection of fluid from the periphery and localized expulsion along the centerline (Figure 5.10c). The rationale behind the formation of a cavity was to reduce the amount of material necessary for printing and increase the amplitude of oscillations at the tip.

Compared to the µjet engine design, µthruster has a significantly smaller footprint, enabling

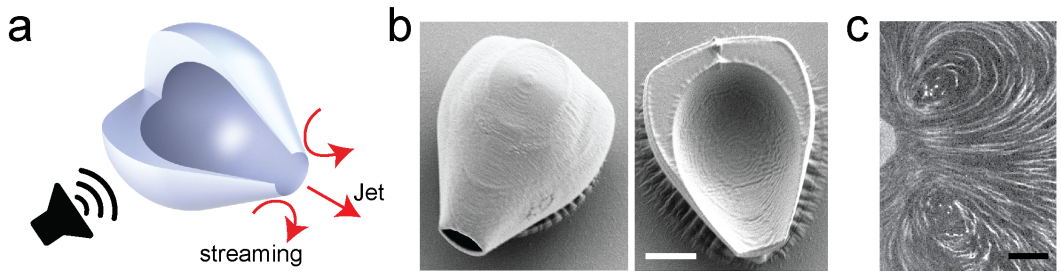

Figure 5.10 – The fabrication and operation of µthrusters. a) Schematic representation of the working principle. The red arrows show the direction of acoustic streaming and jet flow. b) Electron microscopy images of a fully (left) and partially (right) printed devices. Scale bar: 15 µm. c) Streamlines showing counter-rotating vortices at the tip of a µthruster mounted inside the test chamber. Scale bar: 15 µm.

the development of compound micromachines with multiple actuators. We developed a microscale rotor (µrotor) driven by several µthrusters that were arranged around the arms in a way to increase the total torque. The whole system was printed as a single hydrogel piece around an elastomer pillar that served as the shaft for the constrained rotation (Figure 5.11a). We tuned the design of the arm by considering the following tradeoff; thin arms lead to parasitic oscillations during operation while thick arms generate large viscous drag. The angular velocity of the µrotor was proportional to the square of the input voltage or applied acoustic pressure (Figure 5.11b). The angular velocity was as high as 1200 rpm at 5.1 kHz and V_{PP} = 55 V, which is orders of magnitude higher than velocities recorded with magnetic,[12] acoustic,[156] or optical µrotors[150].

The efficient transduction of acoustic energy into mechanical work was due to the relatively high forces generated by acoustic streaming and hydrodynamically favorable 3D design of the engine and the arms of the rotor. We performed experiments to demonstrate that rotation was primarily generated by the µthrusters and not due to bulk streaming in the channel or emergence of standing waves. Once released from the substrate and excited with acoustic waves, µthrusters moved around freely along the opposite direction of the sharp-edged opening, verifying the thrust generation mechanism. In addition, rotors without µthrusters did not respond to acoustic excitation at/around operational frequency from 3 to 6 kHz.

Numerical modal analysis of µthrusters

To study the dynamics of motion, we developed a one-to-one 3D model of the mechanism along with the µthrusters. The flexible body of the rotor has its own resonance modes and some of these modes facilitate the actuation of the µthrusters through vibration of the arms (Figure 5.12a). At higher frequencies, the arms showed much less movement while deformation was observed primarily at the tip of the µthrusters (Figure 5.12c).

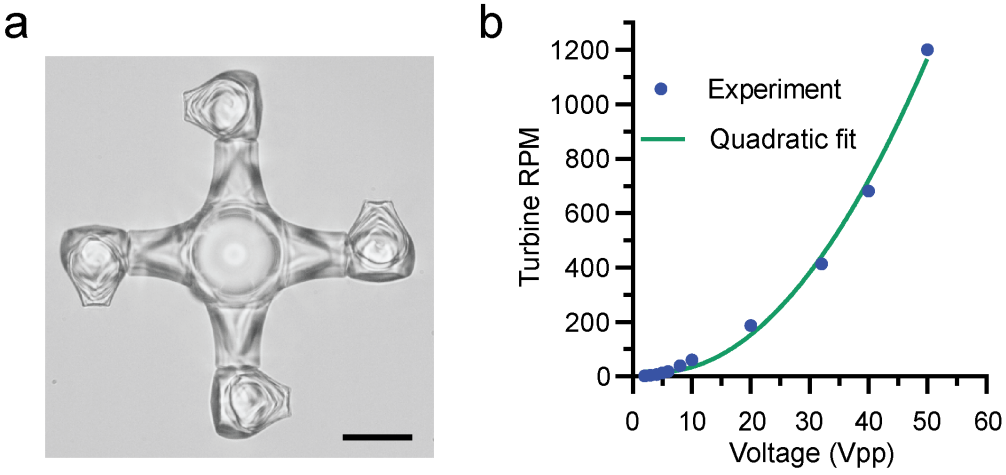

Figure 5.11 – a) Bright-field image of a µrotor propelled by four µthrusters. The device was printed *in situ* around an elastomer pillar. Scale bar: 50 µm. b) The angular velocity of the µrotor changes quadratically with the input voltage applied to the transducer.

We calculated the thrust generated by each engine using the 3D model of the µrotor. All engines were identical, which allowed us to divide the computational domain into quadrants. An extra symmetry plane perpendicular to the rotor axis was formed to further reduce the size of the domain and 1/8th of the structure was simulated. A single rotating reference frame was created around the rotor and angular velocity was set as an input parameter. This method provides an approximation for the steady-state flow field around the rotor in its reference frame without going through the complexity of modeling moving parts. The total pressure along with the viscous stresses acting on the structure was integrated to compute the total fluid force or drag for experimentally recorded angular velocities. Since the rotor was operated at steady state, it was possible to directly deduce thrust from drag (Figure 5.12b). According to the simulation results, each µthruster generates 9.15 nN at V_{PP} = 50 V (Figure 5.12b). These calculations give an order of magnitude estimate on the thrust generated upon acoustic excitation and guide future development of microscale turbomachinery.

Frequency selective actuation of µthrusters

One shortcoming of the presented prototype is the lack of directional control (i.e., the rotor rotates only in one direction). The response of the structures to acoustic waves depends on its architecture, thus, the distribution of forces can be controlled by engineering multiple µthrusters with varying wedge design. We engineered a µrotor that rotates in both clockwise (CW) and counterclockwise (CCW) by incorporating two types of µthruster that resonate at different frequencies (Figure 5.13a). They were arranged as couples to preserve the symmetry

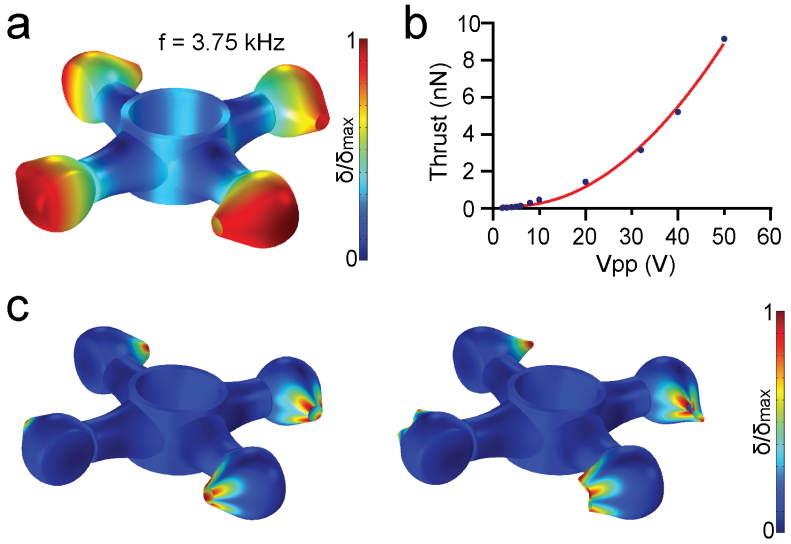

Figure 5.12 – a) Numerical simulation of the µrotor showing the eigenmode corresponding to the acoustic excitation frequency used in the experiments. b) he calculated thrust of a µthruster with respect to input voltage used in the experiments. c) A representative eigenmode of the 4-arm µrotor along driven by µthrusters at a higher resonance frequency. The deflection is localized at the tip of µthrusters resulting in less rotational speed, yet smooth rotation in a rotation compared to lower frequency resonance mode. Top panel shows color coding only while bottom panel shows color coding with exaggerated deformation.

of the rotor and minimize off axis motion. We performed a numerical modal analysis of the machine for frequencies up to 200 kHz and determined two frequencies, 5.19 and 25.77 kHz, at which µthrusters were selectively excited (Figure 5.13b).

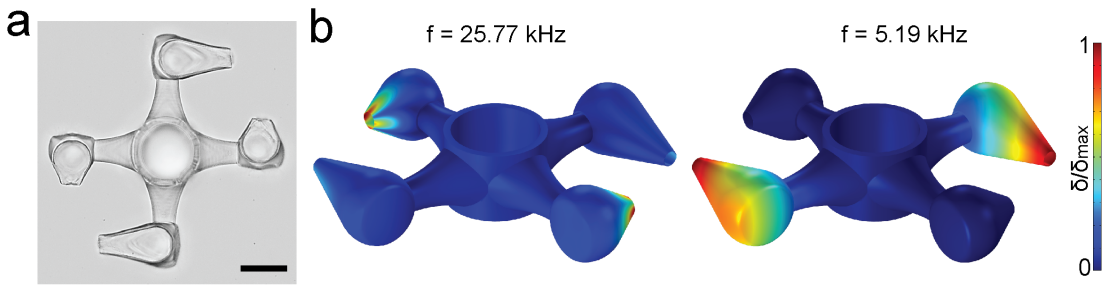

Figure 5.13 – Frequency selective actuation of µthrusters a) Bright-field image of a bidirectional µrotor driven by two different designs of µthruster. The symmetric arrangement ensures smooth rotation. Scale bar: 50 µm. b) Numerical simulations showing selective excitation of µthrusters at different resonance frequencies.

In the experiments, these modes manifested at slightly different frequencies (6.7 and 22.7

kHz), which could be explained by fabrication imperfections. The µrotor rotated 1.75 times faster at 6.7 kHz compared to the speed at 22.7 kHz for the same input power. Next, we explored the potential of sound waves in precise angular position control by modulating the input signal (Figure 5.14a). To simplify the dynamics of machinery, we reduced the number of arms and fabricated a mechanism that can serve as a rotary positioner or steering wheel. This configuration resembles the thrust vectoring devices engineered for steering rockets and satellites using reaction engines.

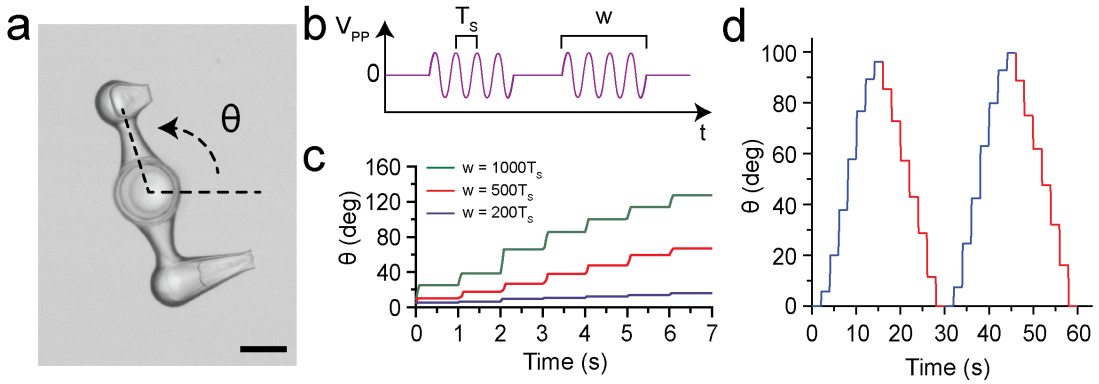

Figure 5.14 – Precise angular position control by modulating the input signal. a) Bright field image of a µrotor depicts angular displacement. Scale bar: 50 µm. b) The input signal consists of pulsed sine waves with period T_S and frequency f_S. The pulse width (w) was modulated while the amplitude and period of the pulse were kept constant. c) CCW rotation of the two-arm µrotor excited with pulses of varying w. d) Bidirectional rotation of the device with pulse-width modulation. CW rotation was performed at f_S = 4.6 kHz and with w = 1000 T_S while, for CCW rotation, the input signal was tuned to f_S = 23.8 kHz and w = 1200 T_S to generate identical motion in both directions.

Angular displacement was controlled in steps using a technique called pulse-width modulation (Figure 5.14b). Each pulse consisted of several cycles of a sine wave that were generated at the resonance frequency ($f_S = 1/T_S$) of the µthrusters (4.6 and 23.8 kHz). We fixed the period of the pulse (T_P) to T_P = 1 s and amplitude to V_{PP} = 40 V, and recorded the angular velocity of the positioner for varying pulse width (w) or duty cycle (Figure 5.14c). The same pulse generated slightly different angular displacement during the rotation. This variation can be attributed to the nonlinear propagation of acoustic waves in our experimental setup. Closed-loop feedback control of input voltage may deliver precise and repeatable motion. For the same pulse width, we recorded slightly different angular displacement in CW and CCW directions. To compensate for this variation, we selectively tuned the pulse width to 1000 T_S and 1200 T_S for 4.6 and 23.8 kHz, respectively. This adjustment led to the same average angular velocity in both directions of motion (Figure 5.14d). This demonstration shows that a separate calibration curve is required for each degree of freedom.

5.2.3 Soft robotic micromanipulation with compound machinery

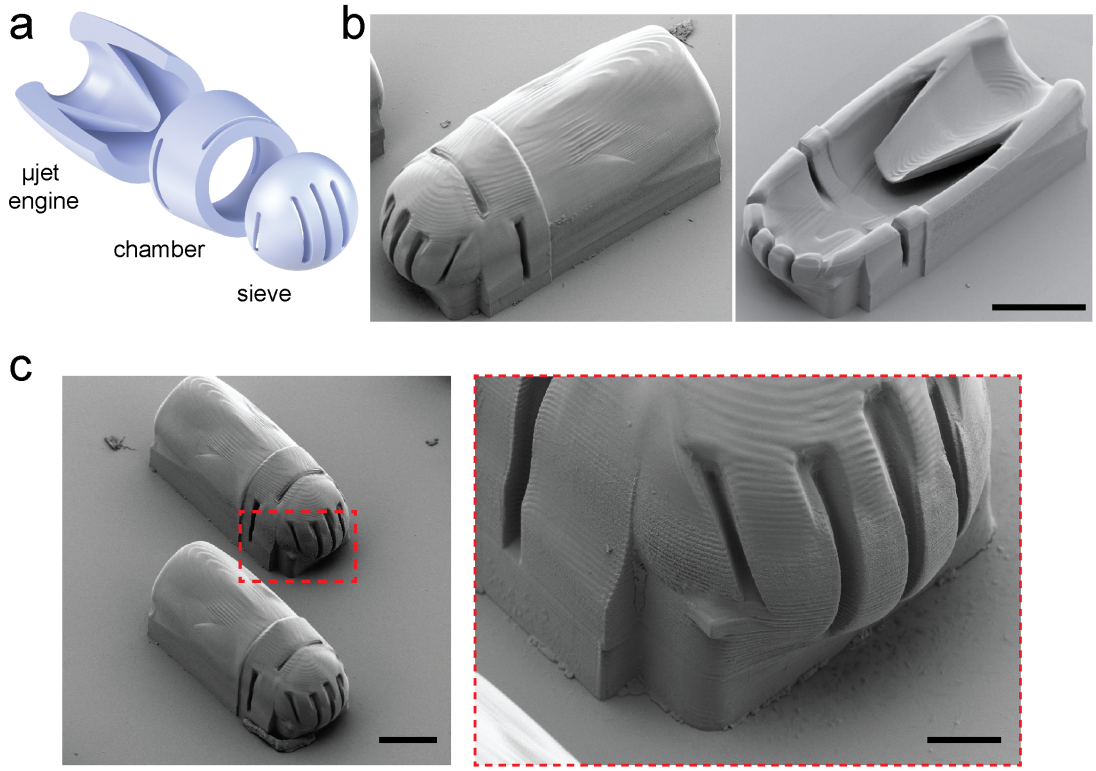

Figure 5.15 – Compound machinery for sample collection. a) Schematic illustration and b) electron microscopy images of a collection device comprised of a µjet engine, a chamber with slits to facilitate fluid flow, and a sieve for size-selective particle and cell encapsulation. b) Scanning electron microscopy images show two identical integrated devices fabricated next to each other (left) and close-view image of the sieve (right). Scale bars: b) 75 µm, c) 75 µm (left), 20 µm (right).

After building a repertoire of micromachines, we explored the potential for robotic micromanipulation of synthetic and biological samples. As a proof of concept, we engineered devices for the controlled collection of microparticles and mammalian cells. With these first demonstrations, we envision to discover design rules for the development of remotely powered and programmable microdevices that can perform in vivo diagnostic or therapeutic operations.We upgraded the µjet engine by incorporating a collection chamber and a sieve into the original design as shown in Figure 5.15a. The integrated device can circulate a suspension through the chamber to selectively collect target samples (Figure 5.15b). The sieve, together with the slits printed around the chamber, was designed to filter particles within the desired size range (Figure 5.15c).

We first tested the functionality of the machine using 10 µm polystyrene microparticles. Figure 5.16 shows snapshots from the collection procedure where the chamber was gradually filled with particles. The granular nature of the suspension allowed the fluid to flow through

the device until the chamber was completely jammed and there was almost no space left between the particles. The successful transport of particles from the inlet to the chamber depended on the dimension of the opening of the wedge, the acoustic power, and the size of the particles.

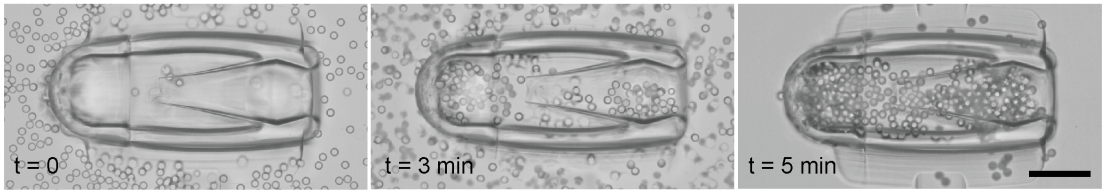

Figure 5.16 – Bead collection using the compound machine. a) Time-lapse microscopy images from a particle collection experiment showing: i) the initial condition where the microfluidic chamber was filled with particles and the chamber of the device is empty (t = 0), ii) an intermediary state where the chamber was gradually filled with particles due to the acoustic powering of the µjet engine at 117 kHz, and iii) the final state that showed the completely filled chamber after washing away the free particles. Scale bar: 75 µm.

Next, we tested the functionality of our device under physiologically relevant environmental conditions. We filled the microfluidic chamber with human embryonic kidney cells that were suspended in culture medium. Notably, wedge opening diameter smaller than 15 µm did not allow collection of cells even though cells should be able to fit into this constriction. We observed that few cells that could pass in the beginning of the experiment got immediately trapped in the steady streaming around the wedge and clogged the channel. On the other hand, when we increased the diameter of the opening above 40 µm, the pumping efficiency went down significantly because the effectiveness of the jet was gradually lost. Another interesting feature of acoustofluidic manipulation was that nearby cells attracted each other due to secondary acoustic radiation force or secondary Bjerknes force,[159]–[161] which facilitated mass transport in our experiments.

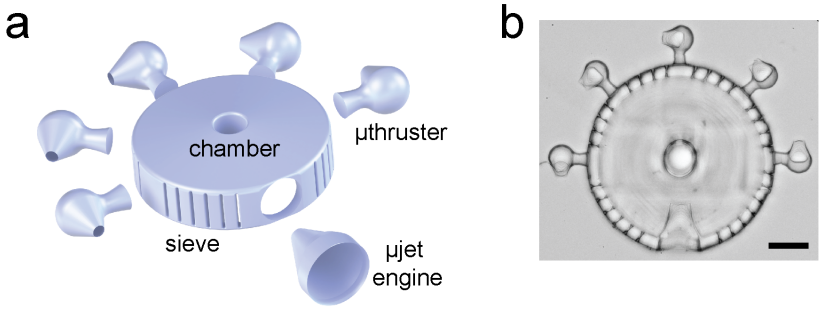

Figure 5.17 – Motorized collection device. a) Schematic illustration and b) bright-field image of a motorized collection device. Several µthrusters are located around the chamber for effective control over angular motion. Scale bar: 75 µm.

As a final demonstration, we combined local pumping with rotary motion to construct a multibody particle collection device with angular position control (Figure 5.17a). The engines in this modular device were chosen from the repertoire of machines shown in the previous sections. The compound machine was designed in a way that the μjet engine and μthrusters were excited at two different frequencies (Figure 5.17b). Upon acoustic excitation at 267.4 kHz, 10 μm polystyrene microparticles were started to be transported into the main chamber. At this relatively high frequency, we observed no streaming around the μthrusters and the device stayed stationary. After filling the chamber, we activated the μthrusters at 5.1 kHz, which led to the continuous rotation of the device as expected with no detectable pumping of particles. The device retained the entrapped particles inside the chamber during the washing away of the free particles (Figure 5.18a). This multifunctionalmodular device allowed on-demand collection and manipulation of particles at specified locations inside the microfluidic channel (Figure 5.18b). As a future extension, the device can be fully mobilized to enable both translational and rotational motion synchronized with particle collection. For precisely controlling the direction of motion, μthrusters with multiple resonance frequencies must be operated with appropriate control signals, as shown in Figure 5.12a and Figure 5.13b.

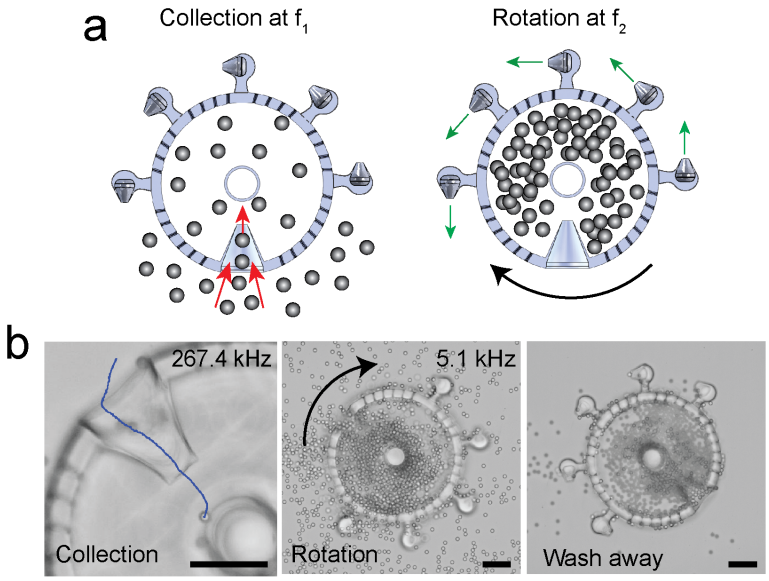

Figure 5.18 – Multibody particle collection device with angular position control. a) Illustration summarizing the working principles of the device. Addressable actuation of μjet engine and μthrusters enable multiple degrees of freedom control over the operation. b) Image sequence showing particle collection at 267.4 kHz, rotation of the filled device at 5.1 kHz, and the final state of the device after cleaning of the free particles. Scale bars: 75 μm.

5.2.4 Conclusion and discussion

Unlike alternatives based on electromagnetic, chemical or optical actuation, our powering scheme does not require the use of any specific material or medium. In the presented actuation paradigm, small amplitude structural oscillations of machine components at resonance generated large scale motion and mass transport. This strategy provides effective and efficient means for harnessing power from traveling acoustic waves, an important feature for *in vivo* applications. To further evaluate clinical potential, we verified the functionality of all the prototypes using medical grade immersion and contact ultrasound transducers (Figure 5.19). We chose hydrogels as the material for manufacturing because they have tunable Young's modulus (Pa to MPa) that is comparable to biological tissues. Furthermore, there are hydrogel formulations that are biocompatible, biodegradable, and amenable to functionalization for biochemical stimulation of target cells. These are other key properties for the intended in vivo applications. Notably, hydrogels can possess physical intelligence through stimuli-responsive behavior.[95] By tailoring the material composition of the resin, we can build autonomous microrobots that can reconfigure their shapes in response to changes in their microenvironment. This morphological transformation can be directly coupled to our acoustic powering paradigm based on sharp-edged structures, closing the loop for sensing-computation-actuation cycle, which is the basis of adaptive behavior and autonomy. Taken together, with the introduction of a proper injection or implantation technique, the presented machinery has the potential to become accessible for clinical applications.

There is no formal methodology for the design of monolithic compliant machines with multiple vibrating engines. With the incorporation of every new engine, the resonance modes of all the existing engines and the corresponding streaming profiles change. The integrated response of the machine articulates the importance of computational analysis. We have developed a modeling framework that can be used as a design tool for the development of more complex microrobots. Considering the small amplitude deformation, it is unlikely that fluid has a significant effect on the bending of the structures. As a result, our modeling assumption on one way coupling from the solid to the fluid seems reasonable. However, in our simulations, we completely ignored the propagation of sound waves in the media. These effects are expected to be more dominant inside biological tissues. We observed that with increasing frequency the velocity of the bulk streaming that appears around the casing reduces significantly. Thus, intuitively, operating devices at high frequencies will increase the precision of manipulation and enhance the validity of computational design efforts. In our future work, we will extend the model to incorporate the direct interactions between acoustic waves and surrounding media. Recent work withmacroscale mechanical metamaterials has shown that locally varying the shape or stiffness of the building blocks and exploiting interactions of transition fronts with topological defects lead to predictable and programmable nonlinear motion.[86], [162], [163]The development of acoustically powered multibody systems may lead to creation of mechanical logic and reconfigurable architecture toward the realization of more efficient and autonomous microrobotic devices.

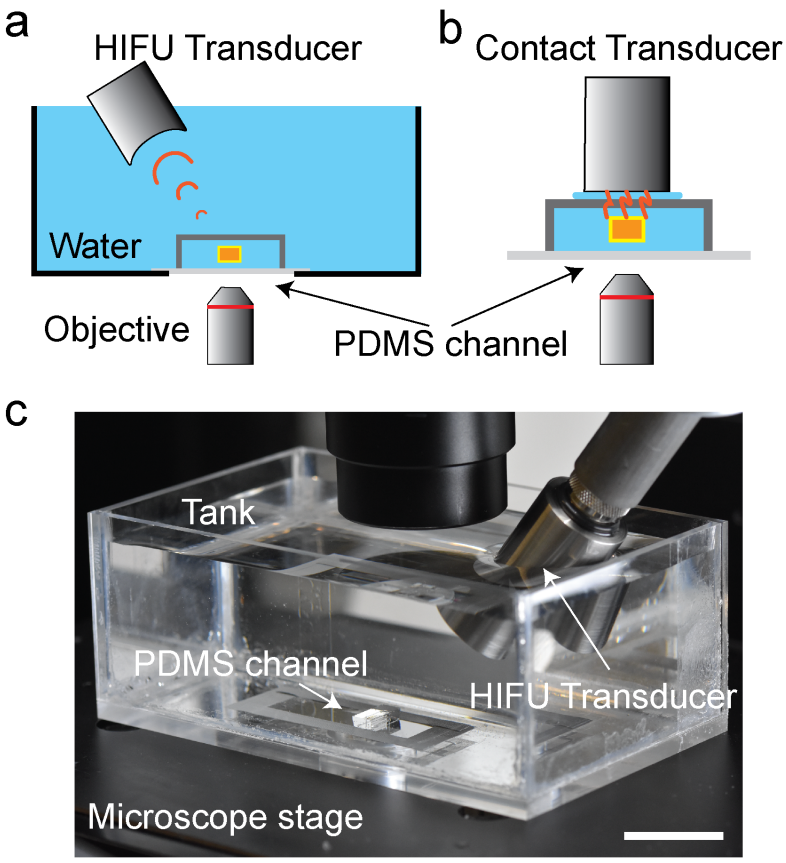

Figure 5.19 – Clinically relevant actuation. a) Water immersion high intensity focused ultrasound (HIFU) transducer is positioned above the microchannel where the µthrusters and µjet engines are 3D-printed *in situ*. b) Contact ultrasound transducer located above the microchannel with water as a coupling agent in between. c) A picture showing the water-filled tank, HIFU and microchannel placed on a microscope stage. Scale bar: 4 cm.

5.2.5 Experimental Section

Fabrication of Soft Robotic Microsystems

Hydrogel structures were fabricated using a 3D laser nanoprinting machine (Nanoscribe GmbH). A 63x oil immersion objective (63×/1.4 Oil DIC M27, Zeiss) was used for printing structures inside closed microfluidic channels from a solution of PEGDA (M_n = 250, Sigma) and pentaerythritol triacrylate with 3:1 ratio (v/v). A photosensitizer (4,4'-bis(diethylamino) benzophenone) and photoinitiator (Irgacure 369, Sigma) were added to at a final concentration of 1% and 5% w/v, respectively. 3D models of the structures were sketched using a computer-aided design (CAD) software (Solidworks 2018, Dessault Systèmes) and further processed via Describe (Nanoscribe GmbH) before importing them for printing. 3D models were sliced 0.25 µm vertically and 0.05 µm horizontally with a hatching angle of 45°. A scan speed of 0.3 m s^{-1} and laser power of 45 mW were set for all printing jobs. The unexposed hydrogel

solution was gently washed away with ethanol. Hydrogel structures with large surface area adhere strongly to untreated glass substrates. To avoid adhesion issues, mobile structures were printed in 3D forms that minimized contact with the substrate. In addition, printing parameters were chosen to adjust the first print layer slightly above the glass slide, which greatly reduced adhesion to the substrate. As a result, gentle agitation applied by the flow seamlessly released the structures. Devices were kept in ethanol for long-term storage.

Fabrication of Microfluidic Devices

Microchannels were fabricated using replica molding. Briefly, 5 µm positive photoresist (AZ9260, MicroChem) was spin coated on a 4-in. silicon wafer using automatic resist processing cluster (EVG150, EVG Group). Photolithography was performed using a mask aligner (MJB4, Süss) and the mold was prepared using reactive ion etching (AMS 200, Alcatel Adixen). The topography was mapped using a mechanical profilometer (Dektak XT, Bruker). The mold was silanized (trichloro(1H,1H,2H,2H-perfluorooctyl) silane, Sigma) under vacuum for 6 h. Poly(dimethylsiloxane) was prepared as a mixture (10:1, w/w) of elastomer and curing agent (Sylgard 184, Dow Corning) and poured on the mold in a petri dish. After degassing of the mixture in a vacuum chamber, the elastomer was cured at 65 °C for 4 h. After the inlets and outlets were formed using a 0.5 mm biopsy punch (Elveflow), the device was bonded to a glass coverslip right after functionalizing the surfaces of both substrates with oxygen plasma (PDC-32G, Harrick Plasma).

Experimental Platform

A piezo transducer (SMMOD15F120, Steminc INC.) was glued right next to the microfludic chamber using a 5 min epoxy (G14250, Devcon) as shown in Figure 5.20.

Solutions and suspensions were injected into the microfluidic device using a computer controlled syringe pump (neMESYS 290N, Cetoni). Before each experiment, channels were filled with ethanol to reduce the surface tension and avoid air bubble formation. The transducer was controlled by a function generator (AFG-2225, Gw Instek) connected to a high voltage amplifier (HVA200, ThorLabs). Soft robotic microsystems were also excited using water immersion (GS200-D19-P50, The Ultran Group) and contact transducers (GC100-D19, The Ultran Group) to demonstrate acoustic wave transmission in different configurations.

Microscopy and Imaging

Acquisition of images and videos was performed using a high speed camera (VEO640L, Phantom) connected to an inverted microscope (Ti2, Nikon) with a 20X objective (Nikon). Videos were captured using the camera‘s commercially available software (phantom camera control, Phantom) and analyzed using Fiji (National Institute of Health). Data were plotted using Prism 8 (GrapPad Software Inc.). Streamlines were visualized using 1 µm fluorescent polystyrene par-

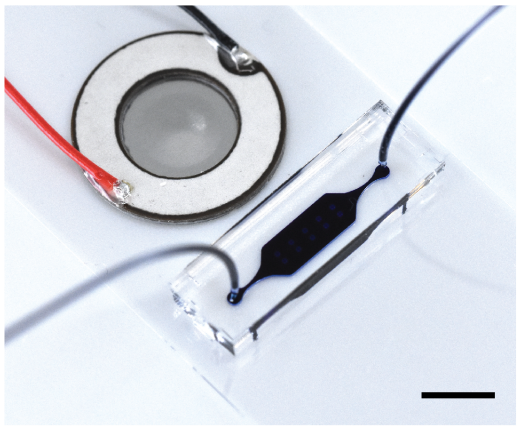

Figure 5.20 – A picture of the experimental platform. µthrusters and µjet engines are fabricated inside an enclosed microchannel. Then, they are actuated via piezotransducer placed adjacent to the microchannel. Scale bar: 5 mm.

ticles (Cat # 17154-10, Polysciences). High-magnification images were taken using a scanning electron microscope (LEO 1550, Zeiss). Prior to imaging, devices were fixed using hexamethyldisilazane (Sigma) to preserve their structure and coated with a thin conductive layer of gold (10 nm) using sputtering (DP650, Alliance-Concept).

Numerical Simulation

CAD models generated in Solidworks and CatiaV5 were imported to COMSOL Multiphysics 5.4 for mesh generation and computational analysis. 2D simulations were performed with triangular elements while 3D simulations were performed with tetrahedral elements to ease the meshing process. An adaptive mesh scheme was followed. For example, 90000 tetrahedral elements were used for the mesh of engines (minimum quality of 0.3 and average quality of 0.9) that are on the order of 100 µm in size with a surrounding fluid domain that was at least four times larger than the volume of the structure. The area around the tip was refined with 0.05 µm mesh elements. The selected time step was 0.02 µs for the simulations. These values were chosen in order to ensure that the mesh was converged and enough data points were saved to accurately capture the mechanics of the simulated models. The eigenfrequency analysis module was used to extract the eigenmodes and eigenfrequencies of 3D structures. The values of the density of the hydrogel, Young's modulus of the hydrogel, and the viscosity of the fluid are given by ρ = 1000 kg m^{-3}, E = 0.5 MPa, and μ = 0.001 Pa s, respectively. The presence of the surrounding liquid was incorporated as added mass on the structure. The normalized eigenmodes were used as inputs for the CFD simulation. A coefficient was tuned manually to define the amplitude of the oscillations. The resulting eigenmode shape was used as a moving boundary in the CFD simulation and it was assumed that the fluid-structure interactions were only in one way (i.e., from solid to fluid). The Laminar module combined

with the moving mesh module (Arbitrary Lagrangian-Eulerian) was used to obtain the flow patterns around the oscillating structures. The viscous stresses and the total pressure were integrated to extract the total stresses on the structure.

Cell Culture

HEK 293T/17 (American Type Culture Collection) were cultured in Dulbecco's modified Eagle medium GlutaMAX (LifeTechnologies, Carlsbad, CA, USA) supplemented with 10% fetal bovine serum (LifeTechnologies) and 1% penicillin-streptomycin (LifeTechnologies). Cells were passaged every 2–3 d using trypsin 0.25% (ethylenediaminetetraacetic acid, LifeTechnologies) and not kept longer than 20 passages. All experiments were done with cells that tested negative for mycoplasma.

Statistical Analysis

Results are presented as mean ± standard deviation. Statistical analysis was performed using Prism 8 (Graphpad). Data were processed coming from at least three different trials per device and the number of devices tested (n) is at least 4 ($n > 3$) for each condition.

6 Compound micromachines powered by acoustic streaming

3D printing is very convenient for building complex machines. However, printing materials that are very soft is challenging due to stress accumulation and bending during layer by layer polymerization. Printing support layers may address this issue but this feature has not been implemented in two photon polymerization yet. We aim to maximize trust by using soft sharp edge structures that show large deformation at the tip. To this end, a well-established technique called projection lithography is explored.

This chapter presents the design, fabrication, and operation of compound micromachines powered by acoustic streaming. The machine components were directly incorporated around pillars serving as shafts without further assembly steps using a single-step *in situ* polymerization process controlled by a programmable projector. Two strategies were presented for harvesting acoustic energy using sharp-edged structures. The first method is based on on-board pumping of fluids and the second method involves engineering of rotors. The implementation of these strategies resulted in the construction of microscale turbines and engines that can be coupled to gear trains for adaptable transmission of mechanical power. We provide a number of further improvements that may together lead to development of compact yet powerful robotic manipulation systems inside microfluidic devices.

This chapter is an adapted version of the following publication[164]:

Kaynak, M., F. Ayhan and M. S. Sakar, "*Compound micromachines powered by acoustic streaming*", 2019 International Conference on Robotics and Automation (ICRA), Montreal, QC, Canada, 2019, pp. 225-230.

Author contribution

Kaynak, M., and Sakar, M. S. designed the experiments, **Kaynak, M.**, Ayhan, F. performed the experiments and analyzed the data, **Kaynak, M.**, and Sakar, M. S. wrote the manuscript, Sakar, M. S. supervised the research.

6.1 Introduction

Microfluidic laboratory-on-a-chip technology promises to enable automated execution of macroscale, bench-top experimentalprotocols in low-cost, miniaturized devices [165], [166]. Precise manipulation of small volumes of fluids and biological samples along with the ability to perform quantitative analysis has already started to revolutionize clinical diagnostics and pharmaceutical research [132]. While sensing and visualization techniques have been rapidly advancing [167], actuated structures are largely limited to the use of conventional pneumatic valves [168]. Previous works demonstrated the feasibility of operating remotely controlled robotic microtools inside microfluidic chips for micromanipulation [34], [169]–[176]. These untethered simple machines provide spatial control over mass transport, yet the design and fabrication methodology is not appropriate for the construction of modular and highly customizable, complex integrated microsystems. A simple and cost-effective method to overcome viscous forces and drive microscopic machinery inside microfluidic channels is the use of sound waves generated by piezoelectric transducers [45], [98], [156], [177]. Microbubbles whose surfaces oscillate when forced with acoustic waves generate powerful flows that can be harnessed for microscale propulsion [40], [41]. While bubble cavitation is the oldest and most extensively studied method for utilizing acoustic power in biomanipulation [178], there are a number of limitations for precision engineering applications. Encapsulation of bubbles exclusively inside engraved cavities on driver components is a challenging procedure. Furthermore, there is no reliable method for retaining the size and shape of the bubbles during long-term continuous excitation inside biological fluids at physiological temperatures. Solid bodies vibrating in fluids also generate steady streaming if they have sharp features [42], [157], [179], providing a more robust and scalable solution for acoustofluidic actuation. Building devices decorated with sharp-edged structures to drive multi-body robotic microsystems is the focus of this work.

We present two distinct strategies for powering compound micromachines (Figure 6.1). In the first mechanism, the walls of the microchannel are decorated with actuated structures to generate pressure difference and drive a turbine located downstream of the pumping area (Figure 6.1a). The second mechanism is driven by a rotor generating acoustic streaming with sharp features attached to its body (Figure 6.1b). Microscale posts fabricated inside the channels serve as shafts for rotating active and passive elements. Maskless optofluidic photopolymerization process enables the manufacturing of custom shaped functional microparts, which we use to create compound micromachines without requiring further assembly. The blueprint for the chassis and machine components are highly re-configurable, which allows rapid design and prototyping of a variety of different systems. We provide guidelines for constructing more sophisticated systems with additional mechanisms such as a clutch.

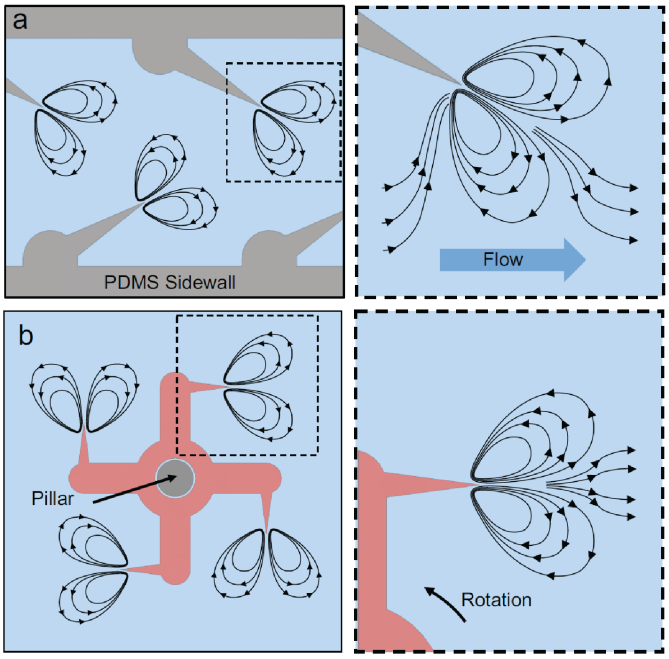

Figure 6.1 – Schematic depiction of working principles for machines powered by acoustic streaming. Upon application of acoustic waves, sharp-edged structures oscillate and generate counter rotating vortices. These vortices can be utilized to drive machinery by generating a) fluid flow inside a watermill system and b) rotation of engines around a shaft (not to the scale).

6.2 Results

Sharp edges generate oscillations at their tips, resulting in a pair of counter rotating vortices. There are pushing and pulling forces generated at each oscillation cycle. The displacement of fluid during pushing is higher than the pulling phase due to viscous attenuation, resulting in pressure fluctuations and formation of a localized jet. We utilized this phenomena in two different ways to power microscale autonomous devices.

6.2.1 Microturbines driven by acoustic pumping

Figure 6.2a shows an image of the device, revealing the overall architecture of the waterwheel mechanism. The fluid flow generated by the sharp-edged structures on the walls of the microchannel is channeled through a closed hydraulics network. The structures were placed bilaterally throughout the pumping area (Figure 6.2b) with a spacing and angle optimized for pumping efficiency [179]. The structures were expected to provide maximum acoustic streaming at the resonant frequency of the transducer (4.6 ± 0.6 kHz). However, at this frequency, geometrical deviations from a straight profile such as curved channels or structural impurities generate non-linear effects that interfere with the flow. We performed a frequency sweep test between 1 and 100 kHz and measured the corresponding flow rate. The best performance was recorded at 30.9 ± 1 kHz and, thus, this frequency was chosen as the driving frequency.

We injected polystyrene microparticles with a diameter of 1 micron into the microchannel to visualize the fluid flow. Vortices are expected to form symmetrically when the tip of the sharp edge is normal to the side wall. By tilting the structures by 30°, we modulated the distribution of vortices and, as a result, created net flow that was observable through the streamlines (Figure 6.2b).

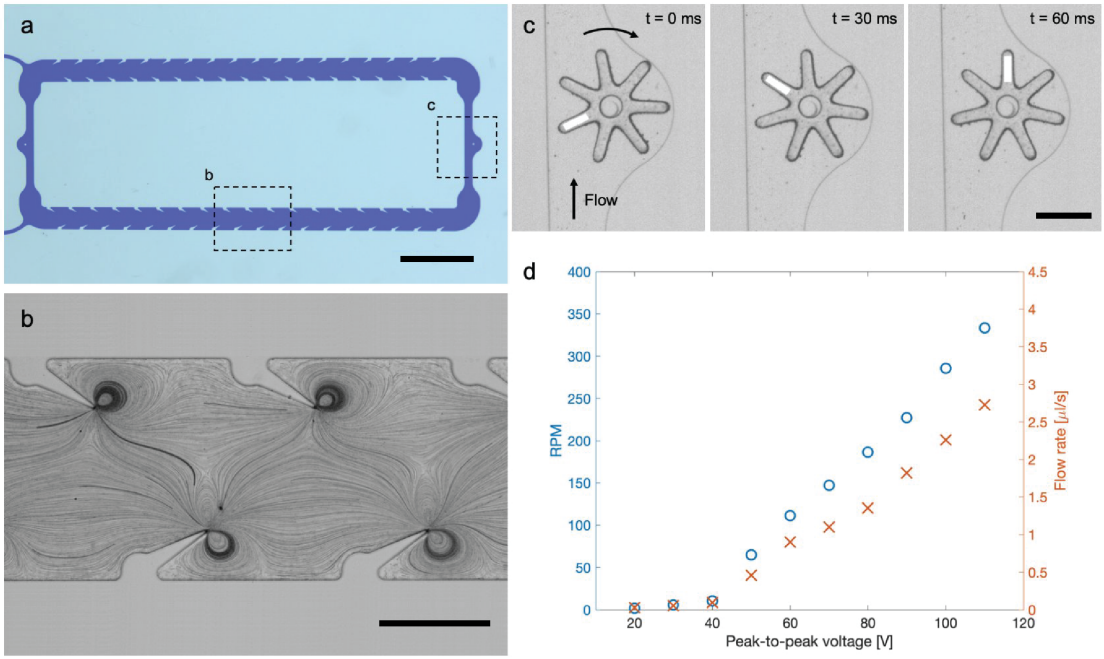

Figure 6.2 – The design and operation of acoustically powered microturbines. a) A representative image of the system designed to pump fluids along the closed hydraulic network and rotate the turbine. Scale bar: 2 mm.b) The fluid flow generated in the pumping area, visualized by particle tracking. Scale bar: 300 µm. c) The sequence of images from a rotating turbine. The white bars indicate specific teeth locations. Arrows show direction of rotation and flow. Scale bar: 200 µm. d) A representative plot of flow rate and turbine revolution rate as a function of the input voltage.

The turbine was formed around the pillar that was engineered inside a circular confinement downstream the pumping area (Figure 6.2c). The primary consideration here is that at low Reynolds number viscous fluids obey the no-slip condition. The thickness of the blades of the turbine was optimized for effective transmission of hydrodynamic forces. Low thickness led to bending of the blades while high thickness generated large viscous drag. The angular speed of the turbine was controlled by tuning the peak-to-peak voltage (V_{PP}) that was applied to the piezoelectric transducer. As a rule of thumb, the higher the input voltage the larger the flow rate due to increase in vibration amplitude. The hydrodynamic forces started to exceed the drag forces and reached enough power to rotate the turbine at 20 V_{PP} (Figure 6.2d). The angular speed increased with applied voltage for all tested values. The rotation completely halted within ≈ 2 ms after turning off the input source due to the characteristics of low Reynolds

number flow.

6.2.2 Computational analysis of acoustic streaming

We performed numerical simulations of the pump mechanism using COMSOL Multiphysics software. We first identified the eigenfrequencies of the structures by running coupled acoustic-structure finite element simulations. The oscillating structures are defined as linear elastic materials due to the mechanical properties of the elastomer. After investigating the vibration modes corresponding to different resonant frequencies, we concluded that the best pumping performance is expected at 6.5 kHz and 27 kHz. The eigenmodes that are driving the vibrations at 27 kHz are shown in Figure 6.3a. The slight increase in the resonance frequency compared to empirical results can be due to the damping in the system and the losses at the interfaces, which were neglected in the computational model. We also assumed that the propagation of the acoustic wave in the fluid does not influence the excitation of the structures because the wavelength of sound in fluid is significantly larger than the characteristic length of the oscillating structures.

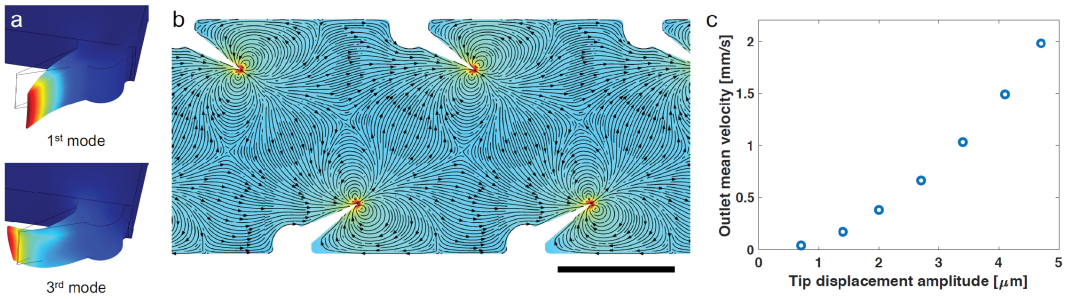

Figure 6.3 – Simulation results of the sharp-edge structures. a) The dominant vibration modes of the structures at 27 kHz. Color represents relative amplitude. b) The streamlines generated inside the pumping area during excitation at 27 kHz. The mean velocity is computed on the fluid domain over 10 oscillation cycles. Scale bar: 300 µm. c) The mean velocity along the long axis of the channel at the outlet that is calculated at different displacement amplitudes.

In the second part, we developed a computational fluid dynamics model to study the flow generated inside the channel using a one-way fluid-structure coupling scheme. That is to say, the actuated structures influence the surrounding fluid but the fluid does not effect the motion of the structure. We applied periodic displacements to the sharp-edged structures according to the excited eigenmodes. Figure 6.3b shows the streamlines generated by the oscillating structures at 27 kHz where we computed the mean velocity over 10 oscillation cycles. We assumed that all structures were actuated with the same acoustic field, which led to a symmetrical flow field inside the channel. We observed asymmetry in the experimentally recorded flow field (Figure 6.2b) due to the damping of pressure waves during power transmission. We modified the amplitude of the oscillations to derive a relationship between the flow rate in

the channel and the input power. The net flow rate increases with the increasing amplitude after exceeding a certain threshold and the trend seems to be linear (Figure 6.3c). The mean velocity was measured as 0.8 mm/s which corresponds to a numerical oscillation amplitude of 3 μm and we verified that the tip movement during experiments corroborates with this prediction. Interestingly, simulations also showed that the streamlines do not depend on the amplitude of the oscillations for a given frequency.The computational framework can be used as a design tool to investigate the influence of device parameters such as the distribution and geometry of structures, channel dimensions, and material properties.

6.2.3 Microengines powered by acoustic rotors

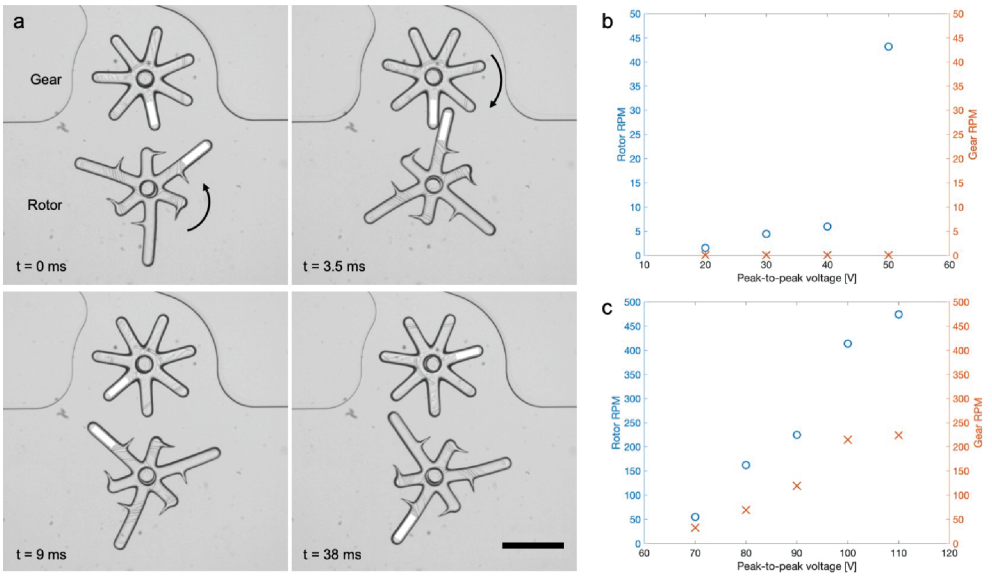

Figure 6.4 – The design and operation of acoustically powered microengines. a) An image series of a rotating rotor and gear pair. While the rotor continuously moves, the gear display intermittent rotation due to the mismatch between teeth number. The white bars indicate specific teeth locations and the arrows show the direction of motion. Representative plot of the revolution rate for the rotor and the gear b) at low and c) high input voltages. Scale bar: 400 μm in a).

An alternative paradigm for driving microsystems is having an on-board mechanism to directly harvest acoustofluidic power (Figure 6.4). The pointy extensions fabricated on the rotor arms generated coordinated acoustic streaming, which induced torque on the rotor. Rotors with multiple arms, all equipped with sharp edges, were expected to generate higher angular speed. On one side, we would like to move the sharp edges as far from the tip of the arm as possible to protect the rest of the machinery from the generated fluid flow. On the other side, confinement of sharp edges between the arms significantly impedes the steady flow. Therefore, we engineered long and short arms, to address both limitations. Together with the gear, the

rotor formed an acoustically controlled engine. While long arms were interacting with the gear to transmit power, there was ample space left around the sharp edges for maximizing torque. The width of the arms also played an important role in the performance. We designed 500 µm x 100 µm arms because these dimensions resulted in maximum speed.

The speed of rotors increased quadratically with input voltage. This relation could be explained by the power relation of the transducer. Two different regimes were observed during amplitude modulation. At low voltage, the power transmitted by the rotor was not sufficient to rotate the gear. The gear started to rotate at 60 V_{PP} and its speed monotonically increased with input voltage. The gears were designed for optimal coupling with the rotor. The ratio between the angular speed of the rotor and the gear was given by 1:2, which is close to the ratio of the number of arms (3:7). The small discrepancy can be explained by imperfect coupling between the arms during rotation and structural defects on the parts. The existence of a chamber around the gear serves the same purpose as the chamber around the turbine, minimization of secondary flows. Although these structures did not have sharp features, they could still generate vortices around the tip of the arms. The walls surrounding the structures prevented completion of the formation of streamlines.

6.2.4 Construction of transmission

The speed ratio and the mechanical advantage of the systems can be systematically controlled by the incorporation of multiple gears (Figure 6.5). We tested whether we could add another gear without significantly reducing the power output of the watermill system (Figure 6.5a). The engaged turbine-gear pair had consistently lower angular speed than the single turbine as expected. Likewise, incorporating another gear to form a gear train into the microengine resulted in reduction in output torque (Figure 6.5b). The gears were rotating synchronously and leak flows did not have a significant effect on angular speed. We also engineered gears with different number of teeth. The measured value of the speed ratio for the pair of meshing gears were the same as the ratio of the number of teeth on each gear for all input voltage values, as expected.

6.2.5 Conclusion and discussion

The parts for building a transmission is not limited to the use of gears. The power output of the systems can be modulated by disengaging the turbine or the rotor from the transmission using a clutch. The presented fabrication methodology is compatible with stimuli responsive materials such as poly(N-isopropylacrylamide) pNIPAM. The swelling degree of pNIPAM depends on the temperature, which can be remotely modulated by light with the incorporation ofmagnetic or gold nanoparticles [13], [84]. The reduction in size can be utilized to reversibly

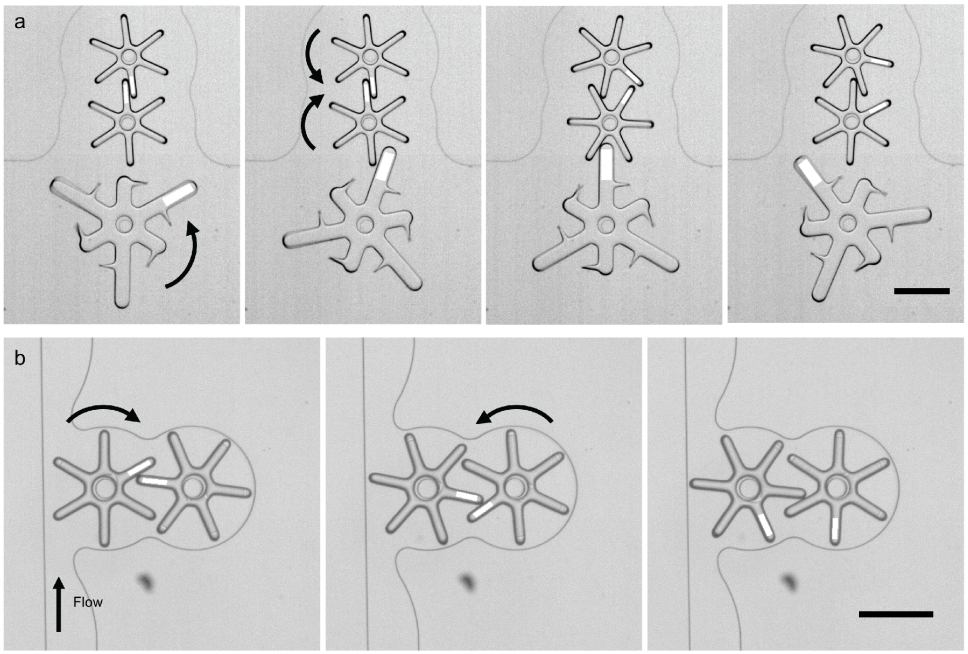

Figure 6.5 – The design and operation of gear trains. An image series demonstrating torque transmission in the a) watermill system and b) microengine. The white bars indicate specific teeth locations and arrows denote the direction of rotation. Scale bars: 400 μm and 300 μm in a) and b), respectively.

disconnect the driving part from the rest of the mechanism. Another upgrade would be to engineer a rack and pinion type mechanism to convert rotational motion into linear motion. The rack can be photopolymerized directly inside a microchannel next to the rotary engine in order to constrict the translational motion to a line.

We do not currently have control over the direction of rotation of neither the turbines nor the engines because sharp-edged structures generate unidirectional flow. Optical modulation of the shape of the structures may address this issue through the modulation of the alignment of sharp edges. By re-aligning the direction the tips, the streamlines may be dynamically moved. Alternatively, multiple sharp features with varying shapes or mechanical properties can be engineered on the same body to selectively excite acoustic streaming at different locations with the aid of frequency modulation. A similar approach has been recently employed to selectively actuate microbubbles that have unique dimensions [20]. This strategy may also lead to coordinated operation of multiple rotors on the same device.

In addition to providing control over power transmission, gear trains can also serve for another important purpose. The sharp edges generate secondary flows that are strong enough to dominate the motion of the machinery. However, there are primary flows generated by the propagating acoustic waves in the medium and, especially at high voltages, these flows may interfere with the intended operation inside the microfluidic device. The transmission may

allow complete decoupling of the end-effector from the driving mechanism and provide a flow free arena for the manipulation tasks. Furthermore, with the incorporation of clutch mechanisms, multiple different tasks may be completed by the same driving mechanism.

6.3 Experimental Section

6.3.1 Development of the micromachinery

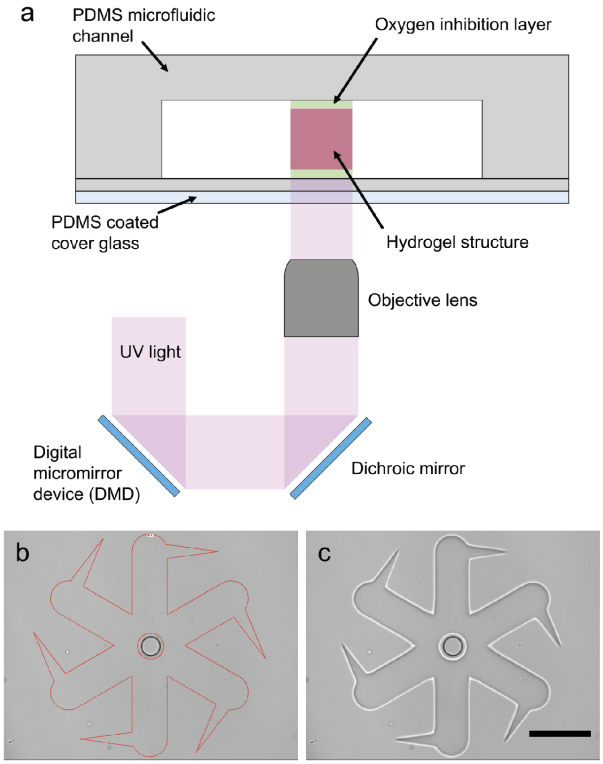

Figure 6.6 – Fabrication of hydrogel micromachines using digital maskless photolithography inside microchannels. a) Schematic illustration of the fabrication process. UV light is patterned and focused by a programmable microscope system according to the CAD drawings. Oxygen inhibition layer permits mobilization of structures. b) The light pattern projected on the screen and c) the microstructure polymerized at the end of the exposure process. Scale bar: 250 µm.

The systematic assembly of microfabricated parts and integration of assembled mechanisms with microfluidic devices are extremely complex tasks. *In situ* polymerization of photocurable polymers directly inside closed chambers is a promising alternative for rapid prototyping [180]. Hydrogels are particularly interesting materials for building machinery due to their tunable mechanical properties and stimuli-responsive behavior [28]. Figure Figure 6.6a illustrates the fabrication of hydrogel components around existing polydimethylsiloxane (PDMS) pillars

inside microfluidic channels. Microfluidic devices were fabricated using replica molding. In this work, channel height was set to be 100 µm. Sharp features required for the development of the pumping regions demand for high-resolution photolithography. We wrote the molds on chrome masks using a laser writer (VPG 200, Heidelberg) with 600 nm resolution to address this requirement. After development, the molds were coated with Trichloro(1H,1H,2H,2H-perfluorooctyl) to facilitate the removal of the PDMS devices.

PDMS is a gas permeable material and an oxygen layer (on the order of 1 µm) forms on the surface of the devices [181] during plasma treatment. This layer inhibits polymerization close to walls, which is instrumental for constructing free-floating machinery that are not attached or physically interacting with the boundaries. The glass slide, on which the microfluidic device and the piezoelectric transducer were attached, was coated with a thin layer of PDMS to utilize this lubrication strategy. As a further precaution, components were fabricated with bores slightly larger than the pillars. This approach ensures the free rotation of microcomponents around the shaft at all times. An image of the entire microfluidic device is shown in Figure 6.7. We used a low pressure syringe pump (neMESYS 290N, CETONI) to introduce the photocurable prepolymer solution (50% (v/v) polyethylene glycol diacrylate (PEGDA) 700, 30% (v/v) PEGDA 250, 20% (v/v) photoinitiator 2-Hydroxy-2-methylpropiophenone (Darocur 1173). All reagents were bought from Sigma Aldrich and used according to the manufacturer's instructions. Polymerization pattern during flow lithography was controlled by a programmable digital micromirror device (MM-8201-801, Andor). The projected UV light was focused onto the bottom layer of microchannels through a 10x objective lens (Plan Flour 10X/0.3 DIC L/N1, infinity/0.17 WD 16.0, Nikon). The intensity of UV light on the sample (80 mW/cm2) was measured using an optical power meter (PM400, Thorlabs).

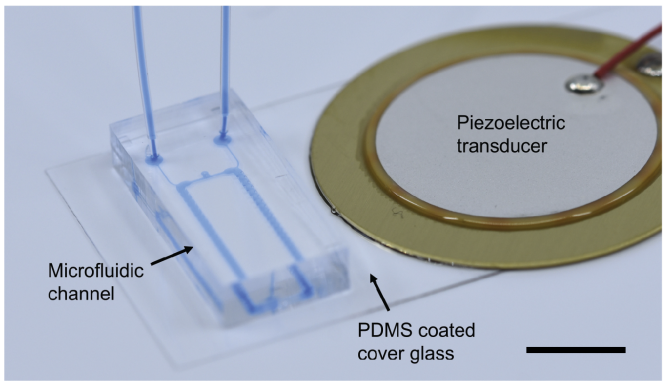

Figure 6.7 – Image of the integrated device consisting of the microfluidic channels and the piezoelectric transducer, all bonded to a glass slide. The acoustic waves are transmitted to the microfabricated machinery through the glass substrate. Scale bar: 10 mm.

6.3.2 Acoustic control system

The sinusoidal control signals were generated by a programmable function generator (AF-2225, GW Instek), which were amplified by a power amplifier (TOE 7610, TEOLLNER) before reaching the piezoelectric transducer (81-7BB-27-4LO, Murata Electronics). The transducer was bonded onto the glass slide using 5-minute epoxy (G14250, Devcon). The transducer was located in the center of the glass slide to enhance vibrations during operations on the microscope stage. The frequency and amplitude of input voltage were monitored using an oscilloscope (TBS 1032B, Textronix) during experiments. Experiments were performed with an inverted fluorescence microscope (Ti2, Nikon) and videos were recorded using a high-speed camera (VEO640L, Phantom).

7 Conclusion and Future Outlook

7.1 Conclusion

This thesis constitutes a step forward in the development of microscopic machines and devices. Among many others in the field, we followed the following philosophy: It is not feasible to miniaturize electrical actuators and batteries to the microscale and package them on the same microscopic device. Therefore, mechanical powering and programming techniques must be pursued. To this end, we focused on compliant structures and mechanisms for various reasons. First, they are made of biocompatible polymers and the presented manufacturing techniques are compatible with many other biopolymers. Second, at microscale, tissues are quite sensitive to mechanical loading. Compliant mechanisms minimize the damage, as exemplified by the work presented in **Chapter 3**. Third, rigid mechanisms that are made of joints and gears encounter significant problems upon miniaturization, due to the increased importance of surface effects. Fourth, compliant mechanisms can be engineered to serve as digital logic through incorporation of bistable mechanisms, a feature extensively explored in **Chapter 4**. Lastly, rationally designed compliant mechanisms are capable of converting pressure waves into mechanical work via acoustic streaming. This property served as the foundation for the devices presented in **Chapters 5** and **6**.

In **Chapter 3**, I introduced an optically transparent microscopic implant and associated implantation tools. This toolkit was used to image neural activity within living *Drosophila melanogaster*. The use of microengineered tools in fundamental neuroscience is not new. However, due to the small size of fruit flies, the technology was not applied in this context. Fruit flies are special in the sense that they can be genetically modified. This way, a number of human diseases can be modeled on an animal that rapidly breeds. The operations that we perform are pain free and do not require ethical approval. Taken together, flies are ideal for exploring a number of questions related to the workings and pathology of the nervous system. The technology is not limited to the thorax and ventral nervous system, other parts of the body could also be made visible for two-photon imaging. The implantation technique would work as along as the implants are within the same size range.

Once establishing the potential for in vivo studies, the thesis progresses to more advanced technologies that involve actuated mechanisms. Microbubbles are very efficient in transducing mechanical work from pressure waves in physiological fluids due to the large mechanical impedance mismatch between water and air. Furthermore, they are ideally suited for minimally invasive operations inside the body as exemplified by recent publications [38]. We based our actuation paradigm in **Chapter 4** on air bubbles encapsulated inside cavities, and systematically studied the forces generated by bubbles interacting with each other and the surrounding fluid. To this end, we harnessed the amazing capabilities of direct laser writing. Ultraflexible microstructures are printed in complex forms to hold bubbles, precisely control the spatial and temporal dynamics of their vibrations, and the resultant operation of the compliant mechanisms. Experimentally validated computational models informed the multiphysics behind the observed nonlinear phenomena including fluid-structure and wave-matter interactions. Empowered by this fundamental understanding, we built a variety of prototypes where the deformation and motion are programmed by the ultrasound signal. In addition, we harnessed bistable mechanisms to instantiate digital logic in purely mechanical systems. This new design and actuation paradigm push microrobotic technology into the next level by enabling fully autonomous operation of a team of micromachines. The devices can be fabricated from any material as bubble-based actuation is completely decoupled from the material properties of the solid structure. The presented technological breakthrough will soon allow the use of cell-size medical devices in vivo.

Bubbles have limited lifetime of a few hours. Therefore, they may not be suitable for devices that are expected to operate over a long time period. To address this issue, we turned to structural design in **Chapter 5** and **Chapter 6**. Sharp structures vibrate at large amplitudes and generate relatively strong streaming upon acoustic excitation. We patterned such structures over monolithically printed machines to control flow and body motion. One of the most interesting machines that is presented in those chapters is a microscopic pump that has no moving parts. The pumping is solely based on the vibration of structures. Not having moving parts makes the machine robust and very compact. Another important contribution of this part of the thesis is the operation of multiple pumps on the same device. This is possible thanks to the frequency selective excitation of vibrations using the concept of resonance. As the machines are printed, we could easily add filters and other parts that are commonly used for particle and cell manipulation.

7.2 Future outlook

7.2.1 Non-actuated implantable devices

The ventral nervous system of the fruit flies is functionally equivalent to vertebrate spinal cord. Our technology will reduce the number of experiment on vertebrates, which is compliant with the principle of 3R: replace, reduce, and refine. There is still room for improvement. The survival rate of implanted animals is 65% over a month while 85% of control groups could

survive. To increase the survival rate and reduce implantation time, human related mistakes should be eliminated. To this end, a robotic manipulation system must be built. We can envision automated laser cutting of the cuticle, subsequent insertion of the implant, and finally sealing of the hole with the transparent window. We are already using non-motorized manipulators. Motion planning based on visual feedback will require some effort as soft tissue manipulation is not trivial.

The transparent windows are numbered. With a proper imaging system, the animals can be tracked in their natural environment throughout their lifetime. Neurological responses within the social context can be studied with such a platform.

7.2.2 Acoustically actuated micromachines

An autonomous robot perceives its environment, makes decisions based on acquired information and programmed routines, and then actuates a movement or performs a manipulation task within that environment. The idea of microrobotics is primarily based on teleoperated mobile micromachines equipped with manipulation capabilities such as actuated grippers and drug-loaded reservoirs. A step toward complete autonomy is the development of on-board control systems that directly transduce environmental stimuli such as heat and pressure into actuation, without going through the perception and computation cycles. Following the analogy of the central nervous system for the architecture of conventional autonomous robots, the next-generation microrobots are expected to possess reflexes that would allow them to autonomously navigate inside structured microenvironments and perform targeted and triggered operations. Ultrasound is particularly appealing for the creation of autonomous microrobots because the bulk travelling acoustic wave does not necessarily apply force or torque to the machine. Taking advantage of this "power but not control" scheme, we explored the use of nonlinear mechanical mechanisms to instantiate automation. While proof-of-concept demonstrations presented in **Chapter 4** are promising, there is still a long way to go before we can present a fully autonomous machine that can find its way to a target location or perform programmed operation at the target location. A very promising direction is harnessing fluid-structure interactions as these interactions may either change the shape of the machine, which may determine its heading, or influence the operation of on-board acoustic microactuators, which will change the distribution of forces.

The microfluidic modules that are presented in **Chapter 5** constitute the foundation for the development of fully programmable implantable drug delivery devices. With the incorporation of multiple pumps and compartments, we can envision on-board mixing, synthesis, and analysis towards diagnostic and therapeutic functions. Cells can be collected or released on demand, as a means to biopsy the microenvironment or deliver biologics to a diseased site. With the programming capabilities introduced in **Chapter 4**, the timing of these operations can be pre-determined.

Miniaturization challenges and autonomy

Currently there is no framework that would allow the engineering of microscopic devices that move autonomously toward a target location. Considering the capabilities of single-celled organisms and eukaryotic cells, mechanochemical control based on organic components such as nucleic acids and proteins is particularly suited for microscale systems. In living systems, biochemical computation drives mechanical work through direct interactions among regulatory and motor proteins. Coupling the physical and chemical properties of polymers with the conformation changes or binding events of nuclei acids and proteins may provide a framework for developing programmable on-board controllers for microrobots.

In this thesis, I proposed a number of solutions to decouple power transfer from control of motion. Acoustic waves turn the actuators on and off nut do not impose restrictions on their orientation or motion. This powering scheme is compatible with mechanochemical control. Furthermore, acoustic actuation do not impose restrictions on material properties. For sharp edge actuation, the coupling between structural resonance and material properties must be considered. Higher Young's modulus results in smaller deflection of sharp edges. To address this issue, the design of the robot and the frequency of excitation can be tuned according to the material properties. In bubble-based actuation, the material properties of the machine is completely decoupled from the characteristics of the power signal.

Optimization is essential for the development of next generation biomedical devices that leverages the acoustic forces generated by oscillating bubbles for various tasks. For optimal operation, sharp-edge and bubble based actuators have to be designed considering multiple factors. For example, the bubble should be excited at its first natural frequency, which should coincide with the exciting element (e.g., piezoelectric transducer) effective frequency band. The bubble's natural frequencies depend on its geometry and surrounding fluid properties. Decreasing the bubble's volume, the water-air interface diameter increases the natural frequencies. Higher natural frequencies result in the generation of stronger acoustic force for the same displacement amplitude, because acoustic streaming increases quadratically with increasing velocity. However, a smaller opening decreases the acoustic streaming because a smaller portion of the bubble oscillates. The secondary radiation forces decrease quadratically with the distance between bubbles as $F \sim 1/d^2$ among other parameters.

Taken together, the design, fabrication, and actuation techniques presented in this thesis are compatible with miniaturization as long as coupled parameters are tuned accordingly.

References

[1] E. M. Purcell, "Life at low Reynolds number", *American Journal of Physics*, vol. 45, no. 1, pp. 3–11, Jan. 1977.

[2] W. J. Polacheck and C. S. Chen, "Measuring cell-generated forces: A guide to the available tools", *Nature Methods*, vol. 13, no. 5, pp. 415–423, 2016.

[3] Y. Hiratsuka, M. Miyata, T. Tada, and T. Q. Uyeda, "A microrotary motor powered by bacteria", *Proceedings of the National Academy of Sciences of the United States of America*, vol. 103, no. 37, pp. 13 618–13 623, 2006.

[4] L. Zhang, J. J. Abbott, L. Dong, B. E. Kratochvil, D. Bell, and B. J. Nelson, "Artificial bacterial flagella: Fabrication and magnetic control", *Applied Physics Letters*, vol. 94, no. 6, 2009.

[5] A. Ghosh and P. Fischer, "Controlled Propulsion of Artificial Magnetic Nanostructured Propellers", *Nano Letters*, vol. 9, no. 6, pp. 2243–2245, Jun. 2009.

[6] R. Dreyfus, J. Baudry, M. L. Roper, M. Fermigier, H. A. Stone, and J. Bibette, "Microscopic artificial swimmers", *Nature*, vol. 437, no. 7060, pp. 862–865, Oct. 2005.

[7] X. Z. Chen, B. Jang, D. Ahmed, C. Hu, C. De Marco, M. Hoop, F. Mushtaq, B. J. Nelson, and S. Pané, "Small-Scale Machines Driven by External Power Sources", *Advanced Materials*, vol. 30, no. 15, pp. 1–22, 2018.

[8] K. Satoshi, S. Hong-Bo, T. Tomokazu, and T. Kenji, "Finer features for functional microdevices", *Nature*, vol. 412, pp. 697–698, 2001.

[9] M. P. Lee, G. J. Cooper, T. Hinkley, G. M. Gibson, M. J. Padgett, and L. Cronin, "Development of a 3D printer using scanning projection stereolithography", *Scientific Reports*, vol. 5, 2015.

[10] J. Li and M. Pumera, "3D printing of functional microrobots", *Chemical Society Reviews*, vol. 50, no. 4, pp. 2794–2838, 2021.

[11] C. N. LaFratta, J. T. Fourkas, T. Baldacchini, and R. A. Farrer, "Multiphoton fabrication", *Angewandte Chemie - International Edition*, vol. 46, no. 33, pp. 6238–6258, 2007.

[12] S. Tottori, L. Zhang, F. Qiu, K. K. Krawczyk, A. Franco-Obregõn, and B. J. Nelson, "Magnetic helical micromachines: Fabrication, controlled swimming, and cargo transport", *Advanced Materials*, vol. 24, no. 6, pp. 811–816, 2012.

[13] B. Özkale, R. Parreira, A. Bekdemir, L. Pancaldi, E. Özelçi, C. Amadio, M. Kaynak, F. Stellacci, D. J. Mooney, and M. S. Sakar, "Modular soft robotic microdevices for dexterous biomanipulation", *Lab on a Chip*, vol. 19, no. 5, pp. 778–788, 2019.

[14] C. Ohm, C. Serra, and R. Zentel, "A Continuous Flow Synthesis of Micrometer-Sized Actuators from Liquid Crystalline Elastomers", *Advanced Materials*, vol. 21, no. 47, pp. 4859–4862, Dec. 2009.

[15] J. J. Abbott, K. E. Peyer, M. C. Lagomarsino, L. Zhang, L. Dong, I. K. Kaliakatsos, and B. J. Nelson, "How Should Microrobots Swim?", *The International Journal of Robotics Research*, vol. 28, no. 11-12, pp. 1434–1447, Nov. 2009.

[16] P. Fischer and A. Ghosh, "Magnetically actuated propulsion at low Reynolds numbers: towards nanoscale control", *Nanoscale*, vol. 3, no. 2, pp. 557–563, 2011.

[17] K. E. Peyer, L. Zhang, and B. J. Nelson, "Bio-inspired magnetic swimming microrobots for biomedical applications", *Nanoscale*, vol. 5, no. 4, pp. 1259–1272, 2013.

[18] H. Zhou, C. C. Mayorga-Martinez, S. Pané, L. Zhang, and M. Pumera, "Magnetically Driven Micro and Nanorobots", *Chemical Reviews*, vol. 121, no. 8, pp. 4999–5041, Apr. 2021.

[19] S. Fusco, M. S. Sakar, S. Kennedy, C. Peters, R. Bottani, F. Starsich, A. Mao, G. A. Sotiriou, S. Pané, S. E. Pratsinis, D. Mooney, and B. J. Nelson, "An integrated microrobotic platform for on-demand, targeted therapeutic interventions", *Advanced Materials*, vol. 26, no. 6, pp. 952–957, 2014.

[20] S. Palagi, D. P. Singh, and P. Fischer, "Light-Controlled Micromotors and Soft Microrobots", *Advanced Optical Materials*, vol. 7, no. 16, p. 1 900 370, Aug. 2019.

[21] T. Ding, V. K. Valev, A. R. Salmon, C. J. Forman, S. K. Smoukov, O. A. Scherman, D. Frenkel, and J. J. Baumberg, "Light-induced actuating nanotransducers", *Proceedings of the National Academy of Sciences*, vol. 113, no. 20, pp. 5503–5507, May 2016.

[22] A. Mourran, H. Zhang, R. Vinokur, and M. Möller, "Soft Microrobots Employing Nonequilibrium Actuation via Plasmonic Heating", *Advanced Materials*, vol. 29, no. 2, p. 1 604 825, Jan. 2017.

[23] M. Camacho-Lopez, H. Finkelmann, P. Palffy-Muhoray, and M. Shelley, "Fast liquid-crystal elastomer swims into the dark", *Nature Materials*, vol. 3, no. 5, pp. 307–310, May 2004.

[24] H. Zeng, P. Wasylczyk, C. Parmeggiani, D. Martella, M. Burresi, and D. S. Wiersma, "Light-Fueled Microscopic Walkers", *Advanced Materials*, vol. 27, no. 26, pp. 3883–3887, 2015.

[25] H. Shahsavan, A. Aghakhani, H. Zeng, Y. Guo, Z. S. Davidson, A. Priimagi, and M. Sitti, "Bioinspired underwater locomotion of light-driven liquid crystal gels", *Proceedings of the National Academy of Sciences of the United States of America*, vol. 117, no. 10, pp. 5125–5133, 2020.

[26] S. Palagi, A. G. Mark, S. Y. Reigh, K. Melde, T. Qiu, H. Zeng, C. Parmeggiani, D. Martella, A. Sanchez-Castillo, N. Kapernaum, F. Giesselmann, D. S. Wiersma, E. Lauga, and P. Fischer, "Structured light enables biomimetic swimming and versatile locomotion of photoresponsive soft microrobots", *Nature Materials*, vol. 15, no. 6, pp. 647–653, 2016.

[27] W. Hu, G. Z. Lum, M. Mastrangeli, and M. Sitti, "Small-scale soft-bodied robot with multimodal locomotion", *Nature*, vol. 554, no. 7690, pp. 81–85, 2018.

[28] J. Kim, S. E. Chung, S. E. Choi, H. Lee, J. Kim, and S. Kwon, "Programming magnetic anisotropy in polymeric microactuators", *Nature Materials*, vol. 10, no. 10, pp. 747–752, 2011.

[29] X. Hu, I. C. Yasa, Z. Ren, S. R. Goudu, H. Ceylan, W. Hu, and M. Sitti, "Magnetic soft micromachines made of linked microactuator networks", *Science Advances*, vol. 7, no. 23, pp. 1–10, 2021.

[30] Y. Kim, H. Yuk, R. Zhao, S. A. Chester, and X. Zhao, "Printing ferromagnetic domains for untethered fast-transforming soft materials", *Nature*, vol. 558, no. 7709, pp. 274–279, Jun. 2018.

[31] G. Z. Lum, Z. Ye, X. Dong, H. Marvi, O. Erin, W. Hu, and M. Sitti, "Shape-programmable magnetic soft matter", *Proceedings of the National Academy of Sciences of the United States of America*, vol. 113, no. 41, E6007–E6015, 2016.

[32] Z. Ren, W. Hu, X. Dong, and M. Sitti, "Multi-functional soft-bodied jellyfish-like swimming", *Nature Communications*, vol. 10, no. 1, p. 2703, Dec. 2019.

[33] J. Cui, T. Y. Huang, Z. Luo, P. Testa, H. Gu, X. Z. Chen, B. J. Nelson, and L. J. Heyderman, "Nanomagnetic encoding of shape-morphing micromachines", *Nature*, vol. 575, no. 7781, pp. 164–168, 2019.

[34] T. Y. Huang, M. S. Sakar, A. Mao, A. J. Petruska, F. Qiu, X. B. Chen, S. Kennedy, D. Mooney, and B. J. Nelson, "3D Printed Microtransporters: Compound Micromachines

for Spatiotemporally Controlled Delivery of Therapeutic Agents", *Advanced Materials*, vol. 27, no. 42, pp. 6644–6650, 2015.

[35] V. Garcia-Gradilla, S. Sattayasamitsathit, F. Soto, F. Kuralay, C. Yardimci, D. Wiitala, M. Galarnyk, and J. Wang, "Ultrasound-propelled nanoporous gold wire for efficient drug loading and release", *Small*, vol. 10, no. 20, pp. 4154–4159, 2014.

[36] A. Marzo, A. Ghobrial, L. Cox, M. Caleap, A. Croxford, and B. W. Drinkwater, "Realization of compact tractor beams using acoustic delay-lines", *Applied Physics Letters*, vol. 110, no. 1, pp. 1–6, 2017.

[37] S. P. Zhang, J. Lata, C. Chen, J. Mai, F. Guo, Z. Tian, L. Ren, Z. Mao, P. H. Huang, P. Li, S. Yang, and T. J. Huang, "Digital acoustofluidics enables contactless and programmable liquid handling", *Nature Communications*, vol. 9, no. 1, pp. 1–11, 2018.

[38] M. S. Ozdas, A. S. Shah, P. M. Johnson, N. Patel, M. Marks, T. B. Yasar, U. Stalder, L. Bigler, W. von der Behrens, S. R. Sirsi, and M. F. Yanik, "Non-invasive molecularly-specific millimeter-resolution manipulation of brain circuits by ultrasound-mediated aggregation and uncaging of drug carriers", *Nature Communications*, vol. 11, no. 1, pp. 1–15, 2020.

[39] Z. Wu, L. Li, Y. Yang, P. Hu, Y. Li, S. Y. Yang, L. V. Wang, and W. Gao, "A microrobotic system guided by photoacoustic computed tomography for targeted navigation in intestines in vivo", *Science Robotics*, vol. 4, no. 32, 2019.

[40] D. Ahmed, M. Lu, A. Nourhani, P. E. Lammert, Z. Stratton, H. S. Muddana, V. H. Crespi, and T. J. Huang, "Selectively manipulable acoustic-powered microswimmers", *Scientific Reports*, vol. 5, pp. 1–8, 2015.

[41] N. Bertin, T. A. Spelman, O. Stephan, L. Gredy, M. Bouriau, E. Lauga, and P. Marmottant, "Propulsion of bubble-based acoustic microswimmers", *Physical Review Applied*, vol. 4, no. 6, pp. 1–5, 2015.

[42] M. Kaynak, A. Ozcelik, A. Nourhani, P. E. Lammert, V. H. Crespi, and T. J. Huang, "Acoustic actuation of bioinspired microswimmers", *Lab on a Chip*, vol. 17, no. 3, pp. 395–400, 2017.

[43] D. Ahmed, T. Baasch, B. Jang, S. Pane, J. Dual, and B. J. Nelson, "Artificial Swimmers Propelled by Acoustically Activated Flagella", *Nano Letters*, vol. 16, no. 8, pp. 4968–4974, 2016.

[44] C. Wang, Q. Wang, R. F. Dong, and Y. P. Cai, "Dynamic self-assembly of micro-nanomotor", *Inorganic Chemistry Communications*, vol. 91, pp. 8–15, 2018.

[45] N. Bertin, T. A. Spelman, T. Combriat, H. Hue, O. Stéphan, E. Lauga, and P. Marmottant, "Bubble-based acoustic micropropulsors: active surfaces and mixers", *Lab on a Chip*, vol. 17, no. 8, pp. 1515–1528, 2017.

[46] L. Ren, N. Nama, J. M. McNeill, F. Soto, Z. Yan, W. Liu, W. Wang, J. Wang, and T. E. Mallouk, "3D steerable, acoustically powered microswimmers for single-particle manipulation", *Science Advances*, vol. 5, no. 10, 2019.

[47] A. Aghakhani, O. Yasa, P. Wrede, and M. Sitti, "Acoustically powered surface-slipping mobile microrobots", *Proceedings of the National Academy of Sciences of the United States of America*, vol. 117, no. 7, pp. 3469–3477, 2020.

[48] J. D. N. Cheeke, *Fundamentals and Applications of Ultrasonic Waves*. New York: CRC Press LLC, 2002.

[49] J. Dual and D. Möller, "Acoustofluidics 4: Piezoelectricity and application in the excitation of acoustic fields for ultrasonic particle manipulation", *Lab on a Chip*, vol. 12, no. 3, pp. 506–514, 2012.

[50] W. Denk, K. R. Delaney, A. Gelperin, D. Kleinfeld, B. W. Strowbridge, D. W. Tank, and R. Yuste, "Anatomical and functional imaging of neurons using 2-photon laser scanning microscopy", *Journal of Neuroscience Methods*, vol. 54, no. 2, pp. 151–162, 1994.

[51] J. T. Trachtenberg, B. E. Chen, G. W. Knott, G. Feng, J. R. Sanes, E. Welker, and K. Svoboda, "Long-term in vivo imaging of experience-dependent synaptic plasticity in adult cortex", *Nature*, vol. 420, no. 6917, pp. 788–794, 2002.

[52] T. H. Kim, Y. Zhang, J. Lecoq, J. C. Jung, J. Li, H. Zeng, C. M. Niell, and M. J. Schnitzer, "Long-Term Optical Access to an Estimated One Million Neurons in the Live Mouse Cortex", *Cell Reports*, vol. 17, no. 12, pp. 3385–3394, 2016.

[53] M. L. Andermann, N. B. Gilfoy, G. J. Goldey, R. N. Sachdev, M. Wölfel, D. A. McCormick, R. C. Reid, and M. J. Levene, "Chronic Cellular Imaging of Entire Cortical Columns in Awake Mice Using Microprisms", *Neuron*, vol. 80, no. 4, pp. 900–913, 2013.

[54] G. J. Goldey, D. K. Roumis, L. L. Glickfeld, A. M. Kerlin, R. C. Reid, V. Bonin, D. P. Schafer, and M. L. Andermann, "Removable cranial windows for long-term imaging in awake mice", *Nature Protocols*, vol. 9, no. 11, pp. 2515–2538, 2014.

[55] J. D. Seelig and V. Jayaraman, "Neural dynamics for landmark orientation and angular path integration", *Nature*, vol. 521, no. 7551, pp. 186–191, 2015.

[56] S. Pick and R. Strauss, "Goal-driven behavioral adaptations in gap-climbing Drosophila", *Current Biology*, vol. 15, no. 16, pp. 1473–1478, 2005.

[57] K. Asahina, "Neuromodulation and Strategic Action Choice in Drosophila Aggression", *Annual Review of Neuroscience*, vol. 40, pp. 51–75, 2017.

[58] H. J. Pavlou and S. F. Goodwin, "Courtship behavior in Drosophila melanogaster: Towards a 'courtship connectome'", *Current Opinion in Neurobiology*, vol. 23, no. 1, pp. 76–83, 2013.

[59] J. D. Seelig, M. E. Chiappe, G. K. Lott, A. Dutta, J. E. Osborne, M. B. Reiser, and V. Jayaraman, "Two-photon calcium imaging from head-fixed Drosophila during optomotor walking behavior", *Nature Methods*, vol. 7, no. 7, pp. 535–540, 2010.

[60] G. Maimon, A. D. Straw, and M. H. Dickinson, "Active flight increases the gain of visual motion processing in Drosophila", *Nature Neuroscience*, vol. 13, no. 3, pp. 393–399, 2010.

[61] D. Grover, T. Katsuki, and R. J. Greenspan, "Flyception: Imaging brain activity in freely walking fruit flies", *Nature Methods*, vol. 13, no. 7, pp. 569–572, 2016.

[62] A. Flores Valle, R. Honnef, and J. D. Seelig, "Automated long-term two-photon imaging in head-fixed walking Drosophila", *bioRxiv*, vol. 9, p. 2021.03.20.436241, 2021.

[63] N. A. Nelson, X. Wang, D. Cook, E. M. Carey, and A. Nimmerjahn, "Imaging spinal cord activity in behaving animals", *Experimental Neurology*, vol. 320, no. June, p. 112 974, 2019.

[64] C.-L. Chen, L. Hermans, M. C. Viswanathan, D. Fortun, F. Aymanns, M. Unser, A. Cammarato, M. H. Dickinson, and P. Ramdya, "Imaging neural activity in the ventral nerve cord of behaving adult Drosophila", *Nature Communications*, vol. 9, no. 1, p. 4390, Dec. 2018.

[65] A. Tsubouchi, T. Yano, T. K. Yokoyama, C. Murtin, H. Otsuna, and K. Ito, "Topological and modality-specific representation of somatosensory information in the fly brain", *Science*, vol. 358, no. 6363, pp. 615–623, 2017.

[66] J. C. Tuthill and E. Azim, "Proprioception", *Current Biology*, vol. 28, no. 5, R194–R203, 2018.

[67] S. S. Bidaye, T. Bockemühl, and A. Büschges, "Six-legged walking in insects: How CPGs, peripheral feedback, and descending signals generate coordinated and adaptive motor rhythms", *Journal of Neurophysiology*, vol. 119, no. 2, pp. 459–475, 2018.

[68] T. Chen, O. R. Bilal, K. Shea, and C. Daraio, "Harnessing bistability for directional propulsion of soft, untethered robots", *Proceedings of the National Academy of Sciences of the United States of America*, vol. 115, no. 22, pp. 5698–5702, 2018.

[69] Y. Liu, J. H. Campbell, O. Stein, L. Jiang, J. Hund, and Y. Lu, "Deformation behavior of foam laser targets fabricated by two-photon polymerization", *Nanomaterials*, vol. 8, no. 7, pp. 1–20, 2018.

[70] S. Günel, H. Rhodin, D. Morales, J. Campagnolo, P. Ramdya, and P. Fua, "Deepfly3D, a deep learning-based approach for 3D limb and appendage tracking in tethered, adult Drosophila", *eLife*, vol. 8, pp. 1–23, 2019.

[71] R. Sen, M. Wu, K. Branson, A. Robie, G. M. Rubin, and B. J. Dickson, "Moonwalker Descending Neurons Mediate Visually Evoked Retreat in Drosophila", *Current Biology*, vol. 27, no. 5, pp. 766–771, 2017.

[72] N. C. Klapoetke, Y. Murata, S. S. Kim, S. R. Pulver, A. Birdsey-Benson, Y. K. Cho, T. K. Morimoto, A. S. Chuong, E. J. Carpenter, Z. Tian, J. Wang, Y. Xie, Z. Yan, Y. Zhang, B. Y. Chow, B. Surek, M. Melkonian, V. Jayaraman, M. Constantine-Paton, G. K. S. Wong, and E. S. Boyden, "Independent optical excitation of distinct neural populations", *Nature Methods*, vol. 11, no. 3, pp. 338–346, 2014.

[73] S. S. Bidaye, C. Machacek, Y. Wu, and D. B. J., "Neuronal Control of Drosophila", *Science*, vol. 344, no. April, pp. 97–101, 2014.

[74] B. J. Nelson, I. K. Kaliakatsos, and J. J. Abbott, "Microrobots for minimally invasive medicine", *Annual Review of Biomedical Engineering*, vol. 12, pp. 55–85, 2010.

[75] X. Yan, Q. Zhou, M. Vincent, Y. Deng, J. Yu, J. Xu, T. Xu, T. Tang, L. Bian, Y. X. J. Wang, K. Kostarelos, and L. Zhang, "Multifunctional biohybrid magnetite microrobots for imaging-guided therapy", *Science Robotics*, vol. 2, no. 12, pp. 1–15, 2017.

[76] C. K. Schmidt, M. Medina-Sánchez, R. J. Edmondson, and O. G. Schmidt, "Engineering microrobots for targeted cancer therapies from a medical perspective", *Nature Communications*, vol. 11, no. 1, pp. 1–18, 2020.

[77] S. M. Won, L. Cai, P. Gutruf, and J. A. Rogers, "Wireless and battery-free technologies for neuroengineering", *Nature Biomedical Engineering*, 2021.

[78] V. B. Koman, P. Liu, D. Kozawa, A. T. Liu, A. L. Cottrill, Y. Son, J. A. Lebron, and M. S. Strano, "Colloidal nanoelectronic state machines based on 2D materials for aerosolizable electronics", *Nature Nanotechnology*, vol. 13, no. 9, pp. 819–827, 2018.

[79] M. Z. Miskin, A. J. Cortese, K. Dorsey, E. P. Esposito, M. F. Reynolds, Q. Liu, M. Cao, D. A. Muller, P. L. McEuen, and I. Cohen, "Electronically integrated, mass-manufactured, microscopic robots", *Nature*, vol. 584, no. 7822, pp. 557–561, 2020.

[80] A. J. Cortese, C. L. Smart, T. Wang, M. F. Reynolds, S. L. Norris, Y. Ji, S. Lee, A. Mok, C. Wu, F. Xia, N. I. Ellis, A. C. Molnar, C. Xu, and P. L. McEuen, "Microscopic sensors using

optical wireless integrated circuits", *Proceedings of the National Academy of Sciences of the United States of America*, vol. 117, no. 17, pp. 9173–9179, 2020.

[81] J. Li and D. J. Mooney, "Designing hydrogels for controlled drug delivery", *Nature Reviews Materials*, vol. 1, no. 12, 2016.

[82] C. L. Van Oosten, C. W. Bastiaansen, and D. J. Broer, "Printed artificial cilia from liquid-crystal network actuators modularly driven by light", *Nature Materials*, vol. 8, no. 8, pp. 677–682, 2009.

[83] E. Diller, J. Zhuang, G. Zhan Lum, M. R. Edwards, and M. Sitti, "Continuously distributed magnetization profile for millimeter-scale elastomeric undulatory swimming", *Applied Physics Letters*, vol. 104, no. 17, 2014.

[84] H. W. Huang, M. S. Sakar, A. J. Petruska, S. Pané, and B. J. Nelson, "Soft micromachines with programmable motility and morphology", *Nature Communications*, vol. 7, pp. 1–10, 2016.

[85] J. J. Abbott, E. Diller, and A. J. Petruska, "Magnetic Methods in Robotics", *Annual Review of Control, Robotics, and Autonomous Systems*, vol. 3, no. 1, pp. 57–90, 2020.

[86] K. Bertoldi, V. Vitelli, J. Christensen, and M. Van Hecke, "Flexible mechanical metamaterials", *Nature Reviews Materials*, vol. 2, 2017.

[87] D. J. Preston, P. Rothemund, H. J. Jiang, M. P. Nemitz, J. Rawson, Z. Suo, and G. M. Whitesides, "Digital logic for soft devices", *Proceedings of the National Academy of Sciences of the United States of America*, vol. 116, no. 16, pp. 7750–7759, 2019.

[88] M. Sitti, "Physical intelligence as a new paradigm", *Extreme Mechanics Letters*, vol. 46, p. 101 340, 2021.

[89] A. Dolev, M. Kaynak, and M. S. Sakar, "On-Board Mechanical Control Systems for Untethered Microrobots", *Advanced Intelligent Systems*, vol. 2000233, p. 2 000 233, 2021.

[90] K. Son, J. S. Guasto, and R. Stocker, "Bacteria can exploit a flagellar buckling instability to change direction", *Nature Physics*, vol. 9, no. 8, pp. 494–498, 2013.

[91] M. J. Kühn, F. K. Schmidt, B. Eckhardt, and K. M. Thormann, "Bacteria exploit a polymorphic instability of the flagellar filament to escape from traps", *Proceedings of the National Academy of Sciences of the United States of America*, vol. 114, no. 24, pp. 6340–6345, 2017.

[92] P. Rothemund, A. Ainla, L. Belding, D. J. Preston, S. Kurihara, Z. Suo, and G. M. Whitesides, "A soft, bistable valve for autonomous control of soft actuators", *Science Robotics*, vol. 3, no. 16, pp. 1–11, 2018.

[93] M. Wehner, R. L. Truby, D. J. Fitzgerald, B. Mosadegh, G. M. Whitesides, J. A. Lewis, and R. J. Wood, "An integrated design and fabrication strategy for entirely soft, autonomous robots", *Nature*, vol. 536, no. 7617, pp. 451–455, 2016.

[94] C. C. Alcântara, F. C. Landers, S. Kim, C. De Marco, D. Ahmed, B. J. Nelson, and S. Pané, "Mechanically interlocked 3D multi-material micromachines", *Nature Communications*, vol. 11, no. 1, 2020.

[95] H. W. Huang, F. E. Uslu, P. Katsamba, E. Lauga, M. S. Sakar, and B. J. Nelson, "Adaptive locomotion of artificial microswimmers", *Science Advances*, vol. 5, no. 1, pp. 1–8, 2019.

[96] T. Huang, H. Huang, D. D. Jin, Q. Y. Chen, J. Y. Huang, L. Zhang, and H. L. Duan, "Four-dimensional micro-building blocks", no. January, pp. 1–10, 2020.

[97] G. Adam, A. Benouhiba, K. Rabenorosoa, C. Clévy, and D. J. Cappelleri, "4D Printing: Enabling Technology for Microrobotics Applications", *Advanced Intelligent Systems*, vol. 3, no. 5, p. 2 000 216, 2021.

[98] D. Ahmed, A. Ozcelik, N. Bojanala, N. Nama, A. Upadhyay, Y. Chen, W. Hanna-Rose, and T. J. Huang, "Rotational manipulation of single cells and organisms using acoustic waves", *Nature Communications*, vol. 7, 2016.

[99] G. Regnault, C. Mauger, P. Blanc-Benon, and C. Inserra, "Secondary radiation force between two closely spaced acoustic bubbles", *Physical Review E*, vol. 102, no. 3, p. 31 101, 2020.

[100] T. G. Leighton, Ed., *The Acoustic Bubble*, 1st editio. Elsevier, 1994.

[101] T. Qiu, F. Adams, S. Palagi, K. Melde, A. Mark, U. Wetterauer, A. Miernik, and P. Fischer, "Wireless Acoustic-Surface Actuators for Miniaturized Endoscopes", *ACS Applied Materials and Interfaces*, vol. 9, no. 49, pp. 42 536–42 543, 2017.

[102] R. Bahadur, L. M. Russell, and S. Alavi, "Surface tensions in NaCl-water-air systems from MD simulations", *Journal of Physical Chemistry B*, vol. 111, no. 41, pp. 11 989–11 996, 2007.

[103] A. E. Ismail, G. S. Grest, D. R. Heine, M. J. Stevens, and M. Tsige, "Interfacial structure and dynamics of siloxane systems: pdms-vapor and pdms-water", *Macromolecules*, vol. 42, no. 8, pp. 3186–3194, 2009.

[104] C. Wang, B. Rallabandi, and S. Hilgenfeldt, "Frequency dependence and frequency control of microbubble streaming flows", *Physics of Fluids*, vol. 25, no. 2, 2013.

[105] B. Audoly and Y. Pomeau, *Elasticity and geometry: from hair curls to the non-linear response of shells*. Oxford university press, 2010.

[106] L. L. Howell, S. P. Magleby, and B. M. Olsen, Eds., *Handbook of Compliant Mechanisms*. Wiley, Feb. 2013.

[107] R. Guseinov, C. McMahan, J. Pérez, C. Daraio, and B. Bickel, "Programming temporal morphing of self-actuated shells", *Nature Communications*, vol. 11, no. 1, pp. 1–7, 2020.

[108] D. J. Ewins, *Modal Testing: Theory, Practice and Application, 2nd Edition*, 2nd editio. Wiley, 2009.

[109] H. Gelderblom, A. G. Zijlstra, L. van Wijngaarden, and A. Prosperetti, "Oscillations of a gas pocket on a liquid-covered solid surface", *Physics of Fluids*, vol. 24, no. 12, p. 122 101, Dec. 2012.

[110] H. Lamb, *Hydrodynamics*, 6th editio. New York: Dover publications, 1945.

[111] S. S. Rao, *Vibration of Continuous Systems*, 2nd Editio. Wiley, 2019.

[112] D. Gritsenko, Y. Lin, V. Hovorka, Z. Zhang, A. Ahmadianyazdi, and J. Xu, "Vibrational modes prediction for water-air bubbles trapped in circular microcavities", *Physics of Fluids*, vol. 30, no. 8, p. 082 001, Aug. 2018.

[113] R. Gabai, D. Ilssar, R. Shaham, N. Cohen, and I. Bucher, "A rotational traveling wave based levitation device – Modelling, design, and control", *Sensors and Actuators A: Physical*, vol. 255, pp. 34–45, Mar. 2017.

[114] J. CHANG and J. WICKERT, "RESPONSE OF MODULATED DOUBLET MODES TO TRAVELLING WAVE EXCITATION", *Journal of Sound and Vibration*, vol. 242, no. 1, pp. 69–83, Apr. 2001.

[115] V. C. Henriquez and P. M. Juhl, "No Title", in *Proceedings of Internoise*, Lisbon, Portugal, 2010, pp. 1–10.

[116] M. Hippler, K. Weißenbruch, K. Richler, E. D. Lemma, M. Nakahata, B. Richter, C. Barner-Kowollik, Y. Takashima, A. Harada, E. Blasco, M. Wegener, M. Tanaka, and M. Bastmeyer, "Mechanical stimulation of single cells by reversible host-guest interactions in 3D microscaffolds", *Science Advances*, vol. 6, no. 39, 2020.

[117] R. Barnkob, P. Augustsson, T. Laurell, and H. Bruus, "Measuring the local pressure amplitude in microchannel acoustophoresis", *Lab on a Chip*, vol. 10, no. 5, pp. 563–570, 2010.

[118] A. A. Doinikov and S. T. Zavtrak, "On the mutual interaction of two gas bubbles in a sound field", *Physics of Fluids*, vol. 7, no. 8, pp. 1923–1930, 1995.

[119] A. A. Doinikov, *Bjerkness forces and translational bubble dynamics*, January 2005. 2005, p. 338.

[120] H. Bruus, "Acoustofluidics 10: Scaling laws in acoustophoresis", *Lab on a Chip*, vol. 12, no. 9, pp. 1578–1586, 2012.

[121] Y. Jiang, L. M. Korpas, and J. R. Raney, "Bifurcation-based embodied logic and autonomous actuation", *Nature Communications*, vol. 10, no. 1, pp. 1–10, 2019.

[122] L. S. Novelino, Q. Ze, S. Wu, G. H. Paulino, and R. Zhao, "Untethered control of functional origami microrobots with distributed actuation", *Proceedings of the National Academy of Sciences of the United States of America*, vol. 117, no. 39, pp. 24 096–24 101, 2020.

[123] T. Chen, M. Pauly, and P. M. Reis, "A reprogrammable mechanical metamaterial with stable memory", *Nature*, vol. 589, no. 7842, pp. 386–390, 2021.

[124] M. Hippler, E. Blasco, J. Qu, M. Tanaka, C. Barner-Kowollik, M. Wegener, and M. Bastmeyer, "Controlling the shape of 3D microstructures by temperature and light", *Nature Communications*, vol. 10, no. 1, pp. 1–8, 2019.

[125] D. Gräfe, A. Wickberg, M. M. Zieger, M. Wegener, E. Blasco, and C. Barner-Kowollik, "Adding chemically selective subtraction to multi-material 3D additive manufacturing", *Nature Communications*, vol. 9, no. 1, pp. 1–6, 2018.

[126] A. A. Doinikov, M. S. Gerlt, A. Pavlic, and J. Dual, "Acoustic streaming produced by sharp-edge structures in microfluidic devices", *Microfluidics and Nanofluidics*, vol. 24, no. 5, pp. 1–13, 2020.

[127] A. A. Doinikov, M. S. Gerlt, and J. Dual, "Acoustic Radiation Forces Produced by Sharp-Edge Structures in Microfluidic Systems", *Physical Review Letters*, vol. 124, no. 15, p. 154 501, 2020.

[128] M. Kaynak, P. Dirix, and M. S. Sakar, "Addressable Acoustic Actuation of 3D Printed Soft Robotic Microsystems", *Advanced Science*, vol. 7, no. 20, pp. 1–9, 2020.

[129] R. Niu, C. X. Du, E. Esposito, J. Ng, M. P. Brenner, P. L. McEuen, and I. Cohen, "Magnetic handshake materials as a scale-invariant platform for programmed self-assembly", *Proceedings of the National Academy of Sciences of the United States of America*, vol. 116, no. 49, pp. 24 402–24 407, 2019.

[130] H. Gu, Q. Boehler, D. Ahmed, and B. J. Nelson, "Magnetic quadrupole assemblies with arbitrary shapes and magnetizations", *Science Robotics*, vol. 4, no. 35, pp. 1–8, 2019.

[131] J. F. Louf, N. Bertin, B. Dollet, O. Stephan, and P. Marmottant, "Hovering Microswimmers Exhibit Ultrafast Motion to Navigate under Acoustic Forces", *Advanced Materials Interfaces*, vol. 5, no. 16, pp. 1–6, 2018.

[132] E. K. Sackmann, A. L. Fulton, and D. J. Beebe, "The present and future role of microfluidics in biomedical research", *Nature*, vol. 507, no. 7491, pp. 181–189, 2014.

[133] C. J. Kearney and D. J. Mooney, "Macroscale delivery systems for molecular and cellular payloads", *Nature Materials*, vol. 12, no. 11, pp. 1004–1017, 2013.

[134] C. Steiger, A. Abramson, P. Nadeau, A. P. Chandrakasan, R. Langer, and G. Traverso, "Ingestible electronics for diagnostics and therapy", *Nature Reviews Materials*, vol. 4, no. 2, pp. 83–98, 2019.

[135] Y. Wang and D. S. Kohane, "External triggering and triggered targeting strategies for drug delivery", *Nature Reviews Materials*, vol. 2, 2017.

[136] H. Zhang, J. K. Jackson, and M. Chiao, "Microfabricated Drug Delivery Devices: Design, Fabrication, and Applications", *Advanced Functional Materials*, vol. 27, no. 45, pp. 1–31, 2017.

[137] J. G. McCall and J. W. Jeong, "Minimally invasive probes for programmed microfluidic delivery of molecules in vivo", *Current Opinion in Pharmacology*, vol. 36, pp. 78–85, 2017.

[138] Y. H. Jung, J. U. Kim, J. S. Lee, J. H. Shin, W. Jung, J. Ok, and T. i. Kim, "Injectable Biomedical Devices for Sensing and Stimulating Internal Body Organs", *Advanced Materials*, vol. 32, no. 16, pp. 1–25, 2020.

[139] Y. Zhang, D. C. Castro, Y. Han, Y. Wu, H. Guo, Z. Weng, Y. Xue, J. Ausra, X. Wang, R. Li, G. Wu, A. Vázquez-Guardado, Y. Xie, Z. Xie, D. Ostojich, D. Peng, R. Sun, B. Wang, Y. Yu, J. P. Leshock, S. Qu, C. J. Su, W. Shen, T. Hang, A. Banks, Y. Huang, J. Radulovic, P. Gutruf, M. R. Bruchas, and J. A. Rogers, "Battery-free, lightweight, injectable microsystem for in vivo wireless pharmacology and optogenetics", *Proceedings of the National Academy of Sciences of the United States of America*, vol. 116, no. 43, pp. 21 427–21 437, 2019.

[140] C. Dagdeviren, K. B. Ramadi, P. Joe, K. Spencer, H. N. Schwerdt, H. Shimazu, S. Delcasso, K. I. Amemori, C. Nunez-Lopez, A. M. Graybiel, M. J. Cima, and R. Langer, "Miniaturized neural system for chronic, local intracerebral drug delivery", *Science Translational Medicine*, vol. 10, no. 425, pp. 1–11, 2018.

[141] J. W. Jeong, J. G. McCall, G. Shin, Y. Zhang, R. Al-Hasani, M. Kim, S. Li, J. Y. Sim, K. I. Jang, Y. Shi, D. Y. Hong, Y. Liu, G. P. Schmitz, L. Xia, Z. He, P. Gamble, W. Z. Ray, Y. Huang, M. R. Bruchas, and J. A. Rogers, "Wireless Optofluidic Systems for Programmable In Vivo Pharmacology and Optogenetics", *Cell*, vol. 162, no. 3, pp. 662–674, 2015.

[142] P. Gutruf and J. A. Rogers, "Implantable, wireless device platforms for neuroscience research", *Current Opinion in Neurobiology*, vol. 50, pp. 42–49, 2018.

[143] X. He, M. Aizenberg, O. Kuksenok, L. D. Zarzar, A. Shastri, A. C. Balazs, and J. Aizenberg, "Synthetic homeostatic materials with chemo-mechano-chemical self-regulation", *Nature*, vol. 487, no. 7406, pp. 214–218, 2012.

[144] L. Dong, A. K. Agarwal, D. J. Beebe, and H. Jiang, "Adaptive liquid microlenses activated by stimuli-responsive hydrogels", *Nature*, vol. 442, no. 7102, pp. 551–554, 2006.

[145] H. Jia, E. Mailand, J. Zhou, Z. Huang, G. Dietler, J. M. Kolinski, X. Wang, and M. S. Sakar, "Universal Soft Robotic Microgripper", *Small*, vol. 15, no. 4, pp. 1–8, 2019.

[146] B. H. Cumpston, S. P. Ananthavel, S. Barlow, D. L. Dyer, J. E. Ehrlich, L. L. Erskine, A. A. Heikal, S. M. Kuebler, I. Y. Lee, D. McCord-Maughon, J. Qin, H. Röckel, M. Rumi, X. L. Wu, S. R. Marder, and J. W. Perry, "Two-photon polymerization initiators for three-dimensional optical data storage and microfabrication", *Nature*, vol. 398, no. 6722, pp. 51–54, 1999.

[147] T. Bückmann, N. Stenger, M. Kadic, J. Kaschke, A. Frölich, T. Kennerknecht, C. Eberl, M. Thiel, and M. Wegener, "Tailored 3D mechanical metamaterials made by dip-in direct-laser-writing optical lithography", *Advanced Materials*, vol. 24, no. 20, pp. 2710–2714, 2012.

[148] S. Y. Chin, Y. C. Poh, A. C. Kohler, J. T. Compton, L. L. Hsu, K. M. Lau, S. Kim, B. W. Lee, F. Y. Lee, and S. K. Sia, "Additive manufacturing of hydrogel-based materials for next-generation implantable medical devices", *Science Robotics*, vol. 2, no. 2, 2017.

[149] S. Maruo and H. Inoue, "Optically driven micropump produced by three-dimensional two-photon microfabrication", *Applied Physics Letters*, vol. 89, no. 14, pp. 5–8, 2006.

[150] S. Bianchi, G. Vizsnyiczai, S. Ferretti, C. Maggi, and R. Di Leonardo, "An optical reaction micro-turbine", *Nature Communications*, vol. 9, no. 1, pp. 1–6, 2018.

[151] M. J. Villangca, D. Palima, A. R. Bañas, and J. Glückstad, "Light-driven micro-tool equipped with a syringe function", *Light: Science and Applications*, vol. 5, no. 9, pp. 16 148–7, 2016.

[152] J. Kolb and W. L. Nyborg, "Small-Scale Acoustic Streaming in Liquids", *Journal of the Acoustical Society of America*, vol. 28, no. 6, pp. 1237–1242, 1956.

[153] N. Riley, "Teady treaming", *Annual Review of Fluid Mechanics*, vol. 33, pp. 43–65, 2001.

[154] P. Marmottant and S. Hilgenfeldt, "A bubble-driven microfluidic transport element for bioengineering", *Proceedings of the National Academy of Sciences of the United States of America*, vol. 101, no. 26, pp. 9523–9527, 2004.

[155] N. Nama, P. H. Huang, T. J. Huang, and F. Costanzo, "Investigation of acoustic streaming patterns around oscillating sharp edges", *Lab on a Chip*, vol. 14, no. 15, pp. 2824–2836, 2014.

[156] M. Kaynak, A. Ozcelik, N. Nama, A. Nourhani, P. E. Lammert, V. H. Crespi, and T. J. Huang, "Acoustofluidic actuation of in situ fabricated microrotors", *Lab on a Chip*, vol. 16, no. 18, pp. 3532–3537, 2016.

[157] M. Ovchinnikov, J. Zhou, and S. Yalamanchili, "Acoustic streaming of a sharp edge", *The Journal of the Acoustical Society of America*, vol. 136, no. 1, pp. 22–29, 2014.

[158] H. Bruus, "Acoustofluidics 7: The acoustic radiation force on small particles", *Lab on a Chip*, vol. 12, no. 6, pp. 1014–1021, 2012.

[159] A. Garcia-Sabaté, A. Castro, M. Hoyos, and R. González-Cinca, "Experimental study on inter-particle acoustic forces", *The Journal of the Acoustical Society of America*, vol. 135, no. 3, pp. 1056–1063, 2014.

[160] G. Q. Zheng, K. Katayama, M. Nishiyama, S. Kawasaki, N. Nishihagi, S. Kimura, M. Hagiwara, and K. Kindo, "Spin-echo NMR in pulsed high magnetic fields up to 48 T", *Journal of the Physical Society of Japan*, vol. 78, no. 9, 2009.

[161] G. T. Silva and H. Bruus, "Acoustic interaction forces between small particles in an ideal fluid", *Physical Review E - Statistical, Nonlinear, and Soft Matter Physics*, vol. 90, no. 6, pp. 1–11, 2014.

[162] O. R. Bilal, A. Foehr, and C. Daraio, "Bistable metamaterial for switching and cascading elastic vibrations", *Proceedings of the National Academy of Sciences of the United States of America*, vol. 114, no. 18, pp. 4603–4606, 2017.

[163] L. Jin, R. Khajehtourian, J. Mueller, A. Rafsanjani, V. Tournat, K. Bertoldi, and D. M. Kochmann, "Guided transition waves in multistable mechanical metamaterials", *Proceedings of the National Academy of Sciences of the United States of America*, vol. 117, no. 5, pp. 2319–2325, 2020.

[164] M. Kaynak, F. Ayhan, and M. S. Sakar, "Compound micromachines powered by acoustic streaming", *Proceedings - IEEE International Conference on Robotics and Automation*, vol. 2019-May, pp. 225–230, 2019.

[165] G. M. Whitesides, "The origins and the future of microfluidics", *Nature*, vol. 442, no. 7101, pp. 368–373, 2006.

[166] P. Yager, T. Edwards, E. Fu, K. Helton, K. Nelson, M. R. Tam, and B. H. Weigl, "Microfluidic diagnostic technologies for global public health", *Nature*, vol. 442, no. 7101, pp. 412–418, 2006.

[167] S. K. Vashist, P. B. Luppa, L. Y. Yeo, A. Ozcan, and J. H. T. Luong, "Emerging Technologies for Testing", vol. 33, no. 11, pp. 692–705, 2015.

[168] M. A. Unger, H. P. Chou, T. Thorsen, A. Scherer, and S. R. Quake, "Monolithic microfabricated valves and pumps by multilayer soft lithography", *Science*, vol. 288, no. 5463, pp. 113–116, 2000.

[169] M. Boukallel, M. Gauthier, M. Dauge, E. Piat, and J. Abadie, "Smart microrobots for mechanical cell characterization and cell convoying", *IEEE Transactions on Biomedical Engineering*, vol. 54, no. 8, pp. 1536–1540, 2007.

[170] L. Zhang, K. E. Peyer, and B. J. Nelson, "Artificial bacterial flagella for micromanipulation", *Lab on a Chip*, vol. 10, no. 17, pp. 2203–2215, 2010.

[171] W. Hu, K. S. Ishii, and A. T. Ohta, "Micro-assembly using optically controlled bubble microrobots", *Applied Physics Letters*, vol. 99, no. 9, pp. 1–4, 2011.

[172] T. Kawahara, M. Sugita, M. Hagiwara, F. Arai, H. Kawano, I. Shihira-Ishikawa, and A. Miyawaki, "On-chip microrobot for investigating the response of aquatic microorganisms to mechanical stimulation", *Lab on a Chip*, vol. 13, no. 6, pp. 1070–1078, 2013.

[173] E. B. Steager, M. Selman Sakar, C. Magee, M. Kennedy, A. Cowley, and V. Kumar, "Automated biomanipulation of single cells using magnetic microrobots", *International Journal of Robotics Research*, vol. 32, no. 3, pp. 346–359, 2013.

[174] H. W. Tung, D. F. Sargent, and B. J. Nelson, "Protein crystal harvesting using the RodBot: A wireless mobile microrobot", *Journal of Applied Crystallography*, vol. 47, no. 2, pp. 692–700, 2014.

[175] Z. Ye and M. Sitti, "Dynamic trapping and two-dimensional transport of swimming microorganisms using a rotating magnetic microrobot", *Lab on a Chip*, vol. 14, no. 13, pp. 2177–2182, 2014.

[176] J. Yu, B. Wang, X. Du, Q. Wang, and L. Zhang, "Ultra-extensible ribbon-like magnetic microswarm", *Nature Communications*, vol. 9, no. 1, pp. 1–9, 2018.

[177] A. Ozcelik, N. Nama, P. H. Huang, M. Kaynak, M. R. McReynolds, W. Hanna-Rose, and T. J. Huang, "Acoustofluidic Rotational Manipulation of Cells and Organisms Using Oscillating Solid Structures", *Small (Weinheim an der Bergstrasse, Germany)*, vol. 12, no. 37, pp. 5120–5125, 2016.

[178] P. Marmottant and S. Hilgenfeldt, "Controlled vesicle deformation and lysis by single oscillating bubbles", *Nature*, vol. 423, no. 6936, pp. 153–156, May 2003.

[179] P. H. Huang, N. Nama, Z. Mao, P. Li, J. Rufo, Y. Chen, Y. Xie, C. H. Wei, L. Wang, and T. J. Huang, "A reliable and programmable acoustofluidic pump powered by oscillating sharp-edge structures", *Lab on a Chip*, vol. 14, no. 22, pp. 4319–4323, 2014.

[180] S. E. Chung, W. Park, H. Park, K. Yu, N. Park, and S. Kwon, "Optofluidic maskless lithography system for real-time synthesis of photopolymerized microstructures in microfluidic channels", *Applied Physics Letters*, vol. 91, no. 4, pp. 26–29, 2007.

[181] A. C. Urness, E. D. Moore, K. K. Kamysiak, M. C. Cole, and R. R. McLeod, "Liquid deposition photolithography for submicrometer resolution three-dimensional index structuring with large throughput", *Light: Science & Applications*, vol. 2, no. 3, e56–e56, 2013.

Curriculum Vitae

Murat Kaynak

Lausanne, July 2021

Email: murat.kaynak@epfl.ch **webpage**: www.kaynakmurat.com **Phone**: +41 78 6477115

Address: EPFL STI IGM MICROBS MED 2715 (Bâtiment MED) Station 9, CH-1015 Lausanne, Switzerland

Research interest
Microrobotics, microfabrication, mechanical design, acoustics, lab-on-a-chip technologies

Education

EPFL, École polytechnique fédérale de Lausanne — Lausanne, Switzerland
Ph.D. in Mechanical Engineering — September 2021 (expected)
Advisor: Mahmut Selman Sakar

Pennsylvania State University — State College, PA, USA
M.Sc. in Engineering Science and Mechanics — August 2016
Advisor: Tony Jun Huang

University of Texas at Austin — Austin, TX, USA
Language School — June 2014

Istanbul University — Istanbul, Turkey
BA in Mechanical Engineering — July 2011

Publications

Kaynak, M., Amit, D., M. S. Sakar, "Mechanical programming of soft micromachines powered by ultrasound", 2021. (Under Review)

Hermans, L., **Kaynak, M.**, M. S. Sakar, Ramdya, P., "Long-term recording of the ventral nerve cord in behaving adult *Drosophila melanogaster*", 2021. (In preparation)

Amit, D., **Kaynak, M.**, M. S. Sakar, "Entrapped gas microbubbles with multiple openings: modal analysis, and streaming patterns", 2021. (Under review)

Lei, K., Kurum, A., **Kaynak, M.**, Gao, M., Xie, Y.-Q., Guo, Y., Hannebelle, M., Wu, Y., Zhou, G., Fantner, F., M. S. Sakar, Li, T., "Stiffening the plasma membrane of cancer cells enhances T-cell mechanical force and anti-tumour efficacy", *Nature Biomedical Engineering*, 2021. (Under review)

Amit, D., **Kaynak, M.**, M. S. Sakar, "On-board mechanical control systems for untethered microrobots", *Adv. Intell. Syst.*, 2021, 2000233

Kaynak, M., Dirix, P., M. S. Sakar, "Addressable Acoustic Actuation of 3D Printed Soft Robotic Microsystems", *Advanced Science* , 2020.

Guey, B., Wischnewski, M., Decout, A., Makasheva, K., **Kaynak, M.**, Sakar, M. S., Fierz, B., Ablasser, A., "BAF restricts cGAS on nuclear DNA to prevent innate immune activation", *Science*, 2020

Kaynak, M., Ayhan, F., M. S. Sakar, "Compound micromachines powered by acoustic streaming", *ICRA* , 2019.

Özkale, B., Parreira, R., Bekdemir, A., Pancaldi, L., Özelçi, E., Amadio, C., **Kaynak, M.**, Stellacci, F., Mooney, D. J., Sakar, M. S., "Modular soft robotic microdevices for dexterous biomanipulation", *Lab on a chip*, 2019

Kaynak, M., Ozcelik, A., Nourhani, A., Lammert, P. E., Crespi, V. H., Huang, T. J., "Acoustic actuation of bioinspired microswimmers", *Lab on a chip*, 20117

Orbay, S., Ozcelik, A., Lata, J., **Kaynak, M.**, Wu, M., Huang, T. J., "Mixing high-viscosity fluids via acoustically driven bubbles", *Journal of Micromechanics and Microengineering*, 2016

Ozcelik, A., Nama, N., Huang, P. -H., **Kaynak, M.**, McReynolds, M. R., Hanna-Rose, W., Huang, T. J., "Acoustofluidic rotational manipulation of cells and organisms using oscillating solid structures", *Small*, 2016

Kaynak, M., Ozcelik, A., Nama, N., Nourhani, A., Lammert, P. E., Crespi, V. H., Huang, T. J., "Acoustofluidic actuation of in situ fabricated microrotors", *Lab on a chip*, 2016

Honors and Scholarship

Graduate Study Abroad, covering all expenses for language and master's education and 1st year of Ph.D. (Turkish Ministry of Education) 2013-2016

Study Abroad Scholarship (Ministry of Energy, Turkey) (not attended) 2011

Prime Minister's Scholarship for undergrads (Prime Ministry of Turkey) 2006-2010

Research experience Research Assistant at MicroBioRobotic Systems Laboratory, EPFL

Advisor: Professor Mahmut Selman Sakar October 2016 – Present

- Development of remotely powered, soft microrobotic systems. I developed a set of acoustically actuated hydrogel micro machines to be used *in vivo*.
- Development of an implant for long-term and real time imaging of VNC in *Drosophila*. I designed and fabricated a microimplant comprised soft, stiff, compliant and light transparent sub-parts using various clean room methods such as 2PP, photolithography and thin film deposition.
- Setting up an experimental platform for breaking nuclear integrity in cells by keeping them alive to study cell's autoimmune response to self-DNA. I designed and fabricated a cell confinement device actuated through negative pressure and did the microscopy experiments.
- Setting up an experimental platform for high throughput measurement of cell stiffness. I built a microfluidic device in which thousands of cell pass through in seconds. Utilizing the shear force near channel walls, cells with different stiffness result in varying deformation.

Research Assistant at Acoustofluidics Laboratory, Pennsylvania State University
Advisor: Professor Tony Jun Huang August 2014 – August 2016

- I developed microrotors and microswimmers powered by acoustic streaming. I showed that micromachines can be powered remotely only using mechanical design only, without any additional agent.

Teaching experience

Teaching assistant, The Department of Mechanical Engineering (EPFL)
ME-436 Micro/Nano Robotics Spring 2021
ME-436 Micro/Nano Robotics Spring 2020
ME-436 Micro/Nano Robotics Spring 2019
ME-475 Multi-body Simulation Spring 2018
ME-475 Multi-body Simulation Spring 2017
Mentoring Activities: 4 Master's students in semester projects

Industry experience

Turkey's Ministry of Energy
Division of External Affairs Ankara, Turkey
Engineer 2011 – 2013
Preparation of technical reports for the Minister. Organizing seminar and conferences regarding energy production.

The Scientific and Technological Research Council of Turkey
Defence Industries Research and Development Institute Ankara, Turkey

Internship Summer 2009
I was the part of a team which were developing air-to-air rocket. I designed multiple units of that rocket in collaboration with technicians and engineers.

Talks

Micromachines powered by acoustic streaming December 2020
EDMI Research Days

Acoustically actuated micromachines May 2016
Pennsylvania State University MRSEC Seminar Series

Technical Skills

Clean Room Technologies

- Microscale Additive manufacturing (2PP, projection lithography)
- Photolithography
- Dry and wet etching
- Thin film deposition (Evaporation, Sputtering)
- Mask design and fabrication
- Scanning electron microscopy
- Optical and mechanical profilometer devices
- PDMS applications

Experimental Skills

- Design and fabrication of microfluidic lab-on-a-chip devices.
- Understanding and application of Acoustofluidics to applications in biomedical and engineering fields.
- Applications of acoustics in microfluidics for biomedical and materials sciences.
- Microscopy: inverted, upright, fluorescence

Software Skills
SolidWorks, Fiji, KLayout, Fortran, Adobe Illustrator, Origin, GraphPad, MS tools

Cell Culture
Familiarity with cell culture room activities and fluorescence imaging, on chip cell handling.